Fidy Andriamanankasina Ramamonjisoa

NON-CIRCULARITY OF BEAMS IN THE CMB POLARIZATION POWER SPECTRUM ESTIMATION

by

Fidy Andriamanankasina Ramamonjisoa

Submitted in fulfilment of the requirements for the degree of

Doctor of Philosophy

School of Mathematics, Statistics & Computer Science

University of KwaZulu-Natal

November 2013

As the candidate's supervisor I have approved this thesis for submission.

Signed: _____ Name: Subharthi Ray Date: _____

Abstract

Precise measurements of the Cosmic Microwave Background (CMB) anisotropies have been one of the foremost concerns in modern cosmology as it provides valuable information on the cosmology of the Universe. However, an accurate estimation of the CMB power spectrum faces many challenges as the CMB experiments sensitivity increases. Furthermore, for the polarization experiments, the precision of the measurements is complicated by the fact that the polarization signal is very faint compared to the measured total intensity and could be impossible to detect in the presence of high level of systematics. One of the most important source of errors in CMB polarization experiment is the beam non-circularity (asymmetry). In addition, the non-uniform and partial sky coverage resulting from the masking of the CMB foreground contaminants as well as point sources bias the estimation of the power spectrum. Consequently, a reasonable estimation of the power spectrum must account for, at least, the beam asymmetry and incomplete sky coverage. Accurate estimation of the angular power spectrum can be done using the standard optimal Maximum Likelihood (ML), although for high resolution CMB experiments with large data set this method is unfeasible due to the enormous computation time involved in the process.

The focus of this research is to estimate the CMB temperature anisotropy T and E-polarization cross-power spectrum and EE polarization power spectrum using a semi-analytical framework, and tackle the computational challenge of the TE power spectrum estimation with the pseudo-C_l estimator in the presence of the non-circular beam and cut-sky systematics. We examine, in the first step, the estimation of the CMB TE power spectrum by only considering the beam non-circularity with a complete sky, and give the error estimates of the power spectrum. Then, we will consider the more general case that includes the effect of the beam asymmetry and cut-sky as a result of the foreground removals across the Galactic plane. The numerical implementation of the bias matrix presents a huge computational challenge. Our ultimate goal is to speed-up the computation of the TE bias matrix that relates the true and observed power spectra in the case of a full sky coverage using a non-circular beam. We adopt a model of beams obtained from a perturbative expansion of the beam around a circular (axisymmetric) one in harmonic space and compute the bias matrix by using an efficient algorithm for rapid computation.

We show in this work that, in the case of non-circular beams and full sky survey, a fast computation of the TE bias matrix can be performed in few seconds using a single CPU processor by means of precomputations and insertion of symmetry relations in the initial analytical expression of the TE bias matrix. We present as well in the last part of this research the first analytical results of the EE bias matrix calculations in the case of a CMB experiment using

non-circular beams and incomplete sky coverage, and derive the corresponding results for the non-circular beams and full sky limit.

Preface

The work described in this thesis was carried out in the School of Mathematics, Statistics & Computer Science, University of Natal, Durban, from June 2010 to November 2013, under the supervision of Professor Subharthi Ray. Part of the computational work was carried out at the Inter-University Centre for Astronomy and Astrophysics, Pune, India from 6 July to 8 September 2012, under the supervision of Professor Sanjit Mitra and Professor Tarun Souradeep.

These studies represent original work by the author and have not otherwise been submitted in any form for any degree or diploma to any tertiary institution. Where use has been made of the work of others it is duly acknowledged in the text.

DECLARATION 1 - PLAGIARISM

I, Fidy Andriamanankasina Ramamonjisoa declare that

1. The research reported in this thesis, except where otherwise indicated, is my original research.

2. This thesis has not been submitted for any degree or examination at any other university.

3. This thesis does not contain other persons' data, pictures, graphs or other information, unless specifically acknowledged as being sourced from other persons.

4. This thesis does not contain other persons' writing, unless specifically acknowledged as being sourced from other researchers. Where other written sources have been quoted, then:

   (a) Their words have been re-written but the general information attributed to them has been referenced.

   (b) Where their exact words have been used, then their writing has been placed in italics and inside quotation marks, and referenced.

5. This thesis does not contain text, graphics or tables copied and pasted from the Internet, unless specifically acknowledged, and the source being detailed in the thesis and in the References sections.

Signed:

DECLARATION 2 - PUBLICATIONS

DETAILS OF CONTRIBUTION TO PUBLICATIONS that form part and/or include research presented in this thesis.

- Publication 1:
  "Cosmic Microwave Background TE Polarization Power Spectrum Estimation with Non-circular Beam and Incomplete Sky Coverage", Fidy A. Ramamonjisoa and Subharthi Ray; African Skies, Vol. 16, p. 144, 2011.
  Nature of candidate's contribution: principal author.

- Publication 2:
  "CMB Polarization TE Power Spectrum Estimation with Non-circular Beam", Fidy A. Ramamonjisoa, Subharthi Ray, Sanjit Mitra & Tarun Souradeep; MNRAS, 2013.
  Nature of candidate's contribution: principal author.

- Publication 3:
  "CMB Polarization TE Power Spectrum Estimation with Non-circular Beam and Incomplete Sky Coverage", Fidy A. Ramamonjisoa, Subharthi Ray, Sanjit Mitra.
  Nature of candidate's contribution: principal author.

- Publication 4:
  "CMB Polarization EE Power Spectrum Estimation with Non-circular Beam and Incomplete Sky Coverage", Fidy A. Ramamonjisoa, Subharthi Ray.
  Nature of candidate's contribution: principal author.

Signed:

Acknowledgements

I would like to acknowledge the academic, and financial assistance from the South African Square Kilometre Array (SKA) Project, Prof. Kesh Govinder and Prof. Kavilan Moodley whose support made this research possible. I would like to express my gratitude to Prof. Subharthi Ray who supervised this thesis. His suggestions, guidance and comments are gratefully appreciated. I would like also to extend my thanks to Prof. Kavilan Moodley for his precious advice and education on cosmology. I am very grateful to Dr. Moumita Aich for providing the code for computing the Clebsch-Gordan coefficients. Special thanks are due to Prof. Saumyadip Samui for making useful comments on the computational complexity of the code during the time of Group Meeting presentations. I wish to acknowledge all people of the Astrophysics and Cosmology Research Unit (ACRU) in the School of Mathematics, Statistics & Computer Science who facilitated my stay in the department. I wish to acknowledge Prof. Sunil Maharaj, Prof. Kavilan Moodley, all Faculty members and Post-Doctoral researchers who organised the Group Meeting, Seminar and Journal Club during my period of research at UKZN. I would like to express my special appreciation to Dr. Caroline Zunckel for her great effort of maintaining regular Journal Club meetings with Prof. Kavilan Moodley and Dr. Matt Hilton during my first year PhD. I acknowledge the Inter-University Centre for Astronomy and Astrophysics (IUCAA) for providing me with computer facilities as a guest. I would like to express my sincere gratitude to Prof. Sanjit Mitra and Prof. Tarun Souradeep for their guidance and collaboration during my period of visit at IUCAA where major part of the numerical implementation was completed. I would like to extend my thanks to all Postdoctoral researchers and PhD students of the ACRU for their collaboration and discussion about the project. Finally, I would like to acknowledge my family and friends for their support.

Contents

List of Figures

List of Tables

Chapter 1

Introduction

Over the past decade, the data from the *Wilkinson Microwave Anisotropy Probe* (*WMAP*) [1] [2] programme has kept scientists busy analysing them, tuning the standard model of cosmology as to the finer details and testing various models of cosmology - a true decade of precision cosmology. With the launch of the *Planck* [2] satellite by the European Space Agency in 2009, and with data currently starting to pour in, it becomes more challenging to analyse the data, as *Planck* probes for a much smaller angular resolution (larger multipoles). *Planck* is scanning the CMB sky to multipoles of ~ 3000, as compared to 1000 by the *WMAP*. To make full use of the potential of the data that we receive it is necessary to accurately determine the observed data, eliminating the systematic effects. One of the primary objectives to probe the CMB sky to such high multipoles is to determine the polarized CMB signals and, in particular, possibly detect the B-mode generated by tensor modes in the primordial perturbations of the density field which could indicate the signature of gravitational waves predicted by the inflationary cosmology [3, 4]. The CMB polarized signals (E-mode) produced by the quadrupolar anisotropy during the recombination epoch are a few order of magnitudes smaller than the total intensity of the anisotropy field [5], implying that even unsignificant systematic effects drastically bias the measurements of the CMB polarization.

The asymmetric beam response of instruments, a consequence of the off-axis placement of the detectors in telescopes, is one of the major systematic issues in CMB experiments as for small angular beam size, a highly asymmetric beam can strongly correlate with the sky signal distorting significantly the underlying true sky signal that we are unable to measure directly from observations. In CMB experiments the beam shape is measured using planets or bright sources observations combined with optical models [6–9]. The actual beam pattern of the experiment can be complex (e.g., *Archeops* [10]) and special tools and techniques have been depicted to model the beam shapes [9, 11–13], though in general an elliptical Gaussian fit provides a good description of the main

[1] http://map.gsfc.nasa.gov/
[2] http://sci.esa.int/planck

beam in many experiments (e.g., *MAXIMA-1* [3] [14], *Python V* [15], *WMAP* [6, 16, 17]) and in particular, the ongoing *Planck* survey [9, 18–21]). Nevertheless, the high precision measurements of the *Planck* mission require more elaborated beam models instead of the crude approximation of an elliptical Gaussian (see, e.g., [9]). The far sidelobes can be modelled separately in spherical harmonics [22], but we will neglect their contributions (see, e.g., [23]) in this work. We note that the sidelobe pickup systematic is ~ 0.5 % to 3.7% of the total sky signal sensitivity for *WMAP* [6]. The imperfection of the instruments optics triggers asymmetry in the beam response and even the main lobe in CMB experiments is not perfectly circular (axisymmetric). Therefore, when the beam is treated as circular (axisymmetric), the power spectrum is systematically biased, and consequently a beam smoothing correction is needed prior to the estimation.

The use of the optimal ML is desirable as it provides an accurate estimation of the CMB angular power spectrum C_l. Different ML estimators have been implemented in data analysis, mainly for small data size [24–27]. These estimators can handle various systematics including correlated noise, non-uniform/cut-sky and asymmetric beams. The method consists to find the covariance that maximizes the likelihood function, defined as the integral over all possible values of the true temperature anisotropy $\Delta T(\hat{q})$ ($\hat{q}$ denotes the pointing direction across the sky), which is statistically Gaussian distributed on the sky map. Nevertheless, the standard ML estimator requires intensive computation either in pixel space [27], or Fourier space [24, 25]. In fact, the evaluation of the inverse of the covariance matrix of the likelihood that scales as $\sim O(N_d^3)$ for a data size N_d [28, 29], is computationally expensive, even impossible for large datasets such as *WMAP* or *Planck*. Various techniques have been developed to speed up the ML estimation, such as exploiting the scanning strategy symmetries [30], using hierarchical decomposition of the CMB map with varying degrees of resolution [31], iterative multigrid method [32]. Specific methods such as estimate of the spectra on rings in the sky, can reduce the computational cost in special cases [33–35]. Other "exact" power spectrum estimation methods have also been proposed in the literature [36–38].

Alternatively, the suboptimal pseudo-C_l estimator [22] provides a very convenient way for a fast computation ($\sim O(N_d^{\frac{3}{2}})$) of the angular power spectrum C_l that we strive to measure. The pseudo-C_l method is exploiting the fast spherical harmonic transform ($\sim N_d^{\frac{3}{2}}$) to estimate the angular power spectrum $C_l = \sum_m a_{lm}^T a_{lm}^{E*}/(2l+1)$ [39, 40] from the data. This quadratic estimator is biased by the instrumental systematics that incorporate the beam asymmetry, partial sky/non-uniform sky coverage, noise, etc. Appropriate corrections of the systematic errors must be accounted for, in order to accomplish the debiasing of the power spectrum estimator. Quadratic estimators can be assorted in the way the spectra are corrected. We can illustrate the Spatially Inhomogenous Correlation Estimator (SpICE, [41]) which computes the two-point correlation function $C(\hat{q}.\hat{q}') = \langle \Delta T(q) \Delta T(q') \rangle$ in pixel space in order to account for the non-uniformity of the sky coverage. Chon et al. [42] have proposed the extension of SpiCE to polarization. Wandelt & Górski [22] and Hivon et al. [43] have

[3] http://www.cfpa.berkeley.edu/group/cmb/

presented the Monte Carlo apodized spherical transform estimator (MASTER), which allows a fast computation of the angular power spectrum from the data before correcting the galactic cut-sky in spherical harmonic space, by assuming circular beams. The method has been extended to the polarization [44–46]. Efstathiou [47, 48] has suggested a hybrid algorithm that computes the power spectrum using ML for low-resolution maps at low multipoles, and pseudo-C_l estimator for higher l where it tends to be nearly optimal in the presence of dominant instrumental noise. This hybrid approach has been applied to the *WMAP* 3-yr data analysis [49]. Hansen & Górski [44] have employed the Gabor transforms to recover the power spectrum of the temperature and polarization on cut-sky, and Wandelt et al. [50] have exploited a global, exact method for power spectra recovery from CMB observations using Gibbs sampling [51]. The beam non-circularity (asymmetry) effects can be simulated into the covariance functions in approaches related to ML estimation [26, 27], and can be included in Harmonic ring [33] and ring-torus estimators [35]. However, these estimators are computationally intensive and unfeasible for high-resolution maps and, the pseudo-C_l method, sufficiently fast, is preferred for extracting the power spectrum at large multipoles [47].

The thesis is structured as follows: in Chapter 2, we review the origin of the CMB temperature and polarization anisotropies and outline the importance of the polarization measurements in CMB experiments. We consider an example of non-circular beam model derived from an elliptical Gaussian fit to real experimental beam response and present an expression of the beam harmonic transform valid in the flat-sky approximation.

We develop in Chapter 3 the derivation of the bias matrix of the temperature T and E-mode polarization cross-correlation under the non-circular beam and full sky coverage assumptions and describe the details of the numerical implementation in order to optimize the computation time of the bias matrix. Then, we examine the effect of the beam non-circularity on the estimation of the TE angular power spectrum. We check the new expression of the TE bias matrix and show that it can reproduce the well-known bias matrix of the temperature and E-polarization correlation in the limiting case of a circular beam and complete sky.

In Chapter 4, we investigate the more complicate case where an asymmetric experimental beam is introduced in the presence of the cut-sky as a result of the mask applied to the foreground residuals. We derive the general expression of the TE bias matrix and demonstrate that the new analytical result of the bias matrix is consistent with the limiting case of the non-circular beam and full sky obtained in the previous chapter. We investigate as well the limiting case of an ideal symmetric beam with cut-sky and show that we can recover from this new result the TE bias matrix of a circular (symmetric) beam and complete sky coverage.

In Chapter 5, we treat the derivation of the EE bias matrix using non-circular beam and cut-sky by using the standard pseudo-C_l estimator. The derivation of the BB bias matrix will not be considered as the estimation of the very weak B-mode signal power spectrum requires the use of

the "pure" pseudo-C_l which does not mix the E and B-mode, and this topic is for now outside the scope of the thesis.

We draw the conclusion of this work in Chapter 6 and present a line of activity that we plan to undertake in the future.

We report in Appendix G some useful formulae which will be frequently referred to throughout the work.

Chapter 2

CMB anisotropies

The CMB radiation is a consequence of the Big Bang cosmology which describes the evolution of the Universe from its initial state of extreme pressure and density. When the Universe was young, before the formation of the stars and planets, it was filled with denser and high temperature plasma in thermal equilibrium with the electromagnetic radiation. The motion of the particles that interacted with the electromagnetic field is described by the Maxwell-Lorentz equations. At this early epoch, the Universe was radiation dominated and the gravitational interaction can be neglected in the physics description of the radiation-plasma fluid. As the Universe expanded, the temperature of both plasma and radiation dropped progressively and at a time when the Universe was cool enough, the electrons combined with protons to create atoms. The time at which the first neutral atoms was formed is referred to as the recombination epoch when atoms ceased to scatter with radiation and thus the Universe became transparent. In literature (e.g., [52]), the recombination is defined as the time when approximately 90% of the electrons initially present in the plasma have combined into neutral atoms. This process occurred at a redshift which is given by the following relation

$$a_{\rm rec}^{-1} = 1 + z_{\rm rec} \simeq 1310 \left(\frac{\Omega_{\rm b} h}{\sqrt{\Omega_0}}\right)^{0.078} \simeq 910 - 1340. \tag{2.1}$$

In this formula, $a_{\rm rec} = a(t = t_{rec})$ denotes the scale factor of the Universe at the time of recombination, z_{rec} the corresponding redshift, $\Omega_{\rm b} = 0.044 \pm 0.004$ the baryon density, $\Omega_0 = 1.02 \pm 0.02$ the total density and $h = 0.71^{+0.04}_{-0.03}$ the Hubble parameter. Shortly afterwards, the photons started to stream freely at a time known as the last scattering which is defined by the relation

$$a_{\rm LSS}^{-1} = 1 + z_{\rm LSS} = 1065 \pm 80, \tag{2.2}$$

where $a_{\rm LSS}$ and $z_{\rm LSS}$ denote the scale factor and redshift at the last scattering surface (LSS) from which the photons were emitted. At that time, the Universe was about $180000(\Omega_0 h^2)^{-\frac{1}{2}}$ years

old with a temperature of 0.26 eV. The time of photon decoupling is defined as the time when the photon scattering falls below the expansion rate of the Universe and the baryons fall out of equilibrium with photons. This occurred after the time of last scattering defined by

$$a_{\rm dec}^{-1} = 1 + z_{\rm dec} \simeq 890. \tag{2.3}$$

The corresponding age of the Universe at this time was about 380 000 years. As we can see the three events did not occur at the same time whereas in general, the time of recombination, the last scattering and decoupling are interchangeably used in the literature [53]. Thus, we can say that the first CMB photons we see today originated from the LSS at the time of decoupling when the constituents of the Universe underwent thermal equilibrium with a blackbody distribution.

2.1 CMB predictions and discoveries

The hot Big Bang theory predicts the existence of the CMB radiation that should have a blackbody spectrum with an intensity given by the formula

$$I_\nu = \frac{2h\nu^3}{c^2}\frac{1}{{\rm e}^{{\rm h}\nu/{\rm k_B T}} - 1}, \tag{2.4}$$

where ν denotes the frequency of the radiation, $k_{\rm B} = 1.381 \times 10^{-23}$ JK^{-1} $= 8.617342 \times 10^{-5}$ eVK^{-1} the Boltzmann constant and $h = 4.13566727 \times 10^{-15}$ eVsec [54] the Planck's constant. Gamow and his collaborators [55–58] were the first who recognized in 1948 that the Universe should be filled with that uniform blackbody radiation. In 1950, Ralph Alpher and Robert Herman [59] calculated the temperature of the radiation that started to free stream from the LSS at the time of decoupling. Based on nucleosynthesis considerations they found that the radiation should exist today and it would have cooled down to a low temperature $T_0 \sim 5$ K caused by the expansion of the Universe [53].

The CMB was serendipitously discovered in 1964 by Arno Penzias and Robert Wilson [60]. In fact, they were testing a communication antenna at Holmden, New Jersey. The Holmden telescope was intended for the *Echo* satellite experiment which was designed for communication purpose by means of satellites. In order to do the calibration of the instrument, they chose a specific frequency (wavelength $\lambda = 0.0735$ m) that is in a quiet window between the shorter wavelength of Galaxy emission and the longer wavelength of the atmosphere emission. During the studies of the telescope plus receiver noise, they unexpectedly found an excess of 3.5 K radiation noise that appeared to be isotropic. However, the excess noise could not have been interpreted as a signal from distant galaxies or Earth's atmosphere, thus Penzias and Wilson suspected technical or electronics problems in the telescope antenna. After a careful consideration of these possibilities, it was found that the "excess" turned out to be a background radiation that is uniformly filling the Universe. The isotropic radiation was observed in the microwave wavelength with a black body temperature of

roughly 3.5 K. They were not yet informed about the polarization of the radiation because the limited precision of their measurements.

The work of Gamow, Ralph Alpher and Robert Herman [58] was forgotten for decades until, in 1965 a group of physicists at Princeton University led by Robert Dicke [61] arrived at the same conclusion. They were preparing to measure the radiation, but before they could complete their experiment the CMB radiation (excess noise) was discovered by Penzias and Wilson. The results of Penzias and Wilson measurements were published in 1965 [60] along with a companion article [61] by Dicke and collaborators explaining its cosmological implications. In 1978, Penzias and Wilson were awarded the Nobel prize for the discovery.

The first precise measurements of the blackbody spectrum of the Planck distribution by NASA in 1989 was made with the Far Infrared Absolute Spectrophotometer (FIRAS) on board the Cosmic Background Explorer (*COBE*) [62]. A result of FIRAS analysis gives a black body temperature $T_0 = 2.725 \pm 0.001$ K [63].

2.2 Temperature anisotropies

Penzias and Wilson's conclusion about the isotropy of the background radiation was based on measurements only limited to 1.0 K accuracy. After the improvement of measurements carried out over years, it was found that the CMB radiation coming from different directions on the sky exhibits some irregularities: in one direction the radiation pattern was observed as a hot spot, and in the opposite direction as a cold spot. The corresponding pattern is known as the dipolar anisotropy. It is caused by the motion of the Earth/Solar system relative to the CMB rest frame. The dipole anisotropy is purely due to Doppler effect and contains no information about the intrinsic property of the CMB.

The typical variation in temperature ΔT across the sky is roughly a few tens of microKelvin. As the average temperature of the CMB is $T_0 = 2.725$ K, this corresponds to a tiny fluctuation in temperature of $\Delta T/T \sim 10^{-5}$. Since the CMB anisotropies encode the state of the Universe as it was at the time of decoupling, this means that the Universe was much homogeneous than it is now. In this section, we provide a statistical characterization of the temperature fluctuations. The CMB observable is the total intensity of the radiation field as a function of the frequency and the direction on the sky $\hat{q} = \hat{q}(\theta, \phi)$ (in spherical coordinates). The CMB radiation spectrum is a perfect blackbody with a mean temperature T_0, nearly constant across the sky. Generally, the observable is described by the temperature fluctuations

$$\frac{\Delta T(\hat{q})}{T_0} = \frac{T(\hat{q}) - T_0}{T_0} = \frac{T(\theta, \phi) - T_0}{T_0}. \tag{2.5}$$

The CMB temperature anisotropy field $\Delta T(\hat{q})$ over all directions on the sky $\hat{q}$ is assumed to be Gaussian distributed and statistically isotropic. In that case the temperature fluctuations on the sky can be expanded in spherical harmonics as

$$\frac{\Delta T(\hat{q})}{T_0} = \sum_{l=0}^{\infty} \sum_{m=-l}^{l} a_{lm} Y_{lm}(\hat{q}). \tag{2.6}$$

The $l = 0$ term is the monopole and is related to the photon energy density. We ignore this term because it is not measurable. The reason is that a particular observer is only limited to one Universe and one sky so that we are unable to determine the global mean over an ensemble of all possible Universes. For instance, if the monopole were larger than its average value in a neighborhood Universe, we would have no way of measuring the difference: we just cannot measure the photon energy density from a different Universe as our own (see, e.g., [1]).

The $l = 1$ term is the dipole which is the manifestation of the Doppler shift caused by the motion of our Solar System through space with respect to the CMB photons rest frame. The amplitude of the dipole is about 0.1 % of the CMB mean temperature. The temperature varies across the sky in such a way that the CMB photons are seen as colder in one direction and hotter in the opposite direction. To the first order $\Delta T = T_{\rm CMB}(v/c)\cos\theta$. The dipole temperature was measured by *COBE* with a precision better than 1% [64]. To first order, the orientation and amplitude of the dipole is given by [65]

$$\Delta T(\theta) = 3.358 \times 10^{-3} \cos\theta \text{ K}, \tag{2.7}$$

where θ is the angle of the dipole with respect to the direction of observation. From the observation and measurements of the diurnal average of the dipole temperature, we can estimate the velocity of the Sun with respect to the CMB frame which is roughly 370 kms^{-1}. Another dipolar contribution with an order lower than that of the dipole due to the Solar System motion through space, is produced by the motion of the Earth around the Sun.

The quadrupole $l = 2$ and the remaining modes $l > 2$ are due to intrinsic anisotropy produced by effects at the recombination epoch or between that time and the present time. For these effects the summation in Eq. (2.6) begins at $l = 2$. The spherical harmonics $Y_{lm}(\hat{q})$ are a complete orthonormal set of functions defined on the surface of a sphere. For a homogeneous and isotropic Universe, the coefficients a_{lm} generally complex satisfy the condition

$$\langle a^*_{l'm'} a_{lm} \rangle = C_l \delta_{ll'} \delta_{mm'}, \tag{2.8}$$

where δ_{ij} denotes the Kronecker symbol, and the brackets $\langle .. \rangle$ refer to the average taken over an ensemble of realizations. The quantity $C_l = \langle |a_{lm}|^2 \rangle$ is the angular power spectrum of the CMB

anisotropy. The multipole moments C_l main contributions come from fluctuations on angular scale $\theta \sim \pi/l$. The term $l(l+1)C_l$ is about squared temperature fluctuations on that scale. The temperature multipole components a_{lm} can be derived from the observed temperature $\Delta T(\hat{q})$ by using the orthonormal properties of the spherical harmonics,

$$a_{lm}^T = \frac{1}{T_0} \int d\Omega_{\hat{q}} \Delta T(\hat{q}) Y_{lm}^*(\hat{q}), \tag{2.9}$$

where $d\Omega_{\hat{q}} = \sin\theta d\theta d\phi$ is the solid angle over the sky. The mean-square $\langle |a_{lm}|^2 \rangle$ (power spectrum) is a measurement of the typical size of the CMB anisotropies. The condition of statistical isotropy implies that the power spectrum C_l values are independent of the choice of coordinates $\hat{q} = (\theta, \phi)$ (rotational invariance) in a given realization. Consequently, the angular power spectrum C_l cannot depend on the m index, but only depends on l. That is why C_l predictions are typically performed in harmonic space. As we do not consider the whole sky simultaneously on small angular scales, we can just focus on a small patch (area of a few deg^2 or smaller [66]) of the sky (flat-sky approximation) where its curvature becomes negligible, and the spherical harmonic analysis coincides with the Fourier analysis in two dimensions. In the flat-sky limit ($l \gg 1$), the multipole l becomes the Fourier wavenumber and the variance of the field is given by $\int d^2l \; C_l/(2\pi)^2$. The power spectrum is then usually plotted in the form [1]

$$\Delta_T^2 = \frac{l(l+1)}{2\pi} C_l T^2, \tag{2.10}$$

which corresponds to the power per logarithmic interval in wavenumber for $l \gg 1$.

The observed temperature anisotropies Δ_T (or ΔT) obtained by different CMB surveys are illustrated in Fig. 2.1, along with the predicted temperature for a given cosmological model. The *COBE* satellite first detection [62] of the temperature anisotropy was on the largest scales ($l \leq 15^\circ$). The term $l(l+1)C_l$ (i.e., temperature fluctuations) is nearly constant across the *COBE* range. The corresponding region is known as the Sachs-Wolfe plateau [67], which is produced by variations of gravitational field between regions. Afterwards, the observations have been pushed to much smaller scales (left to right in Fig. 2.1). The *MAP* [68] satellite launched in June 2001 has probed the multipoles up to ~ 1000, and the ongoing *Planck* survey ~ 3000. We report in Fig. 2.1 (bottom panel) the *Planck* satellite measurements statistical errors for the temperature and polarization anisotropies (see, next section). The CMB experiments shown in Fig. 2.1 are presented in Table 2.1.

The most updated observations of the CMB anisotropies have been recently undertaken with the release of the *WMAP* nine-year (*WMAP*9, [69]) and *Planck* [70] surveys data which are reported in Fig. 2.2. The *WMAP*9 *TT* power spectrum was computed by using the full set of V-band and W-band cross-power spectra. For $2 \leq l \leq 32$, the prediction of the *TT* power spectrum uses the Gibbs sample pixel likelihood estimator [69], which was already previously applied to the

analysis of the $WMAP$ five-year and seven-year data. For the multipole range $32 < l \leq 1200$, the expectation value of the power spectrum of the nine-year release was calculated using an unbiased and optimal quadratic estimator (Fig. 2.2 top panel). The high sensitivity of *Planck* allows to push the analysis to higher l up to ~ 2500. We can see in Fig. 2.2 (bottom panel) that the agreement between the model and the observations is good over the multipole range. A slight power deficit, discussed in [70], can be observed only at low l's.

The sky map of the CMB temperature fluctuations can be analysed in terms of an infinite series of correlation functions [71]. Inflation models predict the Gaussianity of the spectrum of the fluctuations, as current CMB data suggest. In such case of Gaussian fluctuations, the only non-vanishing correlations are of even order and the whole correlations can be expressed with the two-point correlation (autocorrelation) function $C(\theta)$ defined by

$$C(\theta) = \langle \frac{\Delta T(\hat{q}_1)}{T_0} \frac{\Delta T(\hat{q}_2)}{T_0} \rangle. \tag{2.11}$$

The temperature autocorrelation function $C(\theta)$ measures the product of the temperatures in two directions $\hat{q}_1$ and $\hat{q}_2$ separated by an angle θ and averaged $\langle .. \rangle$ over all possible directions. The angle θ satisfies the condition $\hat{q}_1.\hat{q}_2 = \cos\theta$.

On small angular scales θ, we can estimate the autocorrelation $C(\theta)$ from an individual sky using the ergodic hypothesis (see, e.g., [104, 105]) that states that the ensemble average (two-point correlation) should be the same as a spatial average within a single realization of the ensemble. The same holds for higher order correlations. This property only works on small angular scales where it is possible to average over several pairs of directions with the same angle θ.

On large scales, the estimation of the true autocorrelation $C(\theta)$ is difficult since there exist so few independent directions at large θ. As the Universe is homogeneous and isotropic, the average over all directions on the sky from a single observer (e.g., the Earth) should be close to the average obtained by other observers in different regions of the Universe (e.g., other Galaxies). Let us explain this by considering our position in the Universe: we can just see the CMB microwave photons emitted from the last scattering surface, which can be viewed as photons with different temperature and pattern by other observers situated in different Galaxies of the Universe [106]. What we can do is just taking the average over the realizations viewed from Earth (i.e., single sky). Those observers in other Galaxies measure an average, which corresponds to the cosmic mean that can be estimated by the correlation functions of inhomogeneities of the random field.

The root-mean-square difference between the local measurement (the Earth in our example) and the cosmic mean (other Galaxies observers measurement) is called *cosmic variance* (e.g., [71]). The difference is due to the poorer statistics of a single observer: we inhabit one region of the

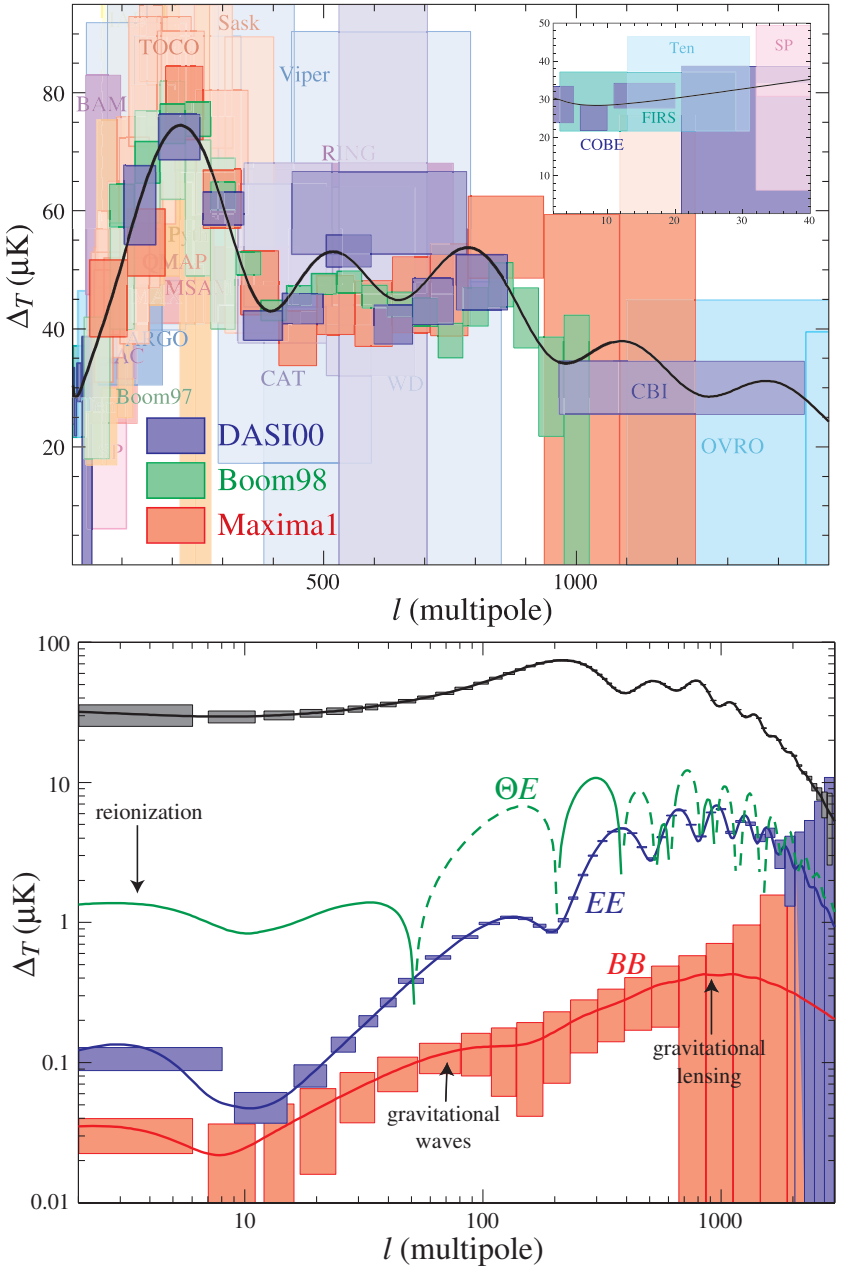

Figure 2.1: Temperature anisotropies spectra as a function of the multipole. The temperature anisotropy data measured from several CMB experiments are shown with boxes representing 1-σ errors and l-bandwidth (top panel). The temperature and polarization spectra TT, TE, EE, BB are also shown in log plot (bottom panel) where the boxes represent the statistical errors of *Planck* satellite. The dashed lines show the negative cross-correlation of T and E since the TE spectrum can be positive or negative (adopted from [1]).

Table 2.1: List of the CMB experiments illustrated in Fig. 2.1 and references (adapted from [1]).

Name	Authors	Journal Reference	
ARGO	Masi S et al. 1996	*ApJL* 463:L47–L50	[72]
ATCA	Subrahmanyan R et al. 2000	*MNRAS* 315:808–822	[73]
BAM	Tucker GS et al. 1997	*ApJL* 475:L73–L76	[74]
BIMA	Dawson KS et al. 2001	*ApJL* 553:L1–L4	[75]
BOOM97	Mauskopf PD et al. 2000	*ApJL* 536:L59–L62	[76]
BOOM98	Netterfield CB et al. 2002	*ApJ* 571:604–614	[77]
CAT99	Baker JC et al. 1999	*MNRAS* 308:1173–1178	[78]
CAT96	Scott PF et al. 1996	*ApJL* 461:L1–L4	[79]
CBI	Padin S et al. 2001	*ApJL* 549:L1–L5	[80]
COBE	Hinshaw G, et al. 1996	*ApJ* 464:L17-L20	[81]
DASI	Halverson NW et al. 2002	*ApJ* 568:38–45	[82]
FIRS	Ganga K, et al. 1994.	*ApJL* 432:L15–L18	[83]
IAC	Dicker SR et al. 1999	*ApJL* 309:750–760	[84]
IACB	Femenia B, et al. 1998	*ApJ* 498:117–136	[85]
QMAP	de Oliveira-Costa A et al. 1998	*ApJL* 509:L77–L80	[86]
MAT	Torbet E et al. 1999	*ApJL* 521:L79–L82	[87]
MAX	Tanaka ST et al. 1996	*ApJL* 468:L81–L84	[88]
MAXIMA1	Lee AT et al. 2001	*ApJ* 561:L1–L5	[89]
MSAM	Wilson GW et al. 2000	*ApJ* 532:57–64	[90]
OVRO	Readhead ACS et al. 1989	*ApJ* 346:566–587	[91]
PYTH	Platt SR et al. 1997	*ApJL* 475:L1–L4	[92]
PYTH5	Coble K et al. 1999	*ApJL* 519:L5–L8	[93]
RING	Leitch EM et al. 2000	*ApJ* 532:37–56	[94]
SASK	Netterfield CB et al. 1997	*ApJL* 474:47–66	[95]
SP94	Gunderson JO, et al. 1995	*ApJL* 443:L57–L60	[96]
SP91	Schuster J et al. 1993	*ApJL* 412:L47–L50	[97]
SUZIE	Church SE et al. 1997	*ApJ* 484:523–537	[98]
TEN	Gutiérrez CM, et al. 2000	*ApJL* 529:47–55	[99]
TOCO	Miller AD et al. 1999	*ApJL* 524:L1–L4	[100]
VIPER	Peterson JB et al. 2000	*ApJL* 532:L83–L86	[101]
VLA	Partridge RB et al. 1997	*ApJ* 483:38–50	[102]
WD	Tucker GS et al. 1993	*ApJL* 419:L45–L49	[103]
WMAP	`http://map.gsfc.nasa.gov`		
Planck	`http://sci.esa.int/planck`		

Universe, and there is no reason that we obtain exactly the same ensemble average as the average value of the Universe. In other words, we can only measure the a_{lm} for a single Universe (our own for example), but only the average over an infinity numbers of realizations (theoretically infinity Universes) coincides exactly with the predicted power spectrum. Averaging on m corresponds to averaging over directions. For each l, m varies from $-l$ to l so that there are $2l+1$ independent estimates (modes) of the power spectrum C_l in each multipole l (assuming full sky coverage). The cosmic variance depends on the number of representatives of the random inhomogeneities within a horizon. The variance is negligible at small angular scales but starts to dominate at large angular scales beyond 10°.

The cosmic variance sets a fundamental limitation to how accurately we can measure C_l. It leads to an unavoidable statistical error of

$$\Delta C_l = \sqrt{\frac{2}{2l+1}}\, C_l. \tag{2.12}$$

If we average over l in bins of width $\Delta l \sim l$, the corresponding precision of the power spectrum estimation scales as $1/l$. For example C_l can be measured at $l = 100$, $l = 1000$ respectively with 1% and 0.1% uncertainties. Experiments introduce additional uncertainties by measuring only a fraction of the sky, since regions of the Galaxy contaminated by strong foreground emissions must be removed. The resulting total difference from the cosmic mean is the *sample variance* [107]. If f_{sky} is the fraction of the sky covered, the sample variance is proportional to $f_{sky}^{-1/2}$ and equal to the cosmic variance when the area covered by the measurements approaches full sky. Noise of instrumental and astrophysical origin is a source of errors as well. If the noise is Gaussian, the power spectrum of the variance is replaced by the sum of the signal and noise power spectra. Finally, the instrument beam shape also affects the values of the cosmic variance (see, e.g., [108]). For a Gaussian random field, the autocorrelation (or covariance) function $C(\theta)$ can be expressed as a series of Legendre polynomials $P_l(\theta)$ of order l,

$$C(\theta) = \frac{1}{4\pi} \sum_{l=2}^{\infty} (2l+1) C_l P_l(\cos\theta), \tag{2.13}$$

where the summation starts at the quadrupole $l = 2$, since the monopole $l = 0$ is just the mean temperature on the observed patch of the sky, and $l = 1$ is the dipole.

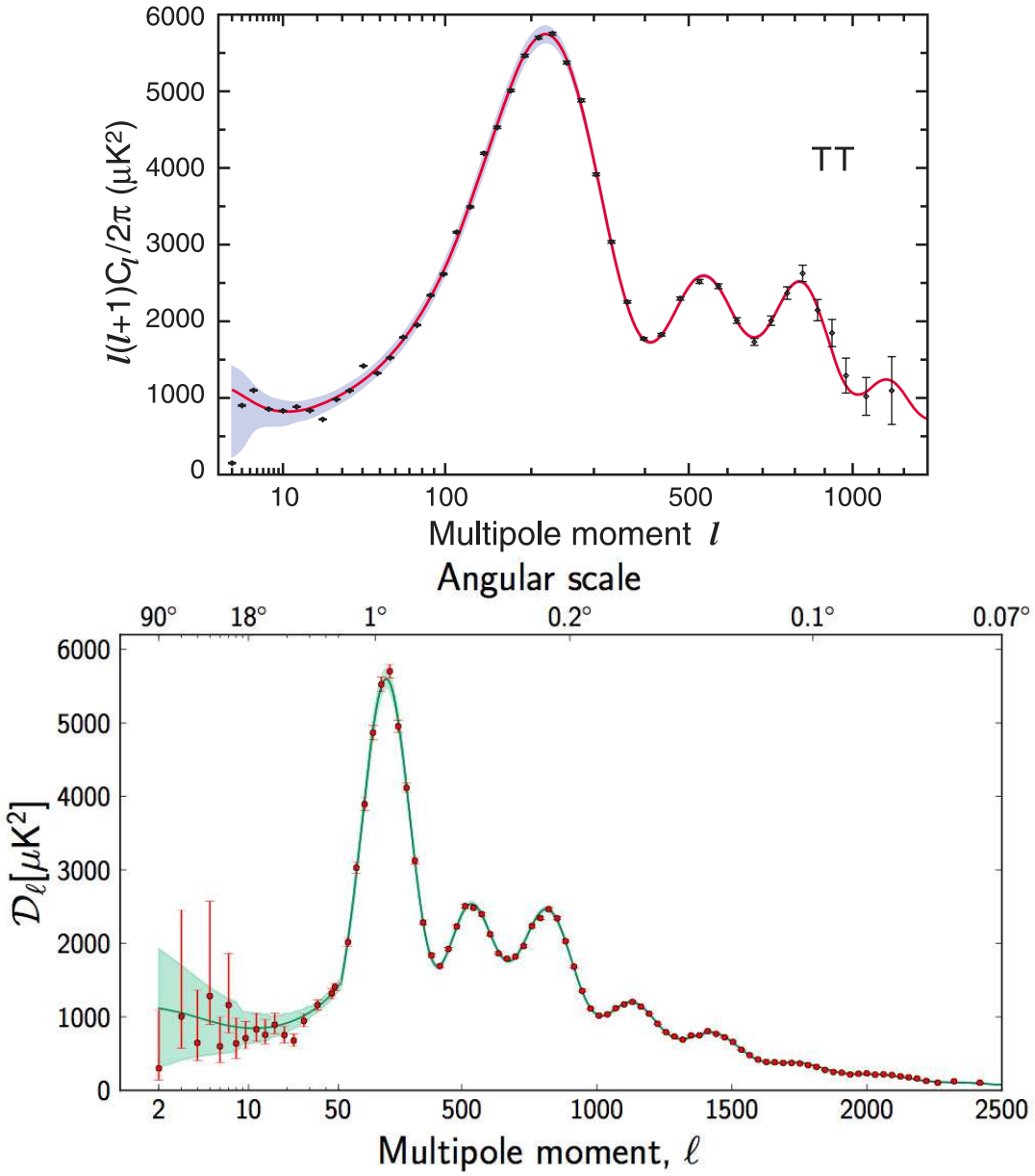

Figure 2.2: Power spectrum of the temperature fluctuations as a function of the multipole as measured by the *WMAP* nine-year survey (top panel) and *Planck* (bottom panel). The *WMAP* data are shown in black dots with the corresponding error bars. The *WMAP* best fit model is illustrated by the red curve and the smoothed binned cosmic variance is depicted with the grey shaded region. The 2013 *Planck* CMB temperature angular power spectrum is shown in bottom. The *Planck* data are shown in red dots with their error bars and the best fit model is represented by the green curve. The cosmic variance included in the error bars is indicated with the green shaded area (adopted from [69, 70]).

2.3 Polarization anisotropies

The temperature fluctuations autocorrelation provides the most valuable tool for distinguishing cosmological models. The power spectrum of the temperature allows the determination of cosmological parameters as well. However, we can exploit the polarization of the CMB radiation to gain additional subtle details about the history of the Universe at the recombination epoch. In particular, the detection of the CMB polarization (B-component of the polarized radiation field), a huge experimental challenge, will provide a clear evidence of the presence of the primordial gravitational waves generated by tensor modes, predicted by inflationary models [3, 4].

In addition, the polarization is much sensitive to the physical process of reionization which took place during the formation of the first stars. The Universe has been known to be ionized since a long time [109] at least up to the redshift $z \simeq 6$ [110]. The reionization is produced by high energy photons traversing ionised hydrogen clouds heated during the gravitational collapse of the first generation of stars [111]. Some estimations place the reionization between $z = 7$ and $z = 30$ [112]. Shortly after the recombination, the photons free-stream between their last scattering with electrons and again rescatter later with electrons in reionized hydrogen. Thus, the polarization fluctuations show up in large scale $l < 20$ and appear as bumps in the CMB power spectra. These bumps illustrated in Fig. 2.1 for the TE, EE, BB allow us to trace the reionization history of the Universe [113–115]. The first detection of the polarization from reionization was carried out with the $WMAP$ experiment [2, 116] with an optical depth of the reionization $\tau = 0.17 \pm 0.04$. Whereas this optical depth is larger than expected, it can be well described by an early reionization at the redshift range $11 < z < 30$ at 95% confidence level. Some work on early reionization is reviewed for instance in [117–121].

The first observations of the CMB polarization power spectra C_l^{TE} and C_l^{EE} were made by the Degree Angular Scale Interferometer DASI [122] and the $WMAP$ satellite [2].

2.3.1 Origin of the CMB polarization

The polarization in the CMB anisotropies originates from *Thomson scattering* by electrons. CMB photons behave as vector bosons particles. The electric and magnetic field of the CMB light can oscillate in the plane transverse to the direction of propagation. The light that propagates along the x-direction corresponds to electric and magnetic field oscillating in the y-z plane. If the intensity along the transverse directions y-z is equal, then the light is unpolarized; otherwise the light becomes polarized. The Thomson scattering by electrons can explain the polarization mechanism. It allows all radiation transverse to the direction of propagation to pass, but suppresses any radiation that is parallel to the outgoing direction.

In the following, we consider all possibilities that may lead to the production of a polarized

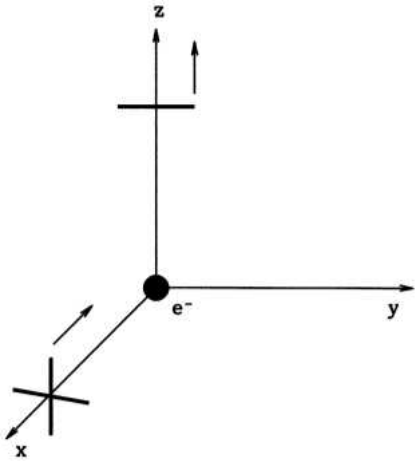

Figure 2.3: Scattering of an unpolarized radiation moving along the x-axis by an electron into the $\hat{z}$ direction. Only the intensity along the $\hat{y}$ direction that is not parallel to the outgoing $\hat{z}$ direction, gets transmitted after scattering. The net result is a polarized radiation along the $\hat{y}$ direction (adopted from [54]).

radiation. We closely follow the description of the mechanism by Dodelson [54]. Let us first consider the simple case of an incoming radiation from the $+\hat{x}$ direction which is sketched in Fig. 2.3. This incident unpolarized radiation that has equal intensity in the $\hat{y}$ and $\hat{z}$ directions scatters off an electron and generates an outgoing radiation scattered in all direction, in particular along the $+\hat{z}$ direction. As the intensity of the incoming radiation parallel to the outgoing $+\hat{z}$ direction is stopped, only the intensity which is perpendicular to both the incoming and outgoing radiation, along the y-axis is transmitted. This produces an outgoing polarized radiation in the $\hat{y}$ direction.

Now, let us consider the more general case of an incoming radiation from all directions. We show in Fig. 2.4 an example of an isotropic radiation coming from the $+\hat{x}$ and $+\hat{y}$ directions. The intensity of the outgoing radiation parallel to the x-axis comes from the incoming radiation along the $\hat{y}$ direction whereas the outgoing intensity along the $\hat{y}$ direction comes from the incident ray along the x-axis. As the incident isotropic radiation has equal intensity along both $\hat{x}$ and $\hat{y}$ directions, the outgoing radiation itself has equal intensity along the x and y-axis and consequently the outgoing radiation is unpolarized after the scattering by an electron.

Let us see what happens when the incoming radiation is anisotropic. This is the case of a dipole pattern which provides the simplest form of anisotropy. The incoming radiation from the $\hat{y}$ direction has an average intensity and produces, after scattering, the outgoing radiation with an average temperature along the $\hat{x}$ direction. The outgoing radiation parallel to the y-axis is neither cold nor hot since it is produced by the hotter radiation from the $+\hat{x}$ direction and the colder radiation from the -$\hat{x}$ direction leading to an outgoing radiation with an average intensity along the $\hat{y}$ direction. Therefore, the dipole generates no polarization since the intensities of the outgoing radiation along the $\hat{x}$ and $\hat{y}$ directions are equal. This is shown in Fig. 2.5.

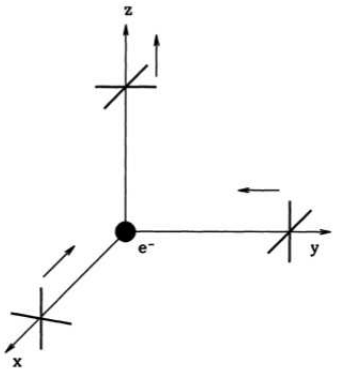

Figure 2.4: Incoming isotropic radiation scattered by an electron in the origin. Since the intensities of the incident rays from the $+\hat{x}$ and $+\hat{y}$ directions are equal, the amplitudes of the outgoing radiation along these directions are equal, resulting in unpolarized radiation (adopted from [54]).

In order to produce a polarized radiation, we need a local quadrupolar anisotropy which is illustrated in Fig. 2.6 (left panel). The incoming hot spots in the $\hat{x}$ direction scattered into the $\hat{z}$ direction leaving only the component of the radiation that is parallel to the $\hat{y}$ direction. During the scattering process, the electron is shaked in the $\hat{y}$ direction of its electric field or polarization $\hat{\epsilon}'$ producing an outgoing polarization parallel to the $\hat{y}$ direction [1]. Similarly, the outgoing polarization $\hat{\epsilon}$ must be perpendicular to the outgoing direction $\hat{z}$ and therefore, only the component of the cold spots parallel to the $\hat{x}$ direction remains after scattering. The Thomson differential scattering cross-section is given by $d\sigma/d\Omega = 3\sigma_T \mid \hat{\epsilon}'.\hat{\epsilon} \mid^2 /8\pi$ where Ω is the solid angle and σ_T the total Thomson cross-section.

Let us now focus on the orientation of the polarization. The orientation is described by the two components E and B and this decomposition can be visualized in the small scale limit, where the spherical harmonic and Fourier analysis are identical. Then the wavevector $\hat{k}$ which is shown in Fig. 2.6 (right panel) is oriented along a specific direction toward which the polarization direction is measured. The linear polarization (Thomson scattering of the CMB cannot generate a circular polarization) is invariant upon a 180° rotation since it is a "headless vector". The E and B components that describe the polarization are parallel or perpendicular to the wavevector (positive and negative E) and crossed at an angle 45° (positive and negative B) [1].

Naturally, there are three sources of quadrupolar anisotropies [65]:

- Vector perturbations: this effect is produced by vortex movements of the primordial fluid. However, the perturbations are negligible in most inflationary models.
- Tensor perturbations: this consists in the modification of the shape of the gravitational well produced by a gravitational wave traversing a density fluctuation. In this case, a well with symmetric shape can become elliptical leading to quadrupolar anisotropies.

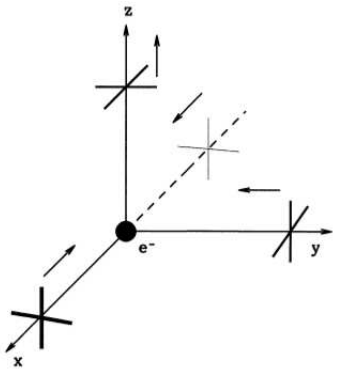

Figure 2.5: Scattering off an electron by an incoming dipole radiation. The heavy lines denote hot spots ($+\hat{x}$ direction) and the thin ones (-$\hat{x}$ direction) are the cold spots. The lines with medium thickness along the y-axis correspond to spots with an average temperature. The outgoing radiation along the $\hat{y}$ direction has an average intensity since it is produced by the hot and cold spots moving along the x-axis. The outgoing radiation along the $\hat{x}$ direction also has a mean temperature since it is the result of the scattering off the electron by the incident radiation with an average intensity (temperature) along the y-axis and therefore, the dipolar anisotropy cannot produce a polarized radiation (adopted from [54]).

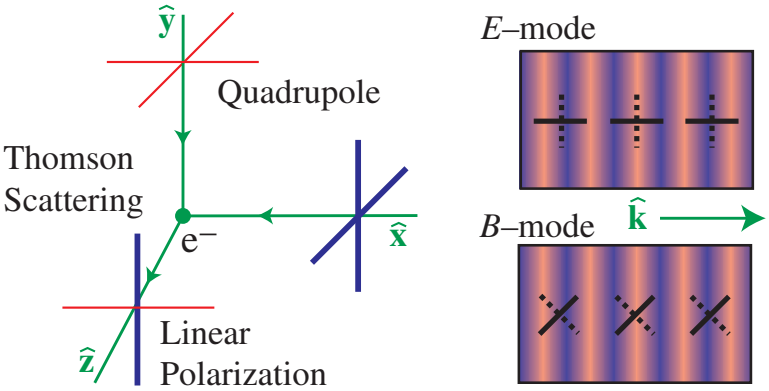

Figure 2.6: CMB polarization from Thomson scattering and classification. Left: Photons with a quadrupolar anisotropy ($\hat{x}$-$\hat{y}$ plane) scattered off a free electron producing a linearly polarized radiation. Note that the outgoing radiation has greater intensity (heavy lines denote hot spots) along the $\hat{y}$ direction than that in the $\hat{x}$-axis as a result of the much hotter incoming radiation (hot spot) from the $\hat{x}$-direction. Right: CMB polarization in the $\hat{x}$-$\hat{y}$ plane along the outgoing $\hat{z}$ axis. The polarization component that is parallel or perpendicular to the wavevector $\hat{k}$ is called the E-mode (E-type) and the one at an angle of 45 ° is called the B-mode (B-type) (adopted from [1]).

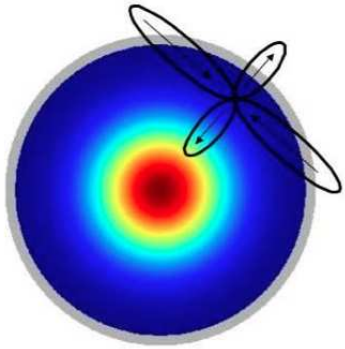

Figure 2.7: Quadrupolar anisotropies caused by density fluctuations in an over-dense region. Radially along the overdensity, the electrons move away from each other, while those belonging to the region of uniform density in the same contour tend to get closer (adopted from [65]).

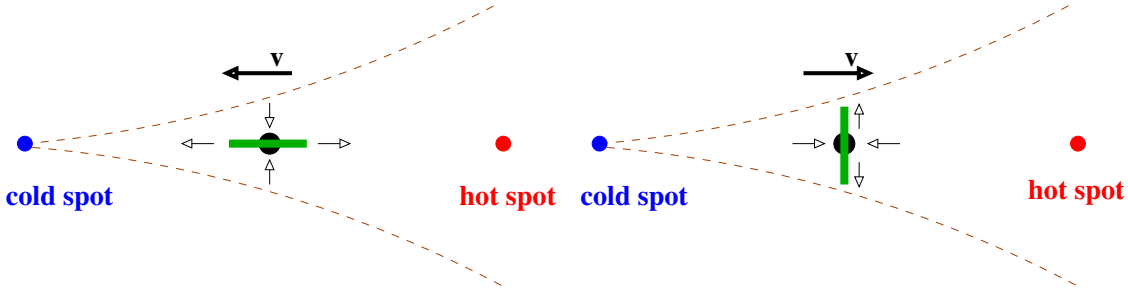

Figure 2.8: Polarization directions from velocity gradients when the fluid accelerates towards the cold spot (left panel) or decelerates towards a hot spot (right panel). The brown dashed curves represent the fluid stream lines. The small thin arrows show the direction of the fluid velocities in the photon baryon fluid rest frame near the scattering point. The large thick arrows depict the directions of the fluid motion near the scattering point relative to the hot and cold spots (adopted from [123]).

- Scalar perturbations: these scalar modes are linked to density perturbations causing quadrupolar anisotropies (see Fig. 2.7).

For the latter case of density fluctuations, the local quadrupolar anisotropies of the CMB photons on the last scattering surface at the end of recombination arise from velocity gradients (see, Fig. 2.8). When the fluid is accelerated from a hot spot (density dip, potential maximum) towards a cold spot (density peak, potential dip), the neighboring fluid velocities with respect to the photon baryon fluid rest frame, tend to diverge radially from and converge transversely to the scattering point. When the fluid is decelerated away from a cold spot, the neighboring particles velocities tend to converge radially to and diverge transversely from the scattering point. As a result of a Doppler shift, a quadrupolar flux anisotropy is induced around the last scattering point, causing a radial polarization in the first case (Fig. 2.8 left panel) and a transverse polarization in the second case (Fig. 2.8 right panel). Note that this geometrical scheme does not apply to tensor perturbations induced by primordial gravitational waves which do not need velocity gradients to produce CMB polarization [123].

2.3.2 Observable Stokes parameters

The Stokes parameters are the physical observable quantities that describe the polarization of the radiation. They are defined by the four parameters I, Q, U and V. An electromagnetic wave is characterized by the electric field vector $\hat{E}$ orthogonal to the direction of propagation $\hat{k}$ (wave vector). For a polarized wave propagating along the z-axis, the Stokes parameters take the form [123]

$$I = \langle |E_x^2| + |E_y^2| \rangle, \tag{2.14}$$

$$Q = \langle |E_x^2| - |E_y^2| \rangle, \tag{2.15}$$

$$U = \langle 2Re(E_x E_y^*) \rangle, \tag{2.16}$$

$$V = \langle 2Im(E_x E_y^*) \rangle, \tag{2.17}$$

where I denotes the total intensity of the radiation. The parameters Q and U describe the linear polarization of the radiation field whereas V characterizes its circular polarization. We neglect the last parameter V since it cannot be produced by Thomson scattering as it only modifies the amplitudes of the components while the phases remain unchanged. Thus, for CMB photons $V = 0$. The conservation of energy implies that $I^2 \geqslant Q^2+U^2+V^2$, which means that the polarization energy cannot exceed the total energy. I and V are invariant under rotation whereas Q and U depend on the reference frame. In a map representation using "rods", the polarization amplitude is given by $P = \sqrt{Q^2 + U^2}$ (rotation invariant), and the orientation makes an angle $\alpha = \frac{1}{2}\arctan(U/Q)$ with the vector $\hat{e}_1$ which is perpendicular to the direction on the sky $\hat{q}$ [53, 124]. As the quantity $Q^2 + U^2$ is invariant under rotation, it follows that the polarization $\mathbf{P}$ is a second rank tensor that reads [53]

$$\mathbf{P} = \frac{1}{2} \begin{pmatrix} Q & U - iV \\ U + iV & -Q \end{pmatrix}. \tag{2.18}$$

This means that unlike the electric field vector, the polarization is not a vector quantity with a given direction. While the temperature (total intensity I) is invariant under a rotation in the plane perpendicular to the direction of propagation $\hat{q}$ (i.e., parallel to the direction $\hat{q}$ on the sky), the Stokes Q and U transform under rotation. Let us choose two basis vectors $\hat{e}_1$ and $\hat{e}_2$ orthogonal to $\hat{k}$ (or $\hat{q}$). If $\hat{e}_1$ and $\hat{e}_2$ are rotated by an angle ψ about the direction $\hat{q}$, then Q and U rotate and transform to Q' and U' by an angle 2ψ, and we may write

$$Q' = Q\cos(2\psi) + U\sin(2\psi), \tag{2.19}$$

$$U' = -Q\sin(2\psi) + U\cos(2\psi), \tag{2.20}$$

or equivalently [123]

$$Q \pm iU \rightarrow Q' \pm iU' = e^{\mp 2i\psi}(Q \pm iU). \tag{2.21}$$

This is known as a spin-2 transformation and the quantities $Q \pm iU$ are said to be spin-2 [124].

2.4 Polarization multipole expansion

In this section, we follow a close presentation of the multipole analysis as [124]. While observing the celestial sphere, it is more convenient to treat the statistical properties of the CMB fluctuations on spherical harmonic basis, which is basically the Fourier basis as the CMB anisotropies random properties are rotationally invariant. Instead of the standard spherical harmonics which are spin-0 quantities, we need to use the spin-2 spherical harmonics to describe the polarization since the quantities $Q \pm iU$ are spin-2 variables. Thus, we can expand the Stokes parameters in the spin-2 spherical harmonic basis as [125]

$$(Q \pm iU)(\hat{q}) = \sum_{lm} a_{\pm 2,lm} \ {}_{\pm 2}Y_{lm}(\hat{q}), \tag{2.22}$$

$$= \sum_{l \geqslant 2} \sum_{m=-l}^{l} a_{\pm 2,lm} \ {}_{\pm 2}Y_{lm}(\hat{q}). \tag{2.23}$$

Q and U depend on the sky direction $\hat{q}$ with respect to the spherical coordinates basis $(\hat{e}_\theta, \ \hat{e}_\phi)$ [126, 127]. The multipole coefficients of the polarization expansion satisfy the following relation in order to ensure that the observables Stokes parameters Q and U are real: $a^*_{-2,lm} = a_{2,l-m}$. For the temperature, the reality condition implies $a^{T*}_{lm} = a^T_{l-m}$. From the spin-2 multipole coefficients $a_{\pm 2,lm}$, we can construct in real space, by using linear combinations of the coefficients of the expansion, two real scalar quantities defined by

$$E(\hat{q}) = \sum_{l,m} a^E_{lm} \ Y_{lm}(\hat{q}), \tag{2.24}$$

$$B(\hat{q}) = \sum_{l,m} a^B_{lm} \ Y_{lm}(\hat{q}), \tag{2.25}$$

where $E(\hat{q})$ is with positive parity and $B(\hat{q})$ with negative parity. The connection between Q/U and E/B in spherical harmonic space is

$$a^E_{lm} = -\frac{a_{2,lm} + a_{-2,lm}}{2}, \tag{2.26}$$

$$a^B_{lm} = i\frac{a_{2,lm} + a_{-2,lm}}{2}. \tag{2.27}$$

The scalar E and the pseudo-scalar B can completely describe the linear polarization of the radiation. The temperature is a real scalar rotationally invariant as $T'(\hat{q}' = \mathcal{R} \ \hat{q}) = T(\hat{q})$, where $\mathcal{R}$ denotes the rotation matrix. Unlike the spin-2 quantities $Q \pm iU$, $E(\hat{q})$ and $B(\hat{q})$ defined from

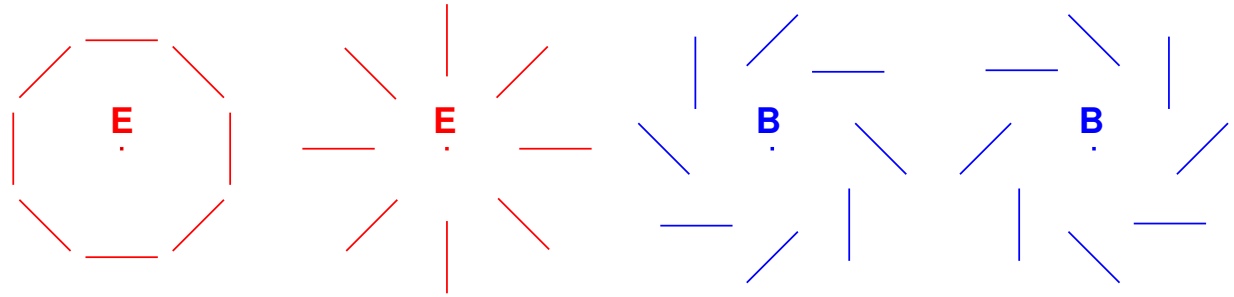

Figure 2.9: Parity of E-type and B-type polarization patterns. The E patterns are invariant under reflection across a line going through the centre whereas the B patterns are interchanged under transformation (adapted from [124]).

the Stokes parameters are invariant under rotations: they are independent of the reference frame. However, as we have previously seen they have opposite behaviour under parity transformations. The different parity properties of E and B are illustrated in Fig. 2.9. The polarization patterns show positive and negative E and B. We can see in Fig. 2.9 that the E polarization patterns remain unchanged if reflected across a line going through the centre. Contrarily, the B pattern changes to the opposite parity from positive to negative. The E patterns are "gradient-like", and the B patterns are "curl-like". Note that E and B are not local quantities, since the E or B type of the polarization is a property of the polarization pattern around a particular point, and not at that point. We can establish some analogy between vector field and polarization field geometrical properties. As the polarization field is a spin-2 object, this means that a rotation of the coordinate system by an angle 180° brings back the same components of the polarization radiation field whereas a rotation of 360° is needed for vector fields. A supplementary information about the similarities and differences between vectors and polarization fields can be found in Bunn et al. [128].

The random properties of the CMB Gaussian fluctuations are fully described by four power spectra if there is no parity violation: the autocorrelations TT, EE, BB and the cross-correlation TE. The cross-correlation between B and E, or B and T vanishes since B has the opposite parity to T or E [124]. Thus, the invariance of the stochastic properties under rotations and the parity conservation imply the following relations

$$\langle a^{T*}_{lm} a^{T}_{l'm'} \rangle = C_l^{TT} \delta_{ll'} \delta_{mm'}, \tag{2.28}$$

$$\langle a^{T*}_{lm} a^{E}_{l'm'} \rangle = C_l^{TE} \delta_{ll'} \delta_{mm'}, \tag{2.29}$$

$$\langle a^{E*}_{lm} a^{E}_{l'm'} \rangle = C_l^{EE} \delta_{ll'} \delta_{mm'}, \tag{2.30}$$

$$\langle a^{B*}_{lm} a^{B}_{l'm'} \rangle = C_l^{BB} \delta_{ll'} \delta_{mm'}, \tag{2.31}$$

where C_l's and $\delta_{ll'}$ denote the angular power spectra of the CMB anisotropies and the Kronecker symbol. Some examples of models with parity violation are discussed in [129].

The choice of the estimator for the characterization of the statistical properties of the CMB fluctuations depends on the goal of the CMB survey. Throughout this work, we will employ an estimator based on spherical harmonic space. For Gaussian fluctuations, we define the rotationally invariant power spectra

$$C_l^{TT} = \frac{1}{2l+1} \sum_{m=-l}^{l} \langle a_{lm}^{T*} a_{lm}^{T} \rangle, \tag{2.32}$$

$$C_l^{TE} = \frac{1}{2l+1} \sum_{m=-l}^{l} \langle a_{lm}^{T*} a_{lm}^{E} \rangle, \tag{2.33}$$

$$C_l^{EE} = \frac{1}{2l+1} \sum_{m=-l}^{l} \langle a_{lm}^{E*} a_{lm}^{E} \rangle, \tag{2.34}$$

$$C_l^{BB} = \frac{1}{2l+1} \sum_{m=-l}^{l} \langle a_{lm}^{B*} a_{lm}^{B} \rangle, \tag{2.35}$$

where the brackets $\langle .. \rangle$ denote the ensemble averages of all statistical realizations. The justification of the choice will be reported in Chapter 3.

As a prominent part of this thesis mostly deals with the estimation of the TE cross-power spectrum, as an illustration we present in Fig. 2.10 current observations and theoretical best-fit of the temperature T and E-mode polarization cross-spectrum. In the $WMAP9$ data release, the TE angular cross-power spectrum was calculated using the MASTER [43] likelihood code, while the lowest multipole bin $2 \leq l \leq 7$ power was estimated using the more accurate pixel likelihood code [69] (Fig. 2.10 top panel). The *Planck* preliminary observations (Fig. 2.10 bottom panel) are in excellent agreement with the best-fit ΛCDM cosmological model. The TE cross-power spectrum data are binned with a band width $\Delta l = 40$. A uniform weighted average of all detector sets combinations at 70×100, 100×143, 100×217, and 143×217 GHz allows the computation of the observed spectrum using the method described in [70].

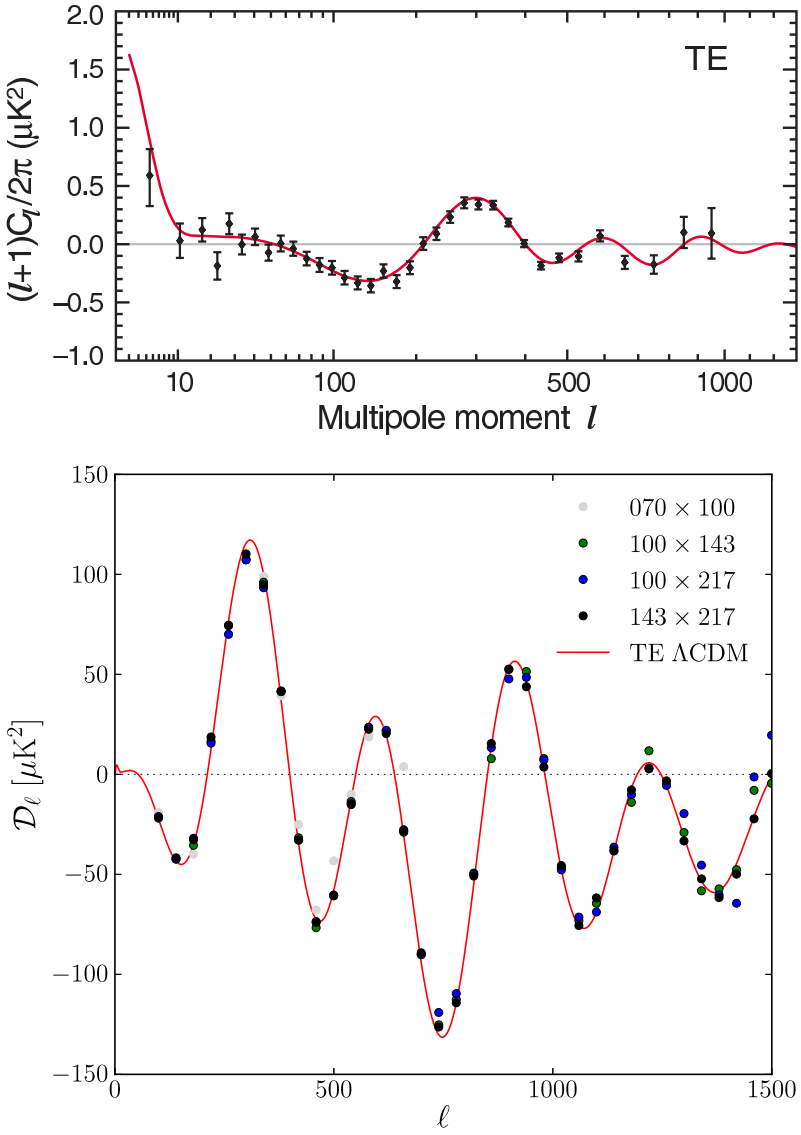

Figure 2.10: The TE spectrum can be positive or negative, and is in opposite phase to the TT spectrum. The *WMAP* data with the corresponding error bars are shown in black, and the red curve is the best fit to the full *WMAP* data that include the TT data as well (top panel). Note that the vertical axis is (l+1)$C_l/2\pi$ so that the scale differs from that of the TT spectrum by a multiplication factor l. For comparison, the *Planck* computed TE power spectrum is illustrated in the bottom panel where the red curve represents the best fit only to the *Planck* temperature data as predicted from the six-parameter ΛCDM model (adopted from [69, 70]).

2.5 Systematics

A systematic error is inevitable in CMB data analysis since it is always present even an average over many data samples is taken. If we consider for example a single measurement on the sky, it would be difficult to disentangle the sky signal from the systematic effects, and the same holds between the real signal and random noise. Among the systematics, our particular interest is on the beam asymmetry and foregrounds which are the only relevant systematics studied in this thesis. We follow the presentation of the systematics described in [65].

2.5.1 Beam asymmetry

The beam is an optical transfer of the instrument. The telescope beam defined by the point-spread-function (PSF) is the instrument response to a signal on the sky. The detectors beams are estimated from the observations of planets or brighter stellar sources from which a model of beam is constructed. The *WMAP* mission beam maps in the Q1, V1 and W1 bands have been fitted with an elliptical Gaussian profile with the radio-astronomy software Astronomical Image Processing System (AIPS) and ellipse fitting routine software Image Reduction and Analysis Facility (IRAF) [130]. The actual beam shape is in general complicated, and for this reason different modern techniques have been developed to model and reconstruct the beam of the ongoing high sensitivity and resolution *Planck* experiment (e.g., [9]).

For CMB experiments using circularly symmetric beams, a one dimension profile can be used to simulate the beam. For asymmetric beams, brighter sources such as Jupiter for $WMAP$ [6] or *Archeops* [10] are used for the construction of the beam shape. The beam systematics are usually simulated and corrected on the power spectrum. The simulations include the convolution of the sky with the beam, which depends on the shape and orientation of the beam on the sky. For non-circular (asymmetric) beams the convolution in a given direction is time dependent which requires intensive computation. Different convolution methods have been developed. They are exploiting a convolution algorithm [35] in harmonic space or decomposition of a pixel based beam model into harmonic space. Several methods of beam symmetrization have been investigated [6, 14], and a model using a decomposition of the beam pattern into Gaussian beams has been proposed [131]. A semi-analytical model of beam has been developed to approximate the ellipticity of the beam [15, 66]. Throughout this thesis, we will adopt the beam model of Fosalba et al. [66] based on the perturbative expansion of the beam around a circular (axisymmetric) Gaussian one. However, it is important to note that this approximation is not sufficient to achieve percent level accuracy with *Planck* (see, e.g., [9]). We explain this choice by the fact that the main purpose of the work was to investigate how to reduce the computational cost of the beam convolution with the sky maps. Thereafter, we can incorporate in our numerical implementation more realistic beams whose convolution can be computed by following the same algorithm exposed in the thesis.

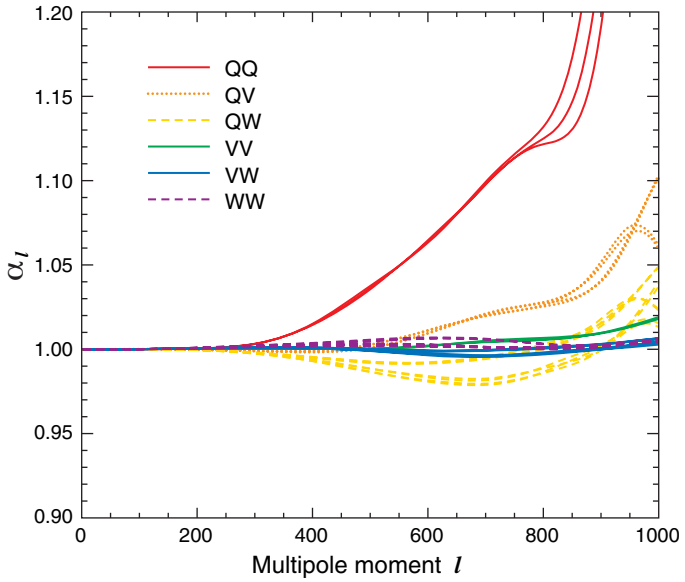

Figure 2.11: Bias estimate in the angular power spectrum due to the beam asymmetry for each *WMAP* channel. The ratio α_l is an estimate of the error introduced in the power spectrum when the actual asymmetric beam is treated as circular (symmetric). The data from Q band is not included in the final power spectrum (adopted from [49]).

The polarized beam response is measured in the co- and cross-polar basis defined on the sphere. For a given polarized beam, the direction of polarization is defined by the image of sensitivity direction of the optics, and the cross-polarization direction is orthogonal to the co-polarization. The asymmetry of the main beam can contaminate the polarization and this effect depends on the scanning strategy. The main intensity beam and cross-polarization are estimated using simulations.

The far sidelobes are measured using bright sources such as the Moon or Sun. The sidelobe pickup causes spurious signal into the time ordered data inside each detector, but their effects are quite small relative to the sky signal.

The effects of beam asymmetry on the angular power spectrum C_l is illustrated in Fig. 2.11. The ratio α_l represents the multiplicative error in the angular power spectrum when the actual beam is assumed as a circular Gaussian in the model of beam. We clearly see that the systematic error introduced by the beam asymmetry is significant at high multipoles. Therefore, appropriate corrections must be accounted for the debiasing of the power spectra of CMB high resolution experiment. This step is crucial as the cosmological parameters derived from the power spectrum are very sensitive to the slight deviation of the power spectrum from its true value.

2.5.2 Foregrounds

The CMB anisotropy signals are exposed to various astrophysical foreground emissions which contaminate the measured CMB signals. For instance, in all *WMAP* frequencies the microwave sky is polarized, and in K band the flux is much larger than the level of CMB polarization. Around the frequency 60 GHz and multipole $l \sim 5$, the temperature of the foreground emission exceeds about a factor of two the CMB polarization signal [132]. Thus, a subtraction of the foreground emission based on the *WMAP* (and later on *Planck*) polarization measurements is essential, before the estimation of the CMB polarization signal. The main contaminants of the CMB signal can be classified as follows.

- Synchrotron emission
  This radiation is produced by relativistic electrons accelerated by magnetic field. The synchrotron spectrum depends on the intensity and energy of the electrons. The Galactic magnetic field is strong enough (few nG) to contaminate CMB measurements. The energy spectrum of the electrons can be modelled as a power law $\nu^{-\beta}$ with $\beta \simeq 3$ [133]. The synchrotron radiation, which can exhibit strong polarization in the direction perpendicular to the Galactic magnetic field [134], is the dominant foreground contaminant at lower CMB frequency observations.

- Free-free emission (Bremsstrahlung)
  This radiation is produced by decelerating electrons traversing hot gas ions. The spectrum of the emission is a power law with a spectral index $\beta \simeq 2.1$ [133]. Free-free emission is dominant at CMB lower frequencies. Broadly speaking, free-free emission is unpolarized but a polarized emission may exist at the edges of HII clouds [135].

- Dust emission
  This radiation is emitted by cold dust via thermal radiation or by excitation of electrical dipolar moment. The radiation is a grey body with temperature $T \sim 17$ K and the emission peaks in the far-infrared. The dust emissivity is modelled as ν^2 [136]. Vibrational dust emission is between 10 and 100 GHz with a peak around 20 GHz [137]. The level of polarization of spinning dust grains is roughly 1-2% [138].

- Point sources
  They can emit radio-millimetric waves and contaminate the CMB signals. The radio sources polarized emission is negligible in the *WMAP* band. The effects of undetected background sources on the CMB spectrum are evaluated with Monte-Carlos simulations.

We show in Fig. 2.12 an example of CMB and foreground models based on MCMC technique. These foreground models are discussed in Bennett et al. [69] and each of the models presents strengths and weaknesses. For instance, using the MCMCg model [69], it appears that the CMB foreground covariance dominates in the Galactic plane and as a result the CMB and foregrounds

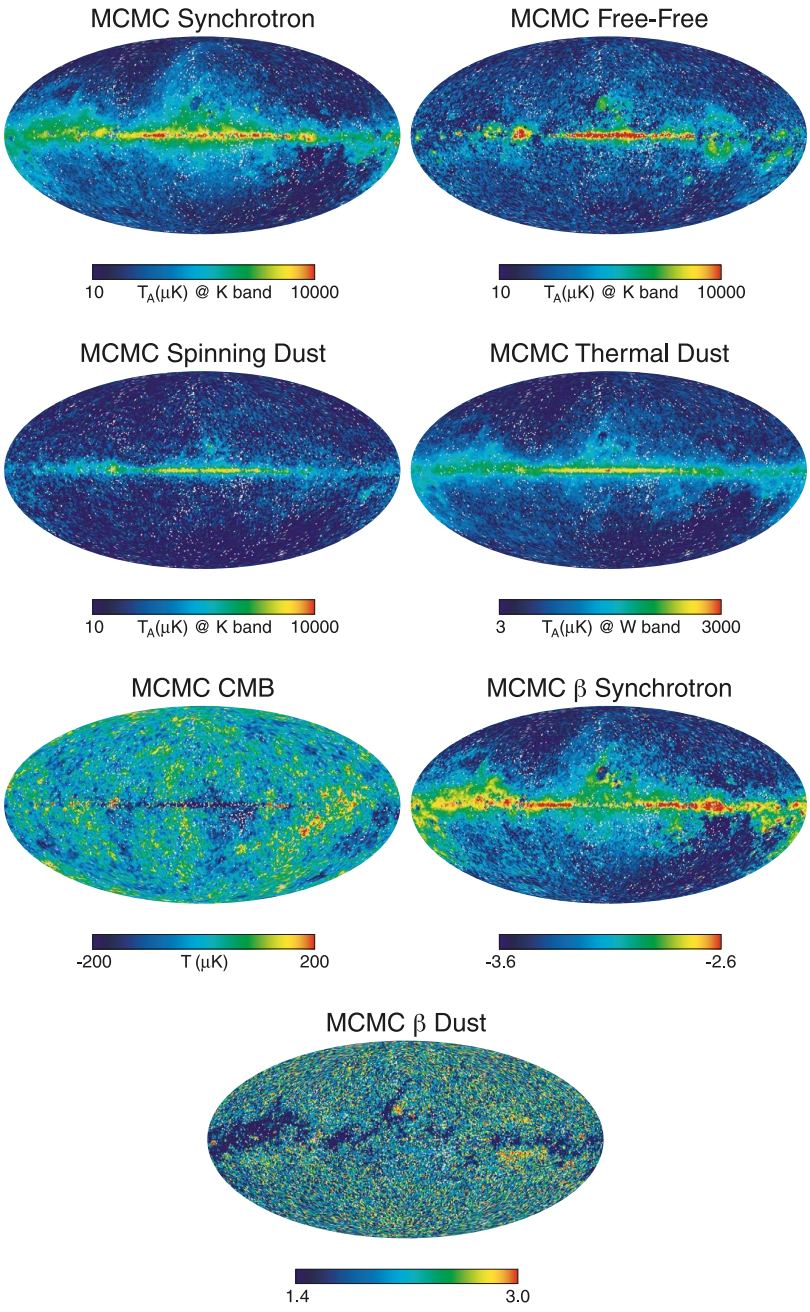

Figure 2.12: CMB and foreground models constructed from the MCMCg model fit [69]. The top four maps are the foreground models on logarithmic scales. The other three maps are the CMB and foreground parameter maps on linear scales. The β synchrotron map is calculated at 40 GHz (adopted from [69]).

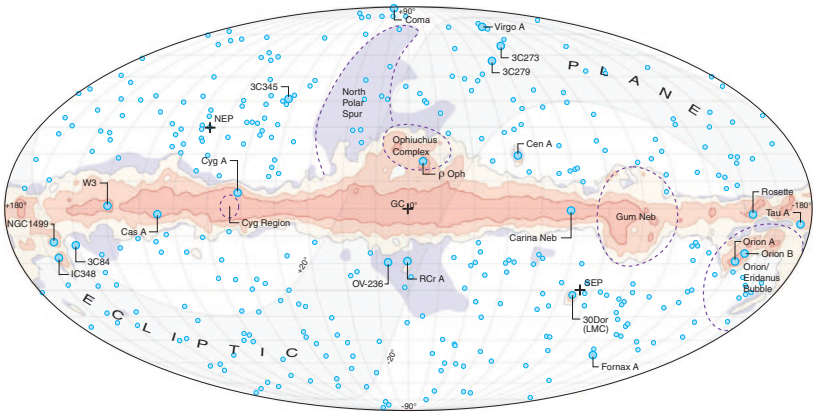

Figure 2.13: An overview of the microwave sky. The yellow, salmon, and red shaded regions illustrate various temperature masks Kp0, Kp2 and Kp8 designed to remove the effects of strong diffuse emissions along the Galactic equatorial plane. The violet shaded regions correspond to the P06 polarization mask described in Page et al. [132] . The small blue dots indicate point sources identified by *WMAP*. In the map is labelled some well-known sources and regions (adopted from [49]).

are not well separated in that region. By contrast, the same model is preferred at high latitudes because of its strength.

The CMB intensity and polarization maps require masking since the observed maps are the combination of CMB with foreground residuals. The temperature and polarization masks are designed to eliminate the effect of regions containing significant residuals along the Galactic plane as well as foreground polarized sources. We report in Fig. 2.13 an overview of the microwave sky (see, [49]) showing the temperature and polarization analysis masks used for the *WMAP* mission. The construction of the Kp0, Kp2, and Kp8 diffuse emission masks is discussed in Bennett et al. [139]. The Kp0 and Kp2 masks are convenient for cosmological analysis. The Kp8 mask is based on the processing mask (see, [16]), which is designed to reduce the bias in the sky maps. The *WMAP* polarization mask P06 covers an important fraction of the sky (73%, [132]) since the polarized foreground emissions reside outside the Galactic plane as well. *Planck* polarization data will be released in 2014 but similar polarization mask based on the construction of *WMAP* can be applied for foreground subtractions. Following the masking of the residuals, the remaining fraction of the sky map produces likewise, a systematic error in the angular power spectrum that needs to be accounted for.

To summarize, the topics that we have introduced in this chapter are limited to the basics and essential backgrounds in order to understand the physical processes and mathematical treatments in the following chapters. We will make use of the expansion of the temperature and Stokes parameters

in spherical harmonics basis throughout this thesis and the estimator that we have defined by

$$C_l^{TE} = \frac{1}{2l+1} \sum_{m=-l}^{l} \langle a_{lm}^{T*} a_{lm}^{E} \rangle, \tag{2.36}$$

$$C_l^{EE} = \frac{1}{2l+1} \sum_{m=-l}^{l} \langle a_{lm}^{E*} a_{lm}^{E} \rangle, \tag{2.37}$$

will be used to estimate the power spectrum of the temperature and polarization anisotropies. We will investigate how the estimation of the power spectrum from the observations of the CMB anisotropies are connected to the systematics. We only focus the study on two of these systematics that we have reviewed in the last section of this chapter: the effect of the experiment beam asymmetry (non-circularity) and partial sky coverage resulting from the masking of foreground residuals. In particular, we will investigate the effects of CMB experiment beam asymmetry in the power spectrum estimation in the case of a full sky survey.

Chapter 3

Non-circular beam and full sky for TE polarized signals

3.1 Introduction

The main objective of any CMB experiment is to extract the primordial signature of the CMB anisotropies from the measured power spectrum of the total intensity (temperature) and polarization of the CMB radiation. This CMB anisotropy signal of cosmological origin is an imprint reflecting the state of the early Universe at the recombination epoch when the Universe became optically thin to radiation. Precise measurements of the angular power spectrum C_l of the CMB anisotropies allow to impose constraints on cosmological parameters. However, in realistic CMB experiments the signal is always disturbed by some systematics, and the power spectrum of the signal is affected by the variance of the systematic perturbing signals.

The non-circularity (asymmetry) of the instrument beam response is one of the most important source of errors in the estimation of the power spectrum of the CMB anisotropies. In this chapter, we address this problem and ignore the effects of the partial sky coverage and instrument noise as well as other systematics. Our goal is to calculate the bias in the estimation of the observed power spectrum when the experiment asymmetric beam is treated as circular. The bias is encoded in a matrix called *bias matrix* which relates the observed power spectrum to the true one. We focus on the derivation of this bias matrix for the TE cross-correlation. The idea is to convolve the true power spectrum, given by a fiducial model, with an asymmetric beam and make the comparison with the true power spectrum convolved with a circular beam of Gaussian shape. The difference between the above values will give an estimate of the bias caused by the non-circularity of the beam. Nevertheless, before we reach this step we need to derive, and then compute the TE bias matrix. During this process, it turned out that the main issue of the study has been the computational challenge involved in the numerical evaluation of the bias matrix.

Throughout this work and along with the remaining chapters we assume a trivial scanning strategy of *non-rotating* beam. The generalization of the results to more realistic scans will be part of our future research. In literature, many variants of estimators have been suggested in order to alleviate the computational cost of the bias matrix estimation. Among them, we cite the pseudo-C_l estimator based on semi-analytical methods [15, 19, 49, 66, 130, 140] in spherical harmonic space, full numerical integration [14, 141]; and the deconvolution of observed maps with asymmetric beams [142, 143]. For Planck-like experiment with non-trivial scan strategy, the beam systematic effect is assessed through the convolution of Monte Carlo simulated maps with the instrument beams [19]. However, the corresponding convolution algorithms in spherical harmonics space are relatively slow [144]. The spherical harmonic based "total convolution" algorithm (see, [22, 145]), for an idealized scan with a fixed orientation of the beam in each direction, scales as $\sim l_{max}^3 m_{max}$, where l_{max} is the highest multipole with non-negligible anisotropies contributions, and m_{max} is the highest azimuthal beam multipole needed for an adequate description of the beam asymmetry. The real space based "Fast Effective Beam Convolution in Pixel space" (FEBeCoP) method developed by Mitra et al. [19] has been implemented in *Planck* mission, with a computational cost that scales as $N_{pix} N_{beam}$, where N_{pix} is the total number of pixels in the map and N_{beam} is the number of pixels required to accurately describe the beam.

In the present chapter, we show that for a trivial scan of non-rotating beam, the computational cost of our spherical harmonic based algorithm scales as l_{max}. We will focus on the optimization of the computation time of the bias matrix, and investigate the effect of non-circular beams on the temperature and polarization (E-mode) power spectrum estimation with full sky coverage and noiseless limit, using the pseudo-C_l estimator. We extend the results of Fosalba et al. [66] by introducing the analytical tools developed by Mitra et al. [140] for the temperature anisotropies, and compute the bias matrix that encodes the power coupling at different multipoles as a result of the beam non-circularity.

3.2 Formalism

For the present formalism, we follow the approach developed in the paper of Mitra et al. [140] for the treatment of the total intensity of the radiation field and combine their method with the semi-analytical treatment of the polarized CMB radiation developed in the paper of Fosalba et al. [66]. The basic idea is to expand the total intensity (temperature) of the anisotropy field and polarized components of the CMB radiation in harmonic space and cross-correlate the multipole coefficients of the expansion in order to obtain a simple theoretical estimate of the power spectrum. The ensemble average will be used to construct the pseudo-C_l estimator. We expand the statistically Gaussian and isotropic temperature fluctuations $\Delta T(\hat{q})$ over all sky directions $\hat{q} = (\theta, \phi)$, on the

spherical harmonics basis as

$$\Delta T(\hat{q}) = \sum_{lm} a_{lm}^T Y_{lm}(\hat{q}) = \sum_{l=2}^{l_{max}} \sum_{m=-l}^{m=l} a_{lm}^T Y_{lm}(\hat{q}), \tag{3.1}$$

where a_{lm}^T are the coefficients of the temperature expansion in harmonic space. We apply the complex conjugate $Y_{l'm'}^*(\hat{q})$ of the spherical harmonic function in Eq. (3.1) and integrate over the solid angle of the sky $\Omega_{\hat{q}}$ to derive

$$\int d\Omega_{\hat{q}} \Delta T(\hat{q}) Y_{l'm'}^*(\hat{q}) = \sum_{lm} a_{lm}^T \int d\Omega_{\hat{q}} Y_{lm}(\hat{q}) Y_{l'm'}^*(\hat{q}), \tag{3.2}$$

and using the orthogonality and normalization relation (e.g., [146]) of the spherical harmonic function

$$\int d\Omega_{\hat{q}} Y_{lm}(\hat{q}) Y_{l'm'}^*(\hat{q}) = \delta_{ll'}\delta_{mm'}, \tag{3.3}$$

in which δ_{ij} denotes the Kronecker symbol, we obtain

$$a_{lm}^T = \int d\Omega_{\hat{q}} \Delta T(\hat{q}) Y_{lm}^*(\hat{q}), \tag{3.4}$$

where $d\Omega_{\hat{q}} = \sin\theta d\theta d\phi$. The above expression defines the multipoles a_{lm}^T as a function of the true temperature of the radiation field in spherical harmonic basis under the ideal systematic errors-free experiment assumption. In reality CMB experiments can only measure a disturbed temperature $\widetilde{\Delta T}(\hat{q})$ triggered by instrument systematic effects. In this condition the coefficients of the harmonic transform of the observed temperature $\widetilde{\Delta T}(\hat{q})$ take the form

$$\tilde{a}_{lm}^T = \int d\Omega_{\hat{q}} \widetilde{\Delta T}(\hat{q}) Y_{lm}^*(\hat{q}). \tag{3.5}$$

As we focus our study on the effects of the beam non-circularity (asymmetry) in CMB surveys, we will neglect in this chapter other systematics such as the cut-sky or non-uniformity of the sky due to the galactic mask applied in the foreground removal processes. In the case of a full sky survey and noiseless limit the observed temperature $\widetilde{\Delta T}(\hat{q})$ is the convolution of the true temperature $\Delta T(\hat{q})$ with the beam as

$$\widetilde{\Delta T}(\hat{q}) = \int d\Omega_{\hat{q}'} B(\hat{q}, \hat{q}') \Delta T(\hat{q}'), \tag{3.6}$$

where $B(\hat{q},\hat{q}')$ denotes the beam function. From Eq. (3.5) and Eq. (3.6) it follows that

$$\tilde{a}^T_{lm} = \int d\Omega_{\hat{q}} \int d\Omega_{\hat{q}'} B(\hat{q},\hat{q}')\Delta T(\hat{q}')Y^*_{lm}(\hat{q}). \tag{3.7}$$

We expand $\Delta T(\hat{q}')$ in the spherical harmonic space as

$$\Delta T(\hat{q}') = \sum_{l'm'} a_{l'm'}Y_{l'm'}(\hat{q}'), \tag{3.8}$$

and plug in Eq. (3.7) to derive the following form of the mutipole coefficients

$$\tilde{a}^T_{lm} = \sum_{l'm'} a^T_{l'm'} \int d\Omega_{\hat{q}} Y^*_{lm}(\hat{q}) \int d\Omega_{\hat{q}'} B(\hat{q},\hat{q}')Y_{l'm'}(\hat{q}'). \tag{3.9}$$

We may transform the above Eq. (3.9) by using the results of the integration of the beam function as referred to Eq. (24) of [140]

$$\begin{aligned}
\int d\Omega_{\hat{q}'} B(\hat{q},\hat{q}')Y^*_{l'm'}(\hat{q}') &= \sqrt{\frac{2l'+1}{4\pi}} \sum_{m''=-l'}^{l'} B_{l'}\beta_{l'm''}D^{l'}_{m'm''}(\hat{q},\rho(\hat{q})), \\
\int d\Omega_{\hat{q}'} B(\hat{q},\hat{q}')Y^*_{l'm'}(\hat{q}') &= \sum_{m''=-l'}^{l'} b^T_{l'm''}D^{l'}_{m'm''}(\hat{q},\rho(\hat{q})),
\end{aligned} \tag{3.10}$$

where

$$B_l = \int_{-1}^{1} d(\hat{q}.\hat{q}')P_l(\hat{q}.\hat{q}') \left[\frac{1}{2\pi}\int_0^{2\pi} d\phi\ B(\hat{z},\hat{q})\right]. \tag{3.11}$$

The beam distortion parameter defined as $\beta_{lm} = b^T_{lm}/b_{l0}$ describes the deviation of the beam from circularity and

$$b^T_{lm} = \int d\Omega_{\hat{q}}\ Y^*_{lm}(\hat{q})B(\hat{z},\hat{q}), \tag{3.12}$$

denotes the beam harmonic transform of the total intensity of the underlying anisotropy field. The terms $D^{l'}_{m'm''}(\hat{q},\rho(\hat{q}))$ in Eq. (3.10) are the Wigner-D functions given in terms of the Euler angles (θ,ϕ,ρ). The rotation angle $\rho(\hat{q})$ describes the rotation of the beam along the pointing direction $\hat{q}$ whereas $D^{l'}_{m'm''}(\hat{q},\rho(\hat{q}))$ accounts for the rotation that carries the pointing direction $\hat{q}$ to the North Pole $\hat{z}$ axis [130]. Eq. (3.11) includes the Legendre polynomials $P_l(\hat{q}.\hat{q}')$ and the instrument beam response $B(\hat{z},\hat{q})$ along the pointing direction $\hat{z}$. From Eq. (3.9) and Eq. (3.10) we derive the general form of the temperature harmonic transform as a function of the intensity beam harmonic

transform b^T_{lm} as

$$\tilde{a}^{T*}_{lm} = \sum_{l'm'} a^{T*}_{l'm'} \sum_{m''=-l'}^{l'} b^T_{l'm''} \int d\Omega_{\hat{q}} Y_{lm}(\hat{q}) D^{l'}_{m'm''}(\hat{q}, \rho(\hat{q})), \tag{3.13}$$

which will be used to estimate the cross-power spectrum TE.

For the E-component of the polarization field, we calculate the harmonic transform $\tilde{a}^E_{lm}$ using Fosalba et al. [66] approach by introducing the beam smoothed Stokes parameters Q_{eff} and U_{eff} on the spherical polar basis. The convolution of the beam with the sky can be expressed using Eq. (31) and Eq. (32) of [66] as

$$Q_{eff} = 2 \sum_{lmM} [D^l_{mM}(\hat{q}, \rho(\hat{q}))]^* \; b^{E*}_{lM} \; a^E_{lm}, \tag{3.14}$$

$$U_{eff} = 2 \sum_{lmM} [D^l_{mM}(\hat{q}, \rho(\hat{q}))]^* \; b^{E*}_{lM} \; a^B_{lm}, \tag{3.15}$$

where $|m| \leq l$, $|M| \leq l$. We adopt the E and B-mode notations in our formula which are connected to the gradient (G) and curl (C) components as $a^E_{lm} = -\sqrt{2}\; a^G_{lm}$ and $a^B_{lm} = -\sqrt{2}\; a^C_{lm}$. In the case of a symmetric (circular Gaussian) beam the Stokes parameters can be expanded in the spin-2 spherical harmonic basis ${}_{\mp 2}Y_{lm}(\hat{q})$ as

$$(Q \pm iU)(\hat{q}) = \sum_{lm} (a^E_{lm} \mp i a^B_{lm}) \; {}_{\mp 2}Y_{lm}(\hat{q}), \tag{3.16}$$

from which we derive the multipole coefficients of the polarization E-component given by

$$a^E_{lm} = \frac{1}{2} \int d\Omega_{\hat{q}} [(Q - iU)(\hat{q}) \; {}_2Y^*_{lm}(\hat{q}) + (Q + iU)(\hat{q}) \; {}_{-2}Y^*_{lm}(\hat{q})]. \tag{3.17}$$

We may obtain the sky multipoles of the non-circular beam $\tilde{a}^E_{lm}$ by plugging in Eq. (3.17) the effective smoothed Stokes parameters defined in Eq. (3.14) and Eq. (3.15), and after some algebra the final expression of the multipoles $\tilde{a}^E_{lm}$ reduces to

$$\begin{aligned} \tilde{a}^E_{lm} &= \int d\Omega_{\hat{q}} \sum_{l'm'} \sum_{M=-l'}^{l'} [D^{l'}_{m'M}(\hat{q}, \rho(\hat{q})) b^E_{l'M}]^* \; [a^E_{l'm'}(\; {}_2Y^*_{lm}(\hat{q}) + {}_{-2}\, Y^*_{lm}(\hat{q})) \\ &- i a^B_{l'm'}(\; {}_2Y^*_{lm}(\hat{q}) - {}_{-2}\, Y^*_{lm}(\hat{q}))]. \end{aligned} \tag{3.18}$$

From Eq. (3.13) and Eq. (3.18) we can cross-correlate the temperature T and the E-mode polarization in spherical harmonic space and get an estimate of the cross-power spectrum using the pseudo-C_l estimator which will be defined afterwards. In order to compute the two-point correlation

function we need to evaluate the beam spherical harmonic transform of the total intensity of the field and the polarized beams. We may pick up these beam corrections from the CMB experiment, though it is more convenient to simulate the instrument beam profile in order to investigate the effect of the beam systematics in the estimation of the TE power spectrum. In the next Section 3.3, we use the approach of Fosalba et al. [66] which describes the beam asymmetry model in the flat-sky approximation ($\theta \ll 1$ rad).

3.3 Beam spherical harmonic transform

In this section we use the results of [66] which give the explicit forms of the beam spherical harmonic transforms of the intensity and polarized beams. The approach is based on a perturbative expansion of an elliptical beam function $B(\theta, \phi)$ around a circular Gaussian beam in the flat-sky approximation, which provides a good approximation for single-dish experiments. The beam window function is expanded in real and harmonic space from which a semi-analytic model of the beam harmonic transform can be obtained. Following [66], the explicit form of the beam window function can be defined as

$$B(\theta, \phi) = B_0 \, \exp\left[-\frac{\theta^2}{2\sigma_b^2} f(\phi)\right], \tag{3.19}$$

in polar coordinates. The ellipticity parameter $\chi = 1-(\sigma_b/\sigma_a)^2$ of the window function is connected to the function

$$f(\phi) = 1 - \chi \, \cos^2(\phi - \omega), \tag{3.20}$$

which describes the deviation of the beam from a circular (axisymmetric) one. σ_a and σ_b denote the beam widths along the major and minor axis. The expansion of the window function in spherical harmonic space reads

$$B(\theta, \phi) = \sum_{l=2}^{l_{max}} \sum_{m=-l}^{l} b_{lm} Y_{lm}(\theta, \phi), \tag{3.21}$$

from which we obtain the beam harmonic transform b_{lm}

$$b_{lm} = \int d\Omega B(\theta, \phi) Y^*_{lm}(\theta, \phi), \tag{3.22}$$

where Ω is the total solid angle over the sky. It is shown in [66] that Eq. (3.22) can be solved using a semi-analytical framework in the flat-sky approximation. Although a full numerical integration can be performed (see, [15]) to evaluate the integral involved in Eq. (3.22), the rapidly converging semi-analytical approach is largely sufficient for our purpose. We use the eccentricity $e = \sqrt{\chi}$ and

the geometric mean beam width of the elliptic Gaussian window defined by

$$\sigma = \sqrt{\sigma_a \sigma_b} = \frac{\pi}{180} \frac{\theta_{FWHM}}{\sqrt{8\ln 2}}, \tag{3.23}$$

to adequately describe the beam geometry where $\theta_{\rm FWHM}$ (in degrees) denotes the full width at half maximum of the beam Gaussian profile. The ellipticity of the beam is defined by $\epsilon = \sigma_a/\sigma_b$ (not to be confounded with the ellipticity parameter $\chi = 1 - 1/\epsilon^2$).

The harmonic expansion coefficients of the beam defined in Eq. (3.22) have symmetry properties which greatly simplify the numerical implementation. As mentioned in [66] only the even m modes have non-vanishing contribution in the beam transform as a consequence of the azimuthal symmetry of the term $\cos^2(\phi)$ which appears in the function $f(\phi)$. As a result of the property of the spherical harmonic complex conjugate $Y^*_{lm}(\theta, \phi)$, it follows that $b^*_{lm} = (-1)^m b_{l-m}$, and from the reality condition of the beam harmonic transform $b^*_{lm} = b_{lm}$. This implies that $b_{lm} = b_{l-m}$ so that negative and positive modes have the same contribution. We adopt the beam models of [66] that will allow us to compute numerically the bias matrix which describes the power coupling between multipoles. For the temperature, the harmonic transform of the beam with second order in the parameter ellipticity χ is computed with the formula (A20) of [66] as follows

$$\begin{aligned}
b^T_{l0} &= \sqrt{\frac{2l+1}{4\pi}} e^{-\frac{l^2\sigma^2}{2}} \left[1 - \frac{\chi}{4} l^2\sigma^2 + \frac{\chi^2}{4}\left(-l^2\sigma^2 + \frac{3}{16} l^4\sigma^4\right)\right], \\
b^T_{l2} &= \sqrt{\frac{2l+1}{4\pi}} \frac{\chi}{8} l^2\sigma^2 e^{-\frac{l^2\sigma^2}{2}} \left[1 + \chi\left(1 - \frac{1}{4} l^2\sigma^2\right)\right], \\
b^T_{l4} &= \sqrt{\frac{2l+1}{4\pi}} \frac{\chi^2}{128} l^4\sigma^4 e^{-\frac{l^2\sigma^2}{2}},
\end{aligned} \tag{3.24}$$

and the linear polarized beam transforms with the same order expansion is obtained by using the simple relation $b^E_{l2} = b^T_{l0}/2$, $b^E_{l4} = b^T_{l2}/2$ and $b^E_{l6} = b^T_{l4}/2$.

We limit the perturbative expansion for both intensity and polarized beam to three terms which provide sufficient accuracy for experiments with mildly non-circular (asymmetric) beam. Under this prescription, the precision that can be achieved is $\sim 1\%$ till the multipole $l_{max} = 5 l_{peak}$ (for $\theta_{\rm FWHM} = 10'$ and $\epsilon = 1.3$) where l_{peak} defined as $\sigma^2 l^2_{peak} \simeq (1 - \chi/4)$ is the multipole where the window function peaks (see, Fosalba et al. [66]). As inferred from Eq. (3.13) and Eq. (3.18), the correlation between T and E in harmonic space involves the product $b^T_{lm} b^E_{lm}$ which is illustrated in Fig. 3.1. Clearly, the effect of higher order corrections (m=2, 4 modes for T and m=4, 6 modes for E) due to the beam non-circularity (asymmetry) is significant for $l\sigma \sim 1$. Providing the analytical expansion of the beam total intensity and the E- polarized beams, we are able to compute the correlation between the sky harmonic coefficients defined in Eq. (3.13) and Eq. (3.18)

and thereafter, the power spectrum of TE. We will use the pseudo-C_l method to estimate the power spectrum whose advantage will be justified in the following Section 3.4.

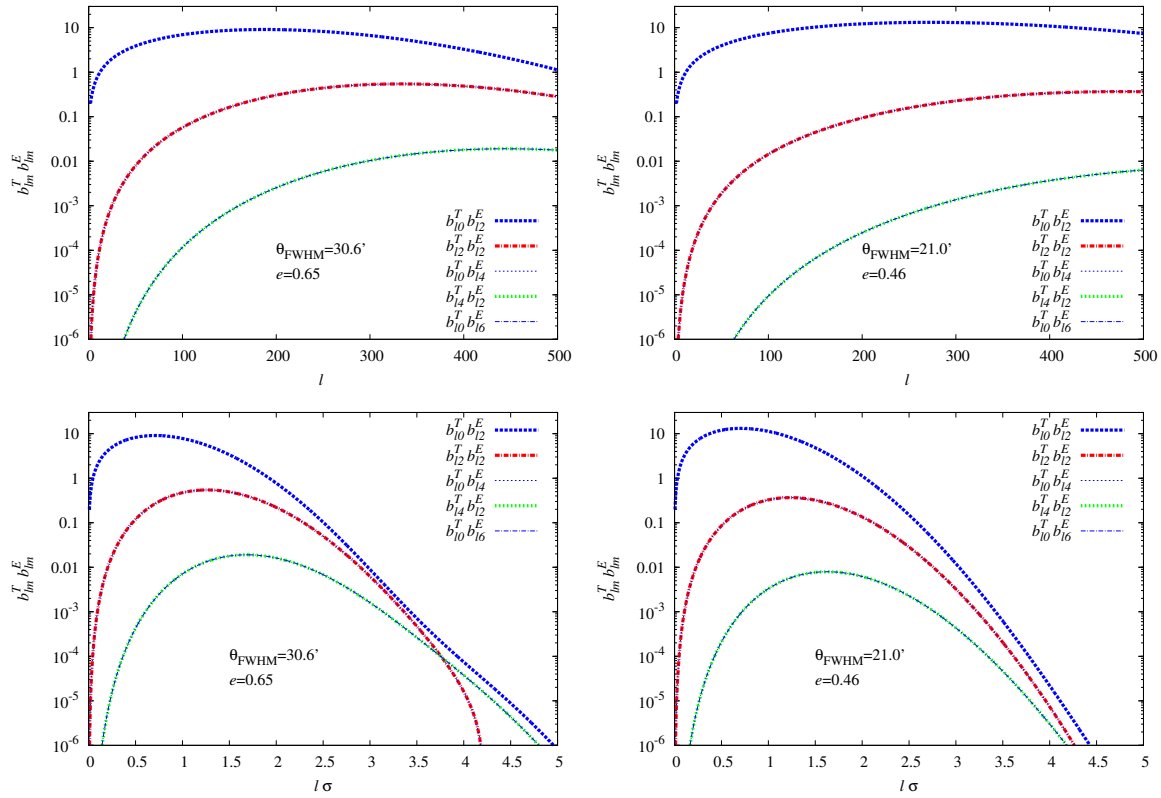

Figure 3.1: Product of the temperature T and the E-polarized beam harmonic transforms. The top left panel shows the variation as a function of the multipole l for a beam width $\theta_{\rm FWHM} = 30.6'$ and eccentricity $e = 0.65$ corresponding to the *WMAP*- Q1 beam parameters model limited to $l_{max} = 500$, and the bottom left panel illustrates the same product plotted against $l\sigma$. We show on the right panel the product of the beam transforms corresponding to the *WMAP*- V beam with a beam width $\theta_{\rm FWHM} = 21.0'$ and eccentricity $e = 0.46$ plotted against the multipole l (top right panel) and $l\sigma$ (bottom right panel). The first leading terms of the beam harmonic products (the blue thick dotted lines) are connected to the circulary symmetric Gaussian window. The relation $b^E_{lm} = b^T_{lm-2}/2$ (m=2, 4, 6) implies that each of the second and third leading terms (non-circularity corrections) of the beam harmonic products incorporate two terms with the same amplitude which are illustrated with the overlapping dotted and dot-dashed lines. Note that the peak shifts to higher l for higher order corrections and becomes important for $l\sigma \sim 1$.

3.4 The bias matrix

Different methods have been proposed to estimate the power spectrum of the CMB anisotropies. Among them, the optimal maximum likelihood estimator [24–27] is the most commonly used, but the huge computational cost makes it just unfeasible for high-resolution CMB experiments which probe small angular scales on the sky. Therefore, we adopt the alternative suboptimal pseudo-C_l approach to estimate the power spectrum. Unlike the maximum likelihood, the pseudo-C_l method is not an exact estimator, though it has the advantage of being relatively fast and can be exploited to process *Planck*-like CMB large data sets in a reasonable time.

The pseudo-C_l estimator of the TE power spectrum is defined by

$$C_l^{TE} = \frac{1}{2l+1} \sum_{m=-l}^{l} a_{lm}^{T} a_{lm}^{E*}. \tag{3.25}$$

This suboptimal estimator is qualified as "pseudo" in the sense that it is biased. In order to obtain an accurate estimation of CMB experiments power spectrum, we must account for the systematic effects due to the beam asymmetry, the instrumental noise and the non-uniform/cut-sky [130] besides other systematics such as the telescope scanning and pointing errors, gain and calibration, power leakage between E and B-modes and the B-mode induced by the gravitational lensing of the CMB by large scale structure, in the case of the B-mode polarization autocorrelation. For now, we investigate the effect of the beam asymmetry in the case of a complete sky coverage. The extension to the cut-sky using non-circular beams will be developed in Chapter 4.

The expectation value of the pseudo-C_l estimator is related to the true power spectrum $C_{l'}^{TE}$ as

$$\langle \tilde{C}_l^{TE} \rangle = \sum_{l'} A_{ll'}^{TE} C_{l'}^{TE}, \tag{3.26}$$

where $\langle \tilde{C}_l^{TE} \rangle$ denotes the ensemble average of the power spectrum over all realizations on the sky. The term $A_{ll'}^{TE}$ is the multipoles coupling matrix which represents the bias (with respect to a circular Gaussian profile) that will affect the estimation of the TE power spectrum when the beam pattern is asymmetric. From Eq. (3.25) we can write the expectation value of the cross-power spectrum TE as

$$\begin{aligned} \langle \tilde{C}_l^{TE} \rangle &= \frac{1}{2l+1} \sum_{m=-l}^{l} \langle \tilde{a}_{lm}^{T} \tilde{a}_{lm}^{E*} \rangle, \\ &= \frac{1}{2l+1} \sum_{m=-l}^{l} \langle \tilde{a}_{lm}^{T*} \tilde{a}_{lm}^{E} \rangle. \end{aligned} \tag{3.27}$$

We substitute Eq. (3.13) and Eq. (3.18) into Eq. (3.27) to obtain the ensemble average of the power spectrum which reads

$$\begin{aligned}\langle \tilde{C}_l^{TE} \rangle &= \frac{1}{2l+1} \sum_{m=-l}^{l} \sum_{l'm'l'_1m'_1} \langle a^{T*}_{l'm'} a^{E}_{l'_1m'_1} \rangle \sum_{m''=-l'}^{l'} b^{T}_{l'm''} \int d\Omega_{\hat{q}} Y_{lm}(\hat{q}) D^{l'}_{m'm''}(\hat{q}, \rho(\hat{q})) \\ &\times \sum_{M=-l'_1}^{l'_1} b^{E}_{l'_1 M} \int d\Omega_{\hat{q}} [D^{l'_1}_{m'_1 M}(\hat{q}, \rho(\hat{q}))]^* ({}_2Y^*_{lm}(\hat{q}) + {}_{-2}Y^*_{lm}(\hat{q})). \end{aligned} \tag{3.28}$$

Then, we use the statistical isotropy of the CMB anisotropy

$$\langle a^{T*}_{l'm'} \, a^{E}_{l'_1m'_1} \rangle = C^{TE}_{l'} \, \delta_{l'l'_1} \delta_{m'm'_1}, \tag{3.29}$$

$$\langle a^{T*}_{l'm'} \, a^{B}_{l'_1m'_1} \rangle = C^{TB}_{l'} \, \delta_{l'l'_1} \delta_{m'm'_1} = 0, \tag{3.30}$$

to derive the following expression

$$\begin{aligned}\langle \tilde{C}_l^{TE} \rangle &= \frac{1}{2l+1} \sum_{m=-l}^{l} \sum_{l'm'} C^{TE}_{l'} \sum_{m''=-l'}^{l'} b^{T}_{l'm''} \int d\Omega_{\hat{q}} Y_{lm}(\hat{q}) D^{l'}_{m'm''}(\hat{q}, \rho(\hat{q})) \\ &\times \sum_{M=-l'}^{l'} b^{E}_{l'M} \left[\int d\Omega_{\hat{q}} ({}_2Y_{lm}(\hat{q}) D^{l'}_{m'M}(\hat{q}, \rho(\hat{q})) + {}_{-2}Y_{lm}(\hat{q}) D^{l'}_{m'M}(\hat{q}, \rho(\hat{q})) \right]^* \\ &= \frac{1}{2l+1} \sum_{m=-l}^{l} \sum_{l'm'} C^{TE}_{l'} \sum_{m''=-l'}^{l'} b^{T}_{l'm''} I_1 \sum_{M=-l'}^{l'} b^{E}_{l'M} (I_2 + I_3)^*, \end{aligned} \tag{3.31}$$

where we define the integrals I_1, I_2, and I_3 as

$$I_1 = \int d\Omega_{\hat{q}} \; Y_{lm}(\hat{q}) D^{l'}_{m'm''}(\hat{q}, \rho(\hat{q})), \tag{3.32}$$

$$I_2 = \int d\Omega_{\hat{q}} \;\; {}_2Y_{lm}(\hat{q}) D^{l'}_{m'M}(\hat{q}, \rho(\hat{q})), \tag{3.33}$$

$$I_3 = \int d\Omega_{\hat{q}} \;\; {}_{-2}Y_{lm}(\hat{q}) D^{l'}_{m'M}(\hat{q}, \rho(\hat{q})). \tag{3.34}$$

The above integrals depend on the scanning strategy of the CMB survey through the function $\rho(\hat{q})$ which defines the rotation of the beam along the pointing direction of the telescope. We will show that under some assumptions on this scanning pattern, the integrals I_1, I_2 and I_3 can be solved analytically. We report in Appendix (B) the derivations of the integrals I_1, I_2, and I_3. By replacing the integrals I_1, I_2 and I_3 into Eq. (3.31) we get the following expression of the expectation value

of the power spectrum

$$\begin{aligned}\langle \tilde{C}_l^{TE} \rangle &= \frac{1}{2l+1} \sum_{m=-l}^{l} \sum_{l'm'} C_{l'}^{TE} \sum_{m''=-l'}^{l'} b_{l'm''}^{T} (-1)^m \sqrt{\frac{2l+1}{4\pi}} \sum_{L=|l-l'|}^{l+l'} C_{l-ml'm'}^{L(-m+m')} C_{l0l'm''}^{Lm''} \\ &\times \int d\Omega_{\hat{q}} D^{L}_{(-m+m')m''}(\hat{q}, \rho(\hat{q})) \sum_{M=-l'}^{l'} b_{l'M}^{E} (-1)^m \sqrt{\frac{2l+1}{4\pi}} \sum_{L'=|l-l'|}^{l+l'} C_{l-ml'm'}^{L'(-m+m')} \\ &\times \left[C_{l2l'M}^{L'(2+M)} \int d\Omega_{\hat{q}} D^{L'}_{(-m+m')(2+M)}(\hat{q}, \rho(\hat{q})) \right. \\ &+ \left. C_{l-2l'M}^{L'(-2+M)} \int d\Omega_{\hat{q}} D^{L'}_{(-m+m')(-2+M)}(\hat{q}, \rho(\hat{q})) \right]^*, \end{aligned} \tag{3.35}$$

which can be simplified in the form

$$\begin{aligned}\langle \tilde{C}_l^{TE} \rangle &= \frac{1}{4\pi} \sum_{m=-l}^{l} \sum_{l'm'} C_{l'}^{TE} \sum_{m''=-l'}^{l'} b_{l'm''}^{T} \sum_{L=|l-l'|}^{l+l'} C_{l-ml'm'}^{L(-m+m')} C_{l0l'm''}^{Lm''} \\ &\times \int d\Omega_{\hat{q}} D^{L}_{(-m+m')m''}(\hat{q}, \rho(\hat{q})) \sum_{M=-l'}^{l'} b_{l'M}^{E} \sum_{L'=|l-l'|}^{l+l'} C_{l-ml'm'}^{L'(-m+m')} \\ &\times \left[C_{l2l'M}^{L'(2+M)} \int d\Omega_{\hat{q}} D^{L'}_{(-m+m')(2+M)}(\hat{q}, \rho(\hat{q})) \right. \\ &+ \left. C_{l-2l'M}^{L'(-2+M)} \int d\Omega_{\hat{q}} D^{L'}_{(-m+m')(-2+M)}(\hat{q}, \rho(\hat{q})) \right]^*. \end{aligned} \tag{3.36}$$

In the following we propose to compute the integral

$$\chi^{l}_{mm'}[\rho(\hat{q})] = \int d\Omega_{\hat{q}} D^{l}_{mm'}(\hat{q}, \rho(\hat{q})), \tag{3.37}$$

involved in Eq. (3.36) which depends on the scanning strategy of the CMB experiment. We can evaluate $\chi^{l}_{mm'}[\rho(\hat{q})]$ using [140] approach. We consider a beam rotation $\rho(\hat{q})$ which can be decomposed into declination and right ascension parts $\rho(\hat{q}) = \Theta(\theta) + \Phi(\phi)$ as it provides a good approximation of real scan strategies. Using Eq. (1), Section 4.3 of [146] we write

$$D^{l}_{mm'}(\hat{q}, \rho(\hat{q})) = e^{-im\phi} d^{l}_{mm'}(\theta) e^{-im'\rho}, \tag{3.38}$$

where $d^{l}_{mm'}(\theta)$ denotes the Wigner-d function. $\chi^{l}_{mm'}[\rho(\hat{q})]$ takes the form

$$\chi^{l}_{mm'}[\rho(\hat{q})] = \int_0^{2\pi} d\phi e^{-im'\Phi(\phi)} \int_0^{\pi} d\theta \, \sin\theta \; d^{l}_{mm'}(\theta) e^{-im'\Theta(\theta)}, \tag{3.39}$$

which contributes significantly only for constrained values of m'.

For an equal declination scan $\rho(\hat{q}) = \rho(\theta)$, and the integral $\chi^l_{mm'}[\rho(\hat{q})]$ reduces to

$$\begin{aligned}\chi^l_{mm'}[\rho(\theta)] &= 2\pi\delta_{m0}\int_0^\pi d\theta\ \sin\theta\ d^l_{mm'}(\theta)e^{-im'\rho(\theta)},\\ &= \chi^l_{0m'}[\rho(\theta)],\end{aligned} \tag{3.40}$$

where the Wigner-d function $d^l_{0m'}(\theta)$ (since the only non-vanishing terms are obtained for $m = 0$) can be evaluated using Eq. (E15) of [140] as

$$d^l_{0m'}(\theta) = i^{m'}\sum_{N=-l}^{l}\left[(-1)^N d^l_{0N}(\frac{\pi}{2})e^{iN\theta}d^l_{Nm'}(\frac{\pi}{2})\right]. \tag{3.41}$$

Thus, we may write

$$\begin{aligned}\chi^l_{0m'}[\rho(\theta)] &= 2\pi\sum_{N=-l}^{l} d^l_{0N}(\frac{\pi}{2})d^l_{Nm'}(\frac{\pi}{2})i^{m'}(-1)^N\int_0^\pi d\theta\ \sin\theta\ e^{iN\theta}e^{-im'\rho(\theta)},\\ &= 2\pi\sum_{N=-l}^{l} d^l_{0N}(\frac{\pi}{2})d^l_{Nm'}(\frac{\pi}{2})\Gamma_{m'N}[\rho(\theta)],\end{aligned} \tag{3.42}$$

where

$$\Gamma_{m'N}[\rho(\theta)] = i^{m'}(-1)^N\int_0^\pi d\theta\ \sin\theta\ e^{iN\theta}e^{-im'\rho(\theta)}. \tag{3.43}$$

Mitra et al. [140] show that only the real parts of $\Gamma_{m'N}[\rho(\theta)]$ contribute in most of the cases where the general shape of the beam and the scan strategies exhibit trivial symmetries. For non-rotating beam $\rho(\hat{q}) = 0$, and the real part of the Γ coefficients reduces to Eq. (38) of [140] expressed as follows

$$\Re\left[\Gamma_{m'N}[\rho(\hat{q}) = 0]\right] = f_{m'N} = \begin{cases} (-1)^{(m'\pm1)/2}\,\pi/2 & \text{if } m'\text{=odd and } N = \pm1\\ (-1)^{m'/2}\,2/(1-N^2) & \text{if both } m', N = 0 \text{ or even}\\ 0 & \text{otherwise.}\end{cases} \tag{3.44}$$

We apply the property obtained in Eq. (E.9) and the relation given in Eq. (3.42) to derive the

following quantities assuming that the beam is non-rotating.

$$\int d\Omega_{\hat{q}} D^{L}_{(-m+m')m''}(\hat{q},\rho(\hat{q})) = 2\pi \sum_{M=-L}^{L} d^{L}_{0M}(\frac{\pi}{2}) d^{L}_{Mm''}(\frac{\pi}{2}) f_{m''M}, \tag{3.45}$$

$$\int d\Omega_{\hat{q}} D^{L'}_{(-m+m')(2+M)}(\hat{q},\rho(\hat{q})) = 2\pi \sum_{N=-L'}^{L'} d^{L'}_{0N}(\frac{\pi}{2}) d^{L'}_{N(2+M)}(\frac{\pi}{2}) f_{(2+M)N}, \tag{3.46}$$

$$\int d\Omega_{\hat{q}} D^{L'}_{(-m+m')(-2+M)}(\hat{q},\rho(\hat{q})) = 2\pi \sum_{N=-L'}^{L'} d^{L'}_{0N}(\frac{\pi}{2}) d^{L'}_{N(-2+M)}(\frac{\pi}{2}) f_{(-2+M)N}. \tag{3.47}$$

Eq. (E.9) implies that the only non-vanishing terms from the above integrals are obtained for $m' = m$. After some algebra the general expression of the bias matrix for an equal declination scan strategy can be derived from Eq. (3.36) in the form

$$\begin{aligned} A^{TE}_{ll'} &= \pi \sum_{m=-l}^{l} \sum_{m''=-l'}^{l'} b^{T}_{l'm''} \sum_{L=|l-l'|}^{l+l'} C^{L0}_{l-ml'm} C^{Lm''}_{l0l'm''} \sum_{M=-L}^{L} d^{L}_{0M}(\frac{\pi}{2}) d^{L}_{Mm''}(\frac{\pi}{2}) \Gamma_{m''M}[\rho(\theta)] \\ &\times \sum_{M'=-l'}^{l'} b^{E}_{l'M'} \sum_{L'=|l-l'|}^{l+l'} C^{L'0}_{l-ml'm} \Bigg[C^{L'(2+M')}_{l2l'M'} \sum_{N=-L'}^{L'} d^{L'}_{0N}(\frac{\pi}{2}) d^{L'}_{N(2+M')}(\frac{\pi}{2}) \Gamma_{(2+M')N}[\rho(\theta)] \\ &+ C^{L'(-2+M')}_{l-2l'M'} \sum_{N=-L'}^{L'} d^{L'}_{0N}(\frac{\pi}{2}) d^{L'}_{N(-2+M')}(\frac{\pi}{2}) \Gamma_{(-2+M')N}[\rho(\theta)] \Bigg], \end{aligned} \tag{3.48}$$

and for the particular case of a non-rotating beam ($\Gamma_{m'N}[\rho(\hat{q}) = 0] = f_{m'N}$) the bias matrix takes the form

$$\begin{aligned} A^{TE}_{ll'} &= \pi \sum_{m=-l}^{l} \sum_{m''=-l'}^{l'} b^{T}_{l'm''} \sum_{L=|l-l'|}^{l+l'} C^{L0}_{l-ml'm} C^{Lm''}_{l0l'm''} \sum_{M=-L}^{L} d^{L}_{0M}(\frac{\pi}{2}) d^{L}_{Mm''}(\frac{\pi}{2}) f_{m''M} \\ &\times \sum_{M'=-l'}^{l'} b^{E}_{l'M'} \sum_{L'=|l-l'|}^{l+l'} C^{L'0}_{l-ml'm} \Bigg[C^{L'(2+M')}_{l2l'M'} \sum_{N=-L'}^{L'} d^{L'}_{0N}(\frac{\pi}{2}) d^{L'}_{N(2+M')}(\frac{\pi}{2}) f_{(2+M')N} \\ &+ C^{L'(-2+M')}_{l-2l'M'} \sum_{N=-L'}^{L'} d^{L'}_{0N}(\frac{\pi}{2}) d^{L'}_{N(-2+M')}(\frac{\pi}{2}) f_{(-2+M')N} \Bigg], \end{aligned} \tag{3.49}$$

which after rearrangement of the beam harmonic transforms product $b^T_{l'm''}b^E_{l'M'}$ yield

$$
\begin{aligned}
A^{TE}_{ll'} &= \pi \sum_{m=-l}^{l} \sum_{m''=-l'}^{l'} \sum_{M'=-l'}^{l'} b^T_{l'm''} b^E_{l'M'} \\
&\times \sum_{L=|l-l'|}^{l+l'} C^{L0}_{l-ml'm}\, C^{Lm''}_{l0l'm''} \sum_{M=-L}^{L} d^L_{0M}(\frac{\pi}{2}) d^L_{Mm''}(\frac{\pi}{2}) f_{m''M} \sum_{L'=|l-l'|}^{l+l'} C^{L'0}_{l-ml'm} \\
&\times \Bigg[C^{L'(2+M')}_{l2l'M'} \sum_{N=-L'}^{L'} d^{L'}_{0N}(\frac{\pi}{2}) d^{L'}_{N(2+M')}(\frac{\pi}{2}) f_{(2+M')N} \\
&+ C^{L'(-2+M')}_{l-2l'M'} \sum_{N=-L'}^{L'} d^{L'}_{0N}(\frac{\pi}{2}) d^{L'}_{N(-2+M')}(\frac{\pi}{2}) f_{(-2+M')N} \Bigg],
\end{aligned}
\tag{3.50}
$$

where $m'' = 0, \pm 2, \pm 4$ and $M' = \pm 2, \pm 4, \pm 6$ are the modes corresponding to the total intensity and polarized beam transforms with second order in ellipticity.

Eq. (3.50) constitutes one of the main results of this chapter. It provides the most general form of the bias matrix for a non-circular (asymmetric) beam in the case of a full sky coverage with non-rotating beam. We can see from Eq. (3.48) and Eq. (3.50) that the computational cost of the bias matrix for an equal declination scan is equivalent to that of the non-rotating beam as we only need to precompute the coefficients $\Gamma_{m'N}[\rho(\theta)]$ and $f_{m'N}$ for the corresponding scan strategies. As a result of the constraint on m in Eq. (E.9) and as discussed in the paper of Mitra et al. [140], we can expect that the bias matrix computation for real scan strategies is computationally equivalent to the bias computation for non-rotating beam.

3.5 Numerical implementation

The bias matrix defined in Eq. (3.50) contains implicit information about the coupling of power between multipoles as a result of the beam asymmetry. A detailed study of the effect of the non-circularity of the beam in the power spectrum estimation requires numerous and repeated computations of the bias matrix with different beam parameters (beam width and eccentricity) at each step of the computation. However, the numerical evaluation of the algebraic expression in Eq. (3.50) is a computational challenge. A naive numerical implementation of the formula Eq. (3.50) that involves six loops, would scale as $O(l^6_{max})$, which quickly becomes prohibitive at large multipoles (smaller angular resolution). In this section, we will tackle this issue and estimate the computational cost of the evaluation of the bias matrix.

To begin with, we decompose the summations involved in Eq. (3.50) in order to split the bias matrix into several ones in which, separately appear the beam harmonic transforms product $b^T_{lm}b^E_{lm}$

introduced in Section 3.3. Therefore, Eq. (3.50) can be written as follows

$$A_{ll'}^{TE} = A_{ll'}^{TE}(term\ 1) + A_{ll'}^{TE}(term\ 2) + A_{ll'}^{TE}(term\ 3) + A_{ll'}^{TE}(term\ 4) + A_{ll'}^{TE}(term\ 5), \quad (3.51)$$

where each term of the bias matrix derived from Eq. (3.50) is given explicitly in Appendix C.

The first term $A_{ll'}^{TE}(term\ 1)$ is the bias corresponding to the leading term $b_{l0}^{T} b_{l2}^{E}$ of the harmonics product. We will show in Appendix A that this term reduces to the well known [145, 147] window function for a circular (axisymmetric) Gaussian beam which reads

$$A_{ll'}^{TE}(term\ 1) = e^{-l^2\sigma^2}\delta_{ll'}. \quad (3.52)$$

Hereafter, we will introduce the symmetry properties of the Wigner-d functions that allow us to considerably reduce the number of operations involved in the computation of the summations of kind $\sum_{N=-l}^{l}$. We define the quantities

$$d(L', m') = \sum_{N=-L'}^{L'} d(L', N, m'), \quad (3.53)$$

where

$$d(L', N, m') = d_{0N}^{L'}(\frac{\pi}{2}) d_{Nm'}^{L'}(\frac{\pi}{2}) f_{m'N}, \quad (3.54)$$

for $m' = \pm 2,\ \pm 4,\ \pm 6$. We notice that the function $f_{m'N}$ involved in Eq. (3.44) that describes the non-rotating beam scanning strategy, is of even parity with respect to N, i.e., $f_{m'-N} = f_{m'N}$. From the following symmetry relations of the Wigner-d function (Eq. (1), Section 4.4 of [146])

$$d_{0-N}^{L'}(\frac{\pi}{2}) = (-1)^N d_{0N}^{L'}(\frac{\pi}{2}) = (-1)^{L'} d_{0N}^{L'}(\frac{\pi}{2}), \quad (3.55)$$

$$d_{-Nm'}^{L'}(\frac{\pi}{2}) = (-1)^{L'-m'} d_{Nm'}^{L'}(\frac{\pi}{2}), \quad (3.56)$$

we may write that

$$d_{0-N}^{L'}(\frac{\pi}{2}) d_{-Nm'}^{L'}(\frac{\pi}{2}) f_{m'-N} = (-1)^{m'} d_{0N}^{L'}(\frac{\pi}{2}) d_{Nm'}^{L'}(\frac{\pi}{2}) f_{m'N}, \quad (3.57)$$

which translates to

$$d(L', -N, m') = (-1)^{m'} d(L', N, m'), \quad (3.58)$$

and finally by plugging in Eq. (3.53), the above relations imply

$$d(L', m') = d^{L'}_{00}(\frac{\pi}{2}) d^{L'}_{0m'}(\frac{\pi}{2}) f_{m'0} + \sum_{N=1}^{L'} ((-1)^{m'} + 1) d^{L'}_{0N}(\frac{\pi}{2}) d^{L'}_{Nm'}(\frac{\pi}{2}) f_{m'N}, \tag{3.59}$$

which is valid for the different values of m'.

We can see from Eq. (3.59) that instead of $2L'$ additions, only L' operations are necessary for the computation of each summation of the form defined by Eq. (3.53). In this way, we will gain a computational improvement by a factor of two. Analogously, the evaluation of the terms $A^{TE}_{ll'}(term\ 2)$, $A^{TE}_{ll'}(term\ 3)$, $A^{TE}_{ll'}(term\ 4)$ and $A^{TE}_{ll'}(term\ 5)$ can be carried out by following the same algebra formalism exposed in Appendix A where we treat a detailed derivation of the term $A^{TE}_{ll'}(term\ 1)$. Furthermore, we can reduce the number of addition operations by including the Clebsch-Gordan coefficients symmetry properties. We notice that each term of the bias matrix contains the summation $\sum_{m=-l}^{l} C^{L0}_{l-ml'm}$ which can be written using Eq. (11), Section 8.4.3 of [146] as

$$\begin{aligned} c(l, l', L) &= \sum_{m=-l}^{l} C^{L0}_{l-ml'm}, & (3.60)\\ &= \sum_{m=-min(l,\ l')}^{min(l,\ l')} C^{L0}_{l-ml'm}, & (3.61)\\ &= C^{L0}_{l0l'0} + ((-1)^L + 1) \sum_{m=1}^{min(l,\ l')} (-1)^m C^{L0}_{l-ml'm}, & (3.62) \end{aligned}$$

which again reduces by a factor of two the operations needed for the summations. Putting all together and introducing the new notations introduced in Eq. (3.53) and Eq. (3.60), we resume

the expression of the different terms of the bias matrix as follows

$$A_{ll'}^{TE}(term\ 1) = e^{-l^2\sigma^2}\ \delta_{ll'}, \tag{3.63}$$

$$A_{ll'}^{TE}(term\ 2) = \frac{4\pi}{2l+1} b_{l'2}^T b_{l'2}^E \sum_{L=|l-l'|}^{l+l'} C_{l0l'2}^{L2}\ \left((-1)^L d(L,-2) + d(L,2)\right)\ c(l,l',L), \tag{3.64}$$

$$\begin{aligned} A_{ll'}^{TE}(term\ 3) &= \frac{2\pi}{2l+1} b_{l'0}^T b_{l'4}^E \sum_{L=|l-l'|}^{l+l'} \left[C_{l-2l'4}^{L2}\ \left((-1)^L d(L,-2) + d(L,2)\right)\right. \\ &+ \left. C_{l2l'4}^{L6}\ \left((-1)^L d(L,-6) + d(L,6)\right)\right] c(l,l',L), \end{aligned} \tag{3.65}$$

$$A_{ll'}^{TE}(term\ 4) = \frac{4\pi}{2l+1} b_{l'4}^T b_{l'2}^E \sum_{L=|l-l'|}^{l+l'} C_{l0l'4}^{L4}\ \left((-1)^L d(L,-4) + d(L,4)\right) c(l,l',L), \tag{3.66}$$

$$\begin{aligned} A_{ll'}^{TE}(term\ 5) &= \frac{2\pi}{2l+1} b_{l'0}^T b_{l'6}^E \sum_{L=|l-l'|}^{l+l'} \left[C_{l-2l'6}^{L4}\ \left((-1)^L d(L,-4) + d(L,4)\right)\right. \\ &+ \left. C_{l2l'6}^{L8}\ \left((-1)^L d(L,-8) + d(L,8)\right)\right] c(l,l',L). \end{aligned} \tag{3.67}$$

In order to compute efficiently the bias matrix, we need to simplify as much as possible the above formula. We further proceed with the algorithm implementation by introducing the new quantities

$$dm'(L) = (-1)^L d(L,-m') + d(L,m'), \tag{3.68}$$

which will greatly ease the computation as they appear several times in the bias matrix expressions ($m' = 2,\ 4,\ 6,\ 8$). As the above quantities can be precomputed, we can expect a fast computation of the bias matrix with a reasonable time. At this step, the summation of the bias matrix terms reduces to the following relation

$$\begin{aligned} A_{ll'}^{TE} &= e^{-l^2\sigma^2}\ \delta_{ll'} \\ &+ \frac{4\pi}{2l+1} \sum_{L=|l-l'|}^{l+l'} \left[b_{l'2}^T b_{l'2}^E\ C_{l0l'2}^{L2} d2(L) + \frac{1}{2} b_{l'0}^T b_{l'4}^E \left(C_{l-2l'4}^{L2} d2(L) + C_{l2l'4}^{L6} d6(L)\right)\right. \\ &+ \left. b_{l'4}^T b_{l'2}^E\ C_{l0l'4}^{L4} d4(L) + \frac{1}{2} b_{l'0}^T b_{l'6}^E \left(C_{l-2l'6}^{L4} d4(L) + C_{l2l'6}^{L8} d8(L)\right)\right] c(l,l',L). \end{aligned} \tag{3.69}$$

We will employ the simplified form Eq. (3.69) of the bias matrix and estimate the computation time involved in the process. The Clebsch-Gordan coefficients can be computed from the Wigner $3jm$ symbols using the code of Schulten & Gordon [148] written in Fortran 77 based on a recursive evaluation of the $3j$ coefficients. The Wigner-d functions can be computed using Fourier transforms on the rotation group SO(3). One approach developed by Risbo [149] is to expand the Wigner-d

functions into a Fourier sum and handle the transforms using a trivariate FFT. An alternative approach proposed by Kostelec & Rockmore [150] consists to use a recursive evaluation of the Wigner-d functions combined with a bivariate FFT technique. We exploit the latter through the free software C routine SOFT which calculates the Wigner-d on the rotation group SO(3) with Fourier transforms. Notice that when looping over L in Eq. (3.69), at each step we need to call eight Clebsch coefficients in addition of the Wigner-d functions computed by the formula Eq. (3.68) and Eq. (3.59). Obviously, this is computationally expensive; consequently, the computation on the fly of the Clebsch and Wigner-d functions is not recommended.

Our main motivation is to *precompute all* Clebsch and Wigner-d coefficients that will allow us to optimize the computation time. We show in this section that the bias matrix can be numerically computed in a very short time without the need of parallel computation. Due to the huge memory requirement (see, [150]) for the Wigner-d precomputation, the highest multipole probed in this thesis is limited to $l_{max} = 500$. In addition, we know that the bias matrix is not far from diagonal. As a result, we can restrain the computation of the bias matrix to a diagonal band $|l - l'| \leq 20$, which sufficiently provides an accurate estimation of the systematic bias of the TE power spectrum estimation, induced by the non-circularity of the beam.

All computations have been carried out using a 2.53 GHz Intel Core i5 processor laptop with 4 GB of RAM. First, we precompute the coefficient $c(l, l', L)$ defined by Eq. (3.62). We have emphasized the necessity of the precomputation of the Clebsch coefficients, but if we look at the coefficient $C^{L0}_{l-ml'm}$ where for each l and l', L varies from $|l - l'|$ to $l + l'$ and m varies from 1 to $min(l,\ l')$, we realize that this cannot be achieved due to the enormous memory storage requirement and is prohibitive even using high performance computing. Alternatively, we can reduce the memory storage by precomputing the sum $\sum_{m=-l}^{l} C^{L0}_{l-ml'm}$ and calculating the coefficients $C^{L0}_{l-ml'm}$ on the fly. We report in Fig. 3.2 the computation time of the sum $\sum_{m=-l}^{l} C^{L0}_{l-ml'm}$ as a function of the multipole. The straight line $\log_{10}(\text{time}) = 3.8\log_{10}(\text{l}) - 7.13$ represents the best fit of the recorded data points. Clearly, the computation time (in minutes) scales as $O(l^{3.8})$ and by extrapolating to higher l's we find that for the *Planck*-like high resolution experiment the time needed for the precomputation of the summation $\sum_{m=-l}^{l} C^{L0}_{l-ml'm}$ corresponding to $l_{max} = 3000$ is $\sim 10^6$ minutes. This can be carried out in a reasonable time with the current high performance computing facilities. Assuming that we use 1000 dual core processors working at the specified frequency of ~ 2.5 GHz, the precomputation of the sum up to $l = 3000$ will take about 10 hours.

We show in Fig. 3.3 the computation time of each Clebsch coefficient which roughly scales as $O(l^{2.6})$. The extrapolation of the best fit to $l = 3000$ gives an estimate of 12 hours for the precomputation of each Clebsch-Gordan coefficient (1 CPU). Practically, this can be achieved just in a few minutes using computer clusters.

Following the same procedure, we precompute all Wigner-d functions of the form $d^{L}_{0M}(\frac{\pi}{2})$ where

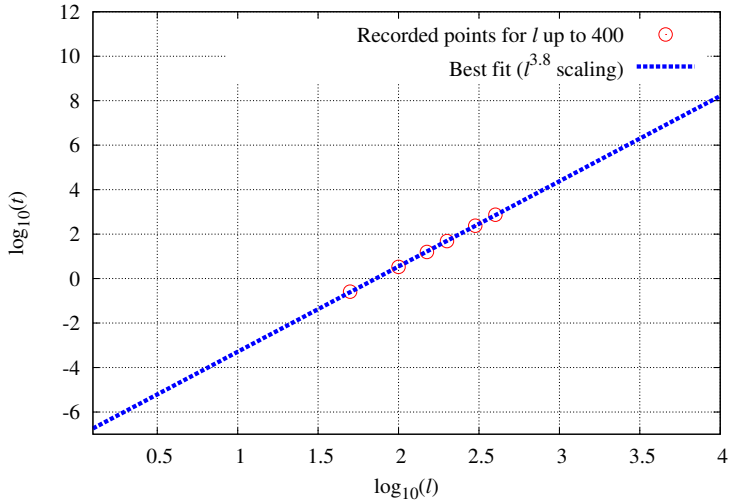

Figure 3.2: The figure illustrates the plot of the logarithm of the computation time t of the sum $\sum_{m=-l}^{l} C^{L0}_{l-ml'm}$ in minutes as a function of the logarithm of the multipole l. The red circled data points are the measured computation time with $l_{max} = 400$. The blue dashed line is the best fit to the points. We can see a tight correlation between $\log_{10}(\text{computation time})$ and $\log_{10}(\text{l})$. The linear correlation allows us to extrapolate the computation time for large multipoles. The figure indicates a computational cost of $\sim O(l^{3.8})$.

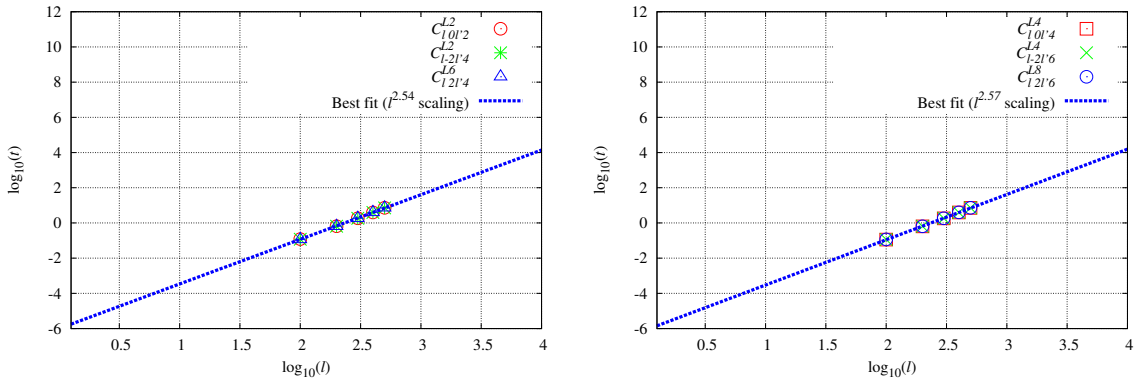

Figure 3.3: The two panels show the computation time (in minutes) of the Clebsch-Gordan coefficients involved in the calculation of the bias matrix. The blue dashed lines in both panels are the best fit of the data points for $l_{max} = 500$. Each Clebsch coefficients has approximately the same computation time and scales as $O(l^{2.6})$.

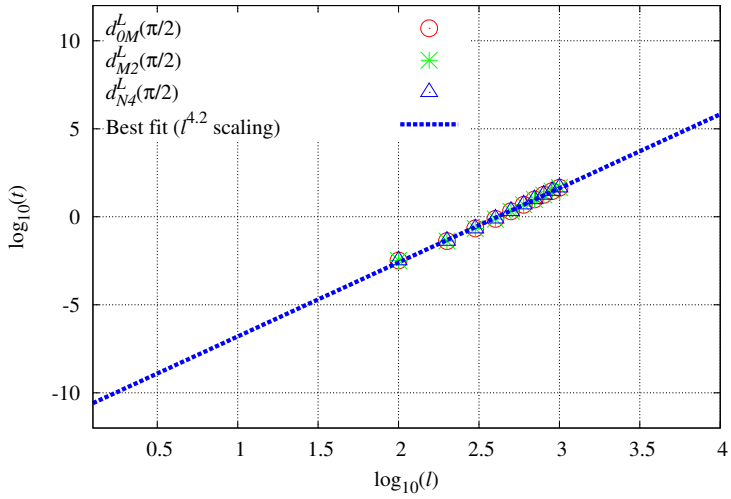

Figure 3.4: The figure illustrates the computation time (in minutes) of the Wigner-d functions for data points recorded up to $l = 1000$. The blue dashed line with $O(l^{4.2})$ scaling represents the best fit to the data points. The slope of the best fit line is relatively much steeper implying that the computation of the Wigner-d function takes much longer time as the multipole l increases.

$1 \leq M \leq L$ and $|l-l'| \leq L \leq l+l'$. The results are shown in Fig. 3.4 where the computational cost is $\sim O(l^{4.2})$. A naive estimate of the computation time deduced from the best fit extrapolated to $l = 3000$ gives ∼3 days for each Wigner-d. We conclude that at sufficiently large multipoles (small scales) the Wigner-d functions dictate the computational complexity of the calculation of the bias matrix. As the Wigner-d and Clebsch-Gordan coefficients values will never change, we just need to precompute them, all at once using clusters and store the coefficients in the computer disk.

The next step of the numerical implementation is to precompute the product of the Clebsch coefficients with the terms $dm'(L)$ (m=2, 4, 6, 8) introduced in the expression of the bias matrix Eq. (3.69) via Eq. (3.68). We define and precompute the new quantities

$$cd2(l,l',L) = C^{L2}_{l0l'2} d2(L), \tag{3.70}$$

$$cd4(l,l',L) = C^{L4}_{l0l'4} d4(L), \tag{3.71}$$

$$cd6(l,l',L) = C^{L2}_{l-2l'4} d2(L) + C^{L6}_{l2l'4} d6(L), \tag{3.72}$$

$$cd8(l,l',L) = C^{L4}_{l-2l'6} d4(L) + C^{L8}_{l2l'6} d8(L), \tag{3.73}$$

for each $2 \leq l \leq l_{max} = 500$, $|l-l'| \leq 20$, $|l-l'| \leq L \leq l+l'$. We store the new coefficients in split files where each file has 63 MB of size. There are in total 11 output files as we have constrained l and l' to a bandwidth of 20 for $l_{max} = 500$. The computation time is shown in Table 3.1. We again, rearrange the expression of the bias matrix of Eq. (3.69) in the following form which is ready for

Table 3.1: Estimate of the total computation time (in minutes) required for the precomputation of all new coefficients introduced in the calculation of the bias matrix where $l_{max} = 500$.

Coefficients	Computation time (min)
cd2	5.05
cd4	6.60
cd6	3.05
cd8	4.58
cd2c	5.04
cd4c	4.56
cd6c	4.55
cd8c	4.60
Σ_2	1.33
Σ_4	1.33
Σ_6	1.33
Σ_8	1.33

further precomputation

$$\begin{aligned} A^{TE}_{ll'} &= e^{-l^2\sigma^2}\ \delta_{ll'} \\ &+ \frac{4\pi}{2l+1}\sum_{L=|l-l'|}^{l+l'}\Big[b^T_{l'2}b^E_{l'2}\ cd2(l,l',L)c(l,l',L) + b^T_{l'4}b^E_{l'2}\ cd4(l,l',L)c(l,l',L) \\ &+ \frac{1}{2}b^T_{l'0}b^E_{l'4}\ cd6(l,l',L)c(l,l',L) + \frac{1}{2}b^T_{l'0}b^E_{l'6}\ cd8(l,l',L)c(l,l',L)\Big]. \end{aligned} \tag{3.74}$$

We proceed as previously and precompute the coefficients defined by

$$cdm'c(l,l',L) = cdm'(l,l',L)c(l,l',L), \tag{3.75}$$

where $m' = 2,\ 4,\ 6,\ 8$. We report the computation time of the coefficients in Table 3.1. We plug in Eq. (3.74) the new coefficients and write the formula in the following form

$$\begin{aligned} A^{TE}_{ll'} &= e^{-l^2\sigma^2}\ \delta_{ll'} \\ &+ \frac{4\pi}{2l+1}\left[b^T_{l'2}b^E_{l'2}\sum_{L=|l-l'|}^{l+l'} cd2c(l,l',L) + b^T_{l'4}b^E_{l'2}\sum_{L=|l-l'|}^{l+l'} cd4c(l,l',L)\right. \\ &+ \left.\frac{1}{2}b^T_{l'0}b^E_{l'4}\sum_{L=|l-l'|}^{l+l'} cd6c(l,l',L) + \frac{1}{2}b^T_{l'0}b^E_{l'6}\sum_{L=|l-l'|}^{l+l'} cd8c(l,l',L)\right]. \end{aligned} \tag{3.76}$$

The final step of the algorithm implementation consists to precompute the summations defined by

$$\Sigma_2(l,l') = \sum_{L=|l-l'|}^{l+l'} cd2c(l,l',L), \tag{3.77}$$

$$\Sigma_4(l,l') = \sum_{L=|l-l'|}^{l+l'} cd4c(l,l',L), \tag{3.78}$$

$$\Sigma_6(l,l') = \sum_{L=|l-l'|}^{l+l'} cd6c(l,l',L), \tag{3.79}$$

$$\Sigma_8(l,l') = \sum_{L=|l-l'|}^{l+l'} cd8c(l,l',L), \tag{3.80}$$

which only depend on l and l'. We resume on Table 3.1 the computation time of the different coefficients that we have included in the bias matrix. Then the final form of the bias matrix reads

$$\begin{aligned} A^{TE}_{ll'} &= e^{-l^2\sigma^2}\ \delta_{ll'} \\ &+ \frac{4\pi}{2l+1}\left[b^T_{l'2}b^E_{l'2}\ \Sigma_2(l,l') + b^T_{l'4}b^E_{l'2}\ \Sigma_4(l,l')\right. \\ &+ \left.\frac{1}{2}b^T_{l'0}b^E_{l'4}\ \Sigma_6(l,l') + \frac{1}{2}b^T_{l'0}b^E_{l'6}\ \Sigma_8(l,l')\right]. \end{aligned} \tag{3.81}$$

From Eq. (3.81) we can estimate the power spectrum using the relation defined in Eq. (3.26) and investigate how the beam asymmetry affects the cross-power spectrum TE. As all coefficients have been precomputed, provided the beam width and eccentricity, only the beam harmonic transforms need to be computed using the specific model of beam.

The final computational cost of the bias matrix evaluation is illustrated in Fig. 3.5. We have already noticed that $\log_{10}$(computation time) varies linearly with $\log_{10}(l)$. Therefore, we can fit the data points recorded from the runs with a linear function. The equation of the best fit is given by $\log_{10}(\text{time}) = 1.03\log_{10}(\text{l}) - 2.88$. After extrapolation to $l = 3000$, we find that the bias matrix can be computed in just 5 seconds. We find that the computational gain of the method scales as $O(l^{6.0}_{max})/O(l^{4.2}_{max}) = O(l^{1.8}_{max})$.

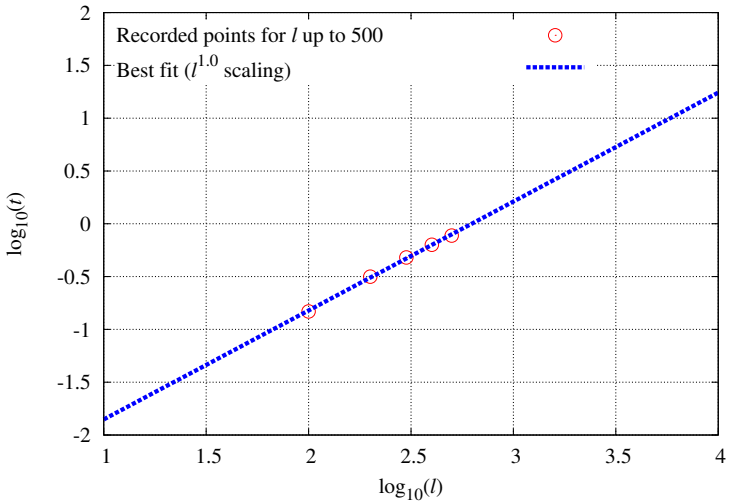

Figure 3.5: Estimate of the computation time (in seconds) of the bias matrix as a function of the logarithm of the multipole. The blue dashed line represents the best fit to the red circled data points recorded at $l = 100,\ 200,\ 300,\ 400,\ 500$. The total amount of computation time is considerably reduced and scales as $O(l)$. Note that the computation time is in a unit of seconds.

3.6 Non-circular beam investigations

In this section we present a detailed analysis of the beam systematics using realistic beam parameters from the *WMAP* and *Planck* experiments. Nevertheless, we must emphasize that the beam model considered in this work cannot completely handle the complex beam shape of the CMB experiment like *Planck*, when the beam ellipticity and orientation vary across the sky map. Despite this restriction, the result obtained in Eq. (3.81) is still applicable without discrepancy if the histogram of the effective beam ellipticity is sufficiently narrow, as it seems to be the case for *Planck* 30 GHz simulated effective beams (see, [19]).

We have reviewed that any deviation of the beam from circularity biases the estimation of the power spectrum which becomes especially significant at small angular scales. As the multipole l increases we expect more off-diagonal elements in the bias matrix which arise from the non-circularity of the beam. The following section deals with the systematic bias produced by the beam asymmetry.

3.6.1 Effects of the beam non-circularity on the bias matrix

The bias matrix encodes the power mixing between multipoles which is illustrated in Fig. 3.6 for the *WMAP* experiment in Q1 band at the frequency 40.9 GHz [6]. As inferred from both panels, the beam asymmetry bias dominates at $l\sigma \sim 1$. The coupling of power between multipoles caused by the non-circularity of the beam is evident but the effect decreases when we move further away from the diagonal elements of the bias matrix. The bias is effectively pronounced for highly elliptical

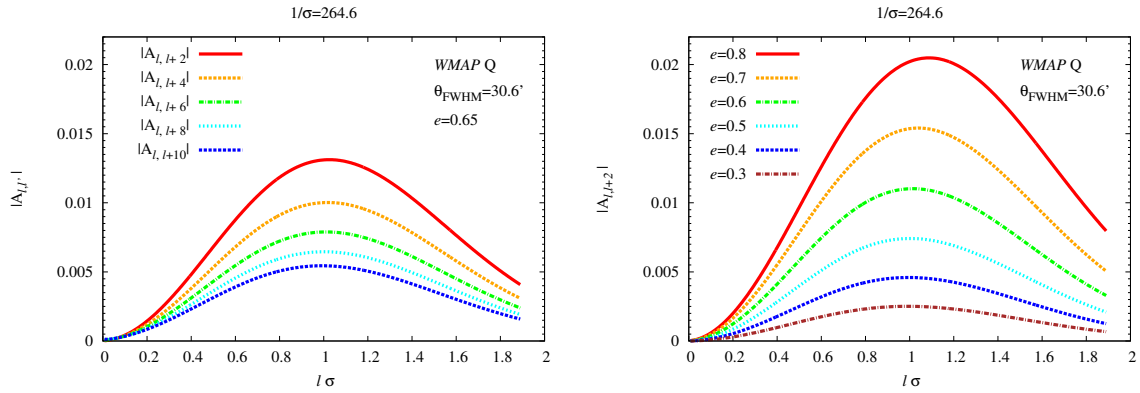

Figure 3.6: Plots of the modulus of the bias matrix as a function of the multipole l, for different values of $l'-l = 2,\ 4,\ 6,\ 8,\ 10$. The left panel illustrates the coupling between multipoles arising from the non-circularity of the beam. The mixing of power between multipoles kicks in at $l\sigma \sim 1$ but decreases when we move away from the diagonal. We show in the right panel the effect of the beam eccentricities for a given beam size $\theta_{\rm FWHM} = 30.6'$ at $l' = l + 2$. The bias increases rapidly with the beam ellipticity (eccentricity) whereas the peaks of the bias are shifted to higher l's. The elements of the bias matrix are shown for a model of beam corresponding to the *WMAP*-Q1 band with the mean beamwidth $\sigma = 3.78 \times 10^{-3}$.

beams.

In new generation CMB high resolution experiments the beam systematics can significantly affect the estimation of the power spectrum. We particularly consider the *Planck* instrument beam response that can be simulated with the beam model defined in Eq. (3.24). As we have previously claimed, this approximation is only valid to first order if the effective beam ellipticity remains constant across the sky map.

The *Planck* survey is carried out with the Low Frequency Instrument (LFI) [151], and the High Frequency Instrument (HFI) [152]. The broad frequency range of *Planck* allows to cover the peaks of the CMB power spectrum and characterizes the spectra of foreground emissions [153]. The *Planck* polarized detectors at 30 GHz exhibit the highest beam asymmetry with an ellipticity which spans over the range $1.35 - 1.40$ [19]. Therefore, we expect an important beam corrections at this channel. At 30 GHz the beam mean ellipticity is $\epsilon = 1.36$ (e= 0.68) with a mean beam width $\theta_{\rm FWHM} = 32.7'$ [153]. We report in Fig. 3.7 the bias matrix obtained from the simulated beams. The plot of the bias matrix against the multipoles exhibits similar behaviour as Fig. 3.6 demonstrating the importance of the power mixing between multipoles in polarization experiments with asymmetric beam.

In order to illustrate the effects of the beam non-circularity in multipole space we consider a sufficiently high resolution beam $\theta_{\rm FWHM} = 2^\circ$ with a mean beam width $\sigma = 1.48 \times 10^{-2}$. We report in Fig. 3.8 the corresponding plot of the logarithm of the modulus of the bias matrix. We can see that the off-diagonal elements of the bias matrix arising from the non-circularity of the beam

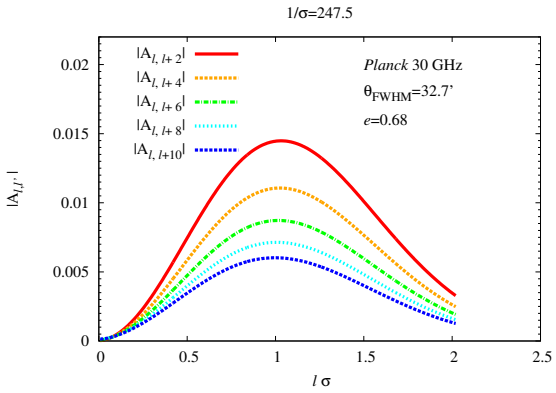

Figure 3.7: The modulus of the bias matrix plotted as a function of the multipole l, for different values of $l' - l = 2,\ 4,\ 6,\ 8,\ 10$. The coupling between multipoles arising from the beam asymmetry kicks in at $l\sigma \sim 1$ but falls off when we move away from the diagonal. The elements of the bias matrix are shown for a model of beam corresponding to the *Planck* 30 GHz with the mean beamwidth $\sigma = 4.04 \times 10^{-3}$ and mean ellipticity $\epsilon = 1.36$ ($e = 0.68$).

start to dominate at the multipole where the bias peaks ($l\sigma \sim 1$). The off-diagonal elements which dominate at $l\sigma \gtrsim 1$ can be clearly distinguished in Fig. 3.9 where we plot the bias matrix for an ideal experiment with non-rotating beam ($\theta_{\rm FWHM} = 1^\circ$ and e= 0.6).

We have seen that the *Planck* 30 GHz beam response pattern is the most asymmetric (e= 0.68) among the *Planck* beams. As an illustration we plot the corresponding bias in the multipole space which is shown in Fig. 3.10. Obviously, the coupling between multipoles (off-diagonal elements of the bias) is important for $l\sigma \gtrsim 1$ implying the necessity of appropriate corrections of the systematics.

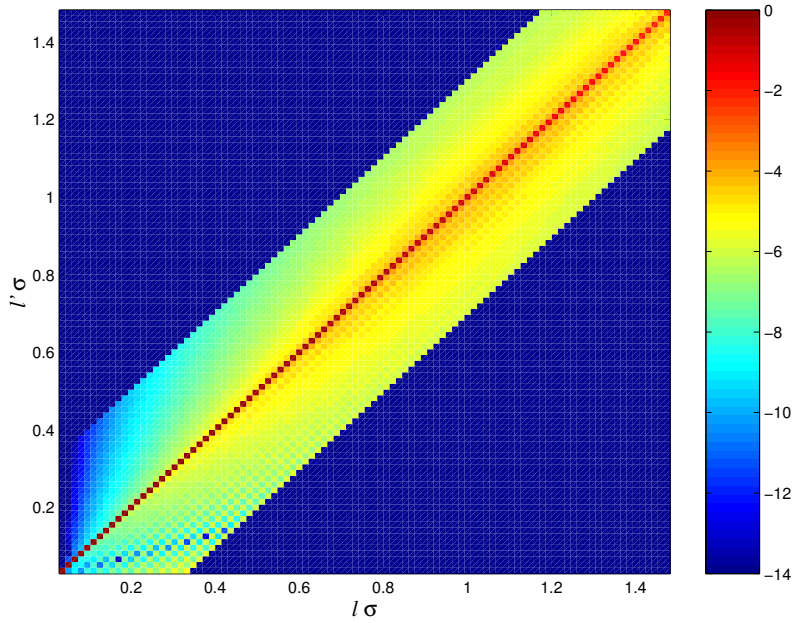

Figure 3.8: Plot of $\log \mid A_{ll'} \mid$ in regions of the multipole space for an hypothetical experiment under a non-rotating beam assumption with a beam resolution $\theta_{\mathrm{FWHM}} = 2^{\circ}$ (average beam size $\sigma = 1.48 \times 10^{-2}$) and eccentricity $e = 0.6$. Significant off-diagonal elements can be seen at $l\sigma \sim 1$ and the effects become more important as l increases. The plot of the logarithm of the bias matrix modulus is shown within the mutipoles band width $\mid l - l' \mid$=20.

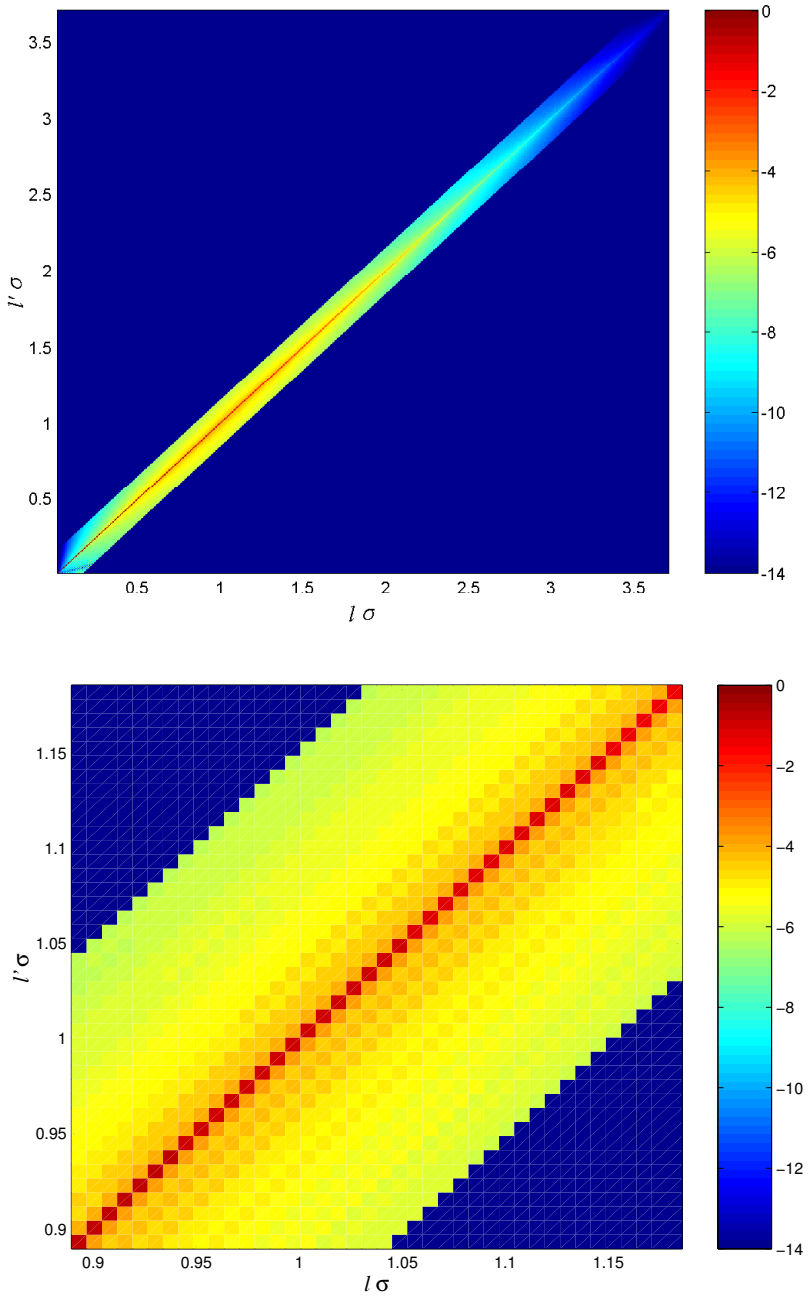

Figure 3.9: Plots of $\log \mid A_{ll'} \mid$ in the multipole space for a hypothetical experiment with non-rotating beam and a beam resolution $\theta_{\rm FWHM} = 1^\circ$ ($\sigma = 7.41 \times 10^{-3}$) with an eccentricity $e = 0.6$. The top panel illustrates the plot between the multipole range [2, 500] and the bottom panel shows the same plot in the range [120, 140]. Both panels show important off-diagonal elements that kick in for $l\sigma \sim 1$.

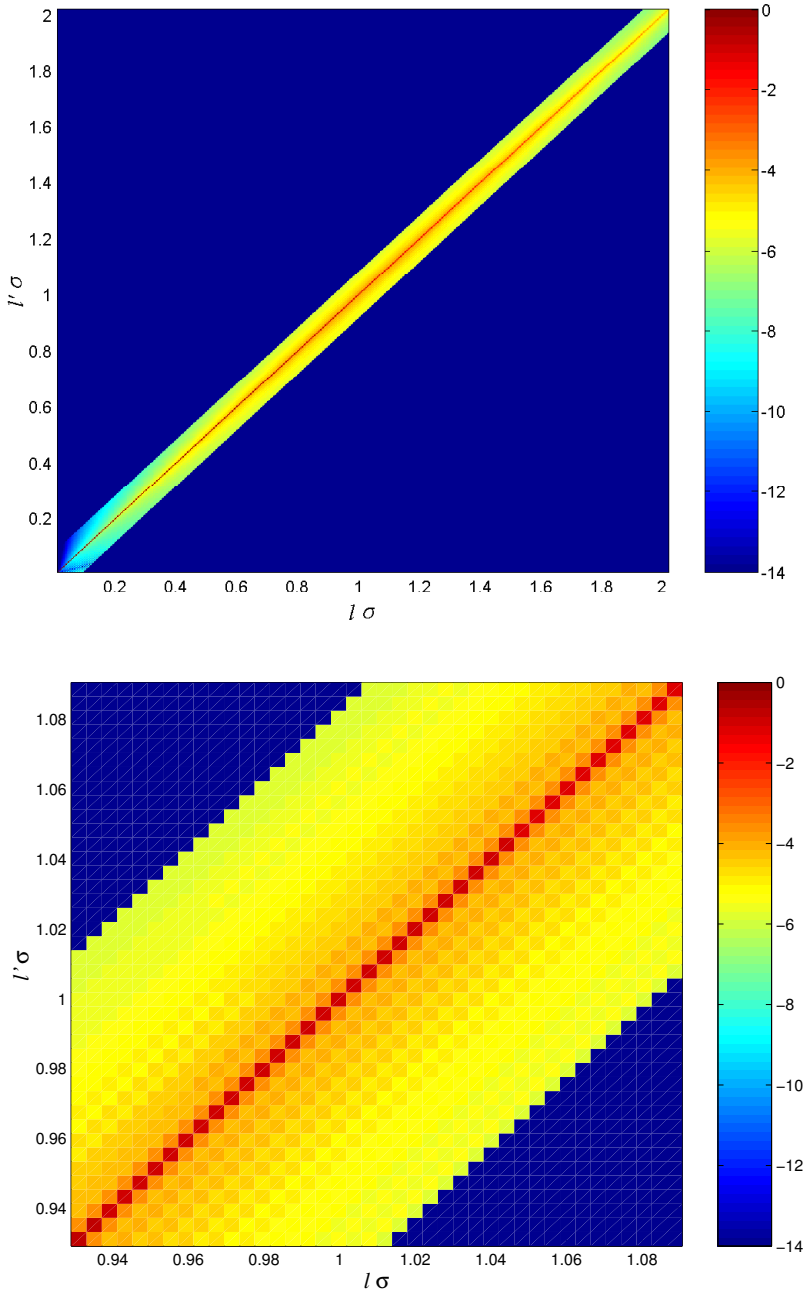

Figure 3.10: Plots of $\log \mid A_{ll'} \mid$ in the multipole space for *Planck* experiment simulated beam parameters at 30 GHz with a beam resolution $\theta_{\rm FWHM} = 32.7'$ ($\sigma = 4.04 \times 10^{-3}$) and eccentricity $e = 0.68$. The top panel illustrates the plot of the bias matrix between the multipole range [2, 500] and the bottom panel shows the same plot in the range [230, 270]. Both panels show significant mixing of power (off-diagonal elements) between multipoles for $l\sigma \sim 1$ that arises from the beam ellipticity.

3.6.2 Effects of the beam non-circularity on the TE power spectrum estimation

In the following, we focus our analysis on the effect of the beam asymmetry on the power spectrum estimation and evaluate the systematic bias. For this purpose, we compare the observed power spectrum of an elliptical beam with a given resolution $\theta_{\rm FWHM}$ and eccentricity e to the corresponding power spectrum measured using a circular Gaussian beam with the same size $\theta_{\rm FWHM}$. The observed power spectrum $\langle \tilde{C}_l^{TE} \rangle$ can be obtained by convolving the true power spectrum C_l^{TE} with an elliptical window through Eq. (3.26). We compute the true power spectrum using the CAMB [154] software for a set of cosmological parameters derived from the *WMAP*7 and the *Planck* best fit fiducial model. The recovered power spectrum from the *WMAP*7 best fit is illustrated in Fig. 3.11. For a given beam size, we find that the peak of the power spectrum is increasing with the beam eccentricity (ellipticity) and is shifted to higher l's.

Similar shifts are observed for the *Planck*+ *WP*+ highL [155] best fit model which are reported in Fig. 3.12 for the *Planck* channels with the highest beam asymmetry (e= 0.68 at LFI 30 GHz) and the smallest beam asymmetry (e= 0.30 at HFI 143 GHz). From both panels of Fig. 3.11 and Fig. 3.12, we notice that for a given beam eccentricity the peaks amplitude of the power spectrum increases as the beam size becomes much smaller.

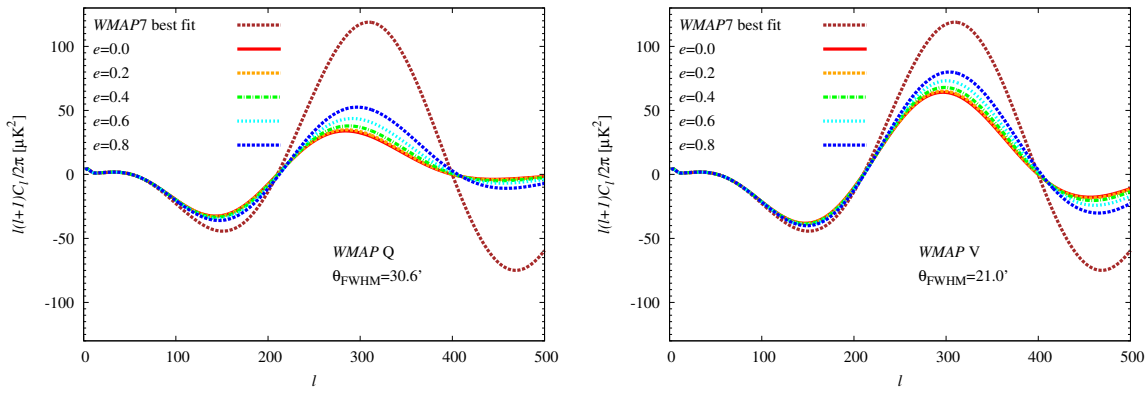

Figure 3.11: Recovered power spectrum using the *WMAP*7 ΛCDM best fit model. The effect of the non-circularity is shown for the *WMAP*-Q1 band experimental beam parameter with size $\theta_{\rm FWHM} = 30.6'$ and eccentricity $e = 0.65$ (left panel) and the *WMAP* V band with size $\theta_{\rm FWHM} = 21.0'$ and eccentricity $e = 0.46$ (right panel). The red curve is the power spectrum computed from a circular Gaussian window. The *WMAP* best fit model is shown in brown dotted curve.

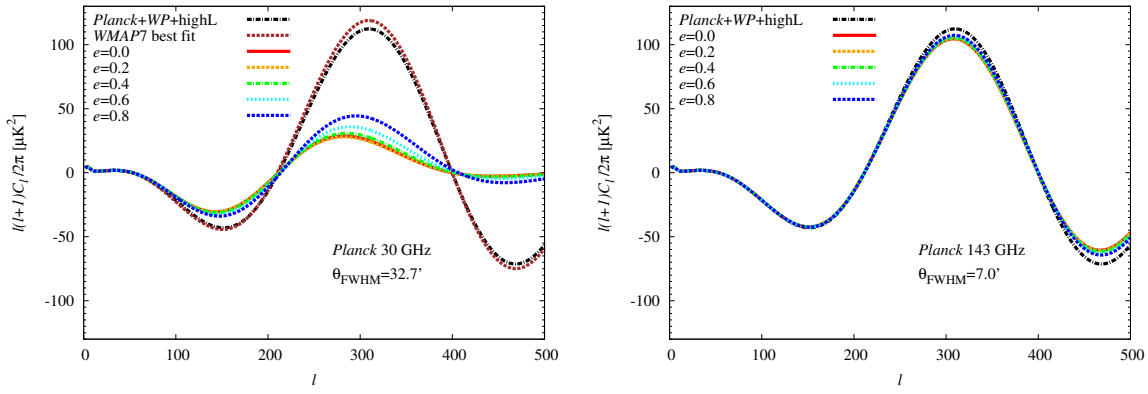

Figure 3.12: Recovered power spectrum using the *Planck* ΛCDM best fit model (*Planck*+ *WP*+ highL in black dotted curve). For comparison, the *WMAP*7 best fit model is also shown in the left panel (brown dotted curve). The effect of the beam non-circularity is shown for the *Planck* 30 GHz beam parameter with size $\theta_{\rm FWHM} = 32.7'$ and eccentricity $e = 0.68$ (highest ellipticity $\epsilon = 1.36$) (left panel) and the *Planck* 143 GHz beam with size $\theta_{\rm FWHM} = 7.0'$ and eccentricity $e = 0.30$ (smallest ellipticity $\epsilon = 1.05$) (right panel).

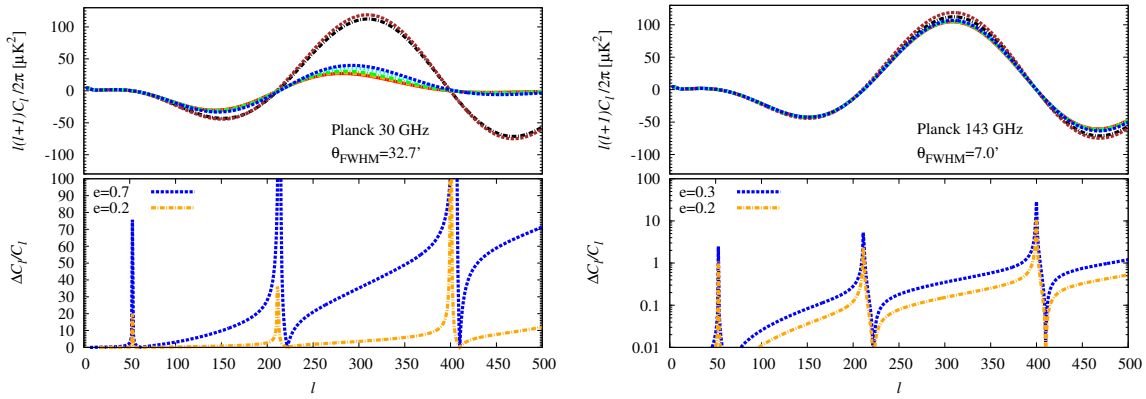

Figure 3.13: Recovered power spectrum using the *Planck* ΛCDM best fit model and the corresponding bias $\Delta C_l/C_l$ as a function of the multipole l. The systematic bias due to the non-circularity of the beam is shown for the *Planck* beam $\theta_{\rm FWHM} = 32.7'$ and eccentricity $e = 0.68 \sim 0.7$ at 30 GHz (left panel) and the *Planck* beam $\theta_{\rm FWHM} = 7.0'$ and eccentricity $e = 0.3$ at 143 GHz (right panel). Hypothetical experiments with respectively the same beam size $\theta_{\rm FWHM} = 32.7'$ and $\theta_{\rm FWHM} = 7.0'$ but with mildly circular beam ($e = 0.2$) are shown for comparison. The bias estimates strongly depend on the beam eccentricity and are more significant at small angular scales.

The systematic bias in the power spectrum estimation is reported in Fig. 3.13. For clarity, we only plotted the systematic bias for the eccentricity $e = 0.2$, $e = 0.3$ (*Planck* smallest asymmetric beam) and $e = 0.7$ (*Planck* highest asymmetric beam). The plots show that the bias estimates are significant at large l's. For the least asymmetric beam (143 GHz) the bias estimate is $\sim 1\%$ at $l_{max} = 500$. For the *Planck* 30 GHz, the systematic bias can be quite large. However, the bias estimates computed here are in reality an upper limit of the systematics since we expect that the effective eccentricity of the beam in the time stream is reduced, as during observations the beam revisits each sky pixel with different orientations so that some non-circular modes cancel out.

Notice that in Fig. 3.11 - 3.13 the best fit model spectra *WMAP*7 and *Planck*+ *WP*+ highL do not have the beam convolution included. We have only shown them in the recovered power spectra in order to illustrate from which best fit model the beam convolution was obtained. In Fig. 3.12 (left panel), the observed power spectrum is the convolution of the beam with the *Planck*+ *WP*+ highL best fit. In that same figure is shown the *WMAP*7 best fit just for comparison with the recent *Planck*+ *WP*+ highL best fit obtained by *Planck* Collaboration 2013 [155].

Now, we estimate the power spectrum bias for different eccentricities computed at the multipole where the bias peaks ($l_{peak}\sigma \sim 1$) for the *Planck* angular beam size $\theta_{\rm FWHM} = 32.7'$ (30 GHz), $\theta_{\rm FWHM} = 27.0'$ (44 GHz) and *WMAP* V beam size $\theta_{\rm FWHM} = 21.0'$. The results are reported in Fig. 3.14. We find an evidence of strong correlation between the systematic bias and the eccentricity of the beam computed at l_{peak}. The recorded data points can be very well fitted with quadratic polynomials which allow the determination of the bias at l_{peak} up to the smallest angular resolution probed by *Planck* ($\theta_{\rm FWHM} = 4.3'$ at HFI 857 GHz). The plots clearly show that for a polarimetry

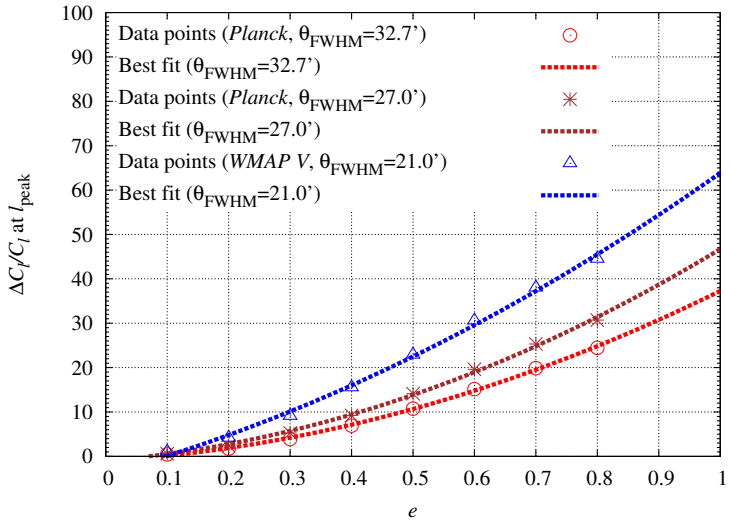

Figure 3.14: Systematic bias $\Delta C_l/C_l$ computed at $l_{\rm peak} = 1/\sigma$ for different beam eccentricities e. The dashed lines are the best fit to the data points recorded for the *Planck* beam size $\theta_{\rm FWHM} = 32.7'$ at 30 GHz, and $\theta_{\rm FWHM} = 27.0'$ at 44 GHz. The *WMAP* V channel beam width $\theta_{\rm FWHM} = 21.0'$ is shown as well in order to illustrate the effect of the beam size. The data points can be well fitted with a second order polynomial of the eccentricity. As inferred from the plots, the beam systematics increase with the ellipticity (eccentricity) of the asymmetric beam; and given the ellipticity of the beam, the bias of the power spectrum estimation become more significant for smaller beam width.

experiment, the power spectrum bias estimates at l_{peak} increase with the beam ellipticity and for a given beam eccentricity (ellipticity) the bias becomes more significant for smaller beam size.

3.7 Discussion

In CMB experiments the bias matrix relates the observed power spectrum to its true value. Among the systematic biases affecting the estimation of the power spectrum, the beam non-circularity (asymmetry) is one of the major potential source of systematics that cannot be neglected in *Planck*-like high sensitivity and resolution experiment. More importantly for the polarized signal (at a level about tenth of the temperature fluctuation), the beam systematics must be correctly addressed and accounted for. We have presented a semi-analytical framework to compute the bias matrix of the TE power spectrum including the beam asymmetry in which the non-circular beam shape was modeled using a perturbative expansion of the beam around a circular Gaussian beam (see, [66]).

We have developed a computationally fast algorithm that can be implemented in simulation pipeline analysis although the formalism described in this chapter is only valid for a non-rotating beam, assuming that the ellipticity of the effective beam does not vary across the pixels map. Nevertheless our approach provides some insights about the computational cost involved in more realistic scanning strategies. We have reduced the analytical expression of the bias matrix to its

simplest form by precomputing all Clebsch-Gordan coefficients and Wigner-d functions. The computation ressource requirement is very modest and can be carried out with a laptop processor up to the multipole $l_{max} = 500$ with a computational scaling of $O(l_{max})$ (1 CPU at 2.53 GHz and 4 GB of RAM). We recall that the computational cost of the FEBeCoP implemented in *Planck* (though, using real scan path) by Mitra et al. [19] scales as $N_{pix}N_{beam}$.

The computation of the Wigner-d functions is a memory intensive task and Kostelec & Rockmore [150] have claimed that the 3-term recurrence relations have been verified stable up to the bandwidth $B = 1024$. As a result of these limitations it was not possible to compute the functions of the form $d^L_{0M}(\frac{\pi}{2})$ or $d^L_{Mm''}(\frac{\pi}{2})$ when the index L reaches the bandwidth 1024 ($L < B$ i.e., $L_{max} = 1023$). In such case, using our laptop 4 GB of RAM, the code of Kostelec & Rockmore produces NAN and infinity numbers. As L varies from $|l - l'|$ to $l + l'$ and we compute inside the diagonal band $|l - l'| \leq 20$, it results in the limitation of the probed multipole to $l_{max} = 500$, as in that case $l + l' = L_{max} = 500 + 520 = 1020$. Obviously a multipole value of $l_{max} = 501$ is still possible but such difference does not have much significance for the $WMAP$ or *Planck* analyses.

Our approach can be extended to higher multipoles up to $l_{max} = 3000$ at the expense of disc/memory storage and code input/output (I/O) overhead. This can be done in the future provided that all Wigner-d functions can be precomputed up to $l_{max} = 3000$. The bias matrix computation was restricted in the band $\mid l - l' \mid \leq 20$ in order to reach the highest multipole $l_{max} = 500$. This band width choice can be well justified as in most CMB experiments the beam profile is mildly elliptical ($\epsilon \leq 1.2$, [66]) implying that the bias matrix is not far from diagonal. For highly asymmetric beams, a much broader band (e.g $\mid l - l' \mid \leq 50$) is desirable in order to correctly evaluate the bias estimates of the power spectrum with high precision.

A second order expansion in the ellipticity parameter introduced in the beam harmonic transform is accounted for highly elliptical beam (e.g., *Planck* 30 GHz where $\epsilon = 1.36$), and two non-circular corrections with modes $m = 2,\ 4$ (for the temperature) and $m = 4,\ 6$ (for the E-mode polarization) are included to adequately describe the beam geometry (see, [66]). From the extrapolation of the recorded runs, we find that the bias matrix can be computed up to $l_{max} = 3000$ in a few seconds and the corresponding computational gain is $\sim O(l^{1.8})$. Theoretically this is a naive estimate of the computation time at large multipoles as the program I/O overhead marginally increases the computation time.

Our findings suggest that the systematic biases peak at a multipole comparable to the inverse of the beam width. The amplitude of the peaks of the bias increases with the ellipticity and is more significant at higher multipoles. Similar behaviour has been already observed for the temperature correlation (see, [130]). A graphic representation of the bias matrix in multipole space shows the importance of multipoles coupling at $l\sigma \gtrsim 1$ which arises from the beam asymmetry but the mixing of power between multipoles falls off when we move away from the bias matrix diagonal.

We find that the effect of the non-circularity of the beam in the TE power spectrum systematic bias at $l_{peak} \sim 1/\sigma$ is important attaining $\sim 20\%$ ($\epsilon_{\rm mean} = 1.36$ at 30 GHz) in the *Planck* highest asymmetric beams. In *WMAP* Q band (effective ellipticity $\epsilon = 1.15$ with beam width $\theta_{\rm FWHM} = 30.6'$), the power spectrum bias estimate is $\sim 12\%$ and in *WMAP* V (effective ellipticity $\epsilon = 1.09$ and beam width $\theta_{\rm FWHM} = 21'$), the corresponding systematic bias is $\sim 16\%$.

For *Planck* and *WMAP* beams with much smaller size the bias peaks outside the range [2, 500] but we expect much significant bias for such high resolution beams. We note that the biases previously estimated in the simulated *Planck* beams represent upper limits. This is explained by the fact that the ellipticity (eccentricity) of the beam in our time domain representation of the elliptical window is slightly larger than the effective beam ellipticity (eccentricity) in the pixel domain since in the latter, during the satellite observations the beams visit each sky pixel multiple times, but with different orientations of the beams resulting to some extent in the suppression of non-circular modes. Consequently, the effective beam ellipticity (eccentricity) in the sky map becomes much smaller than our nominal ellipticity (eccentricity) in the time stream.

General scanning strategies must be incorporated in our analysis in the future in order to improve the accuracy of the bias estimates of the TE power spectrum. Simultaneously, the variations of the beam ellipticity along the scan path must be correctly accounted for. The systematics of instrument noise and non-uniform/cut-sky using asymmetric beams are expected to become important as well in CMB polarization experiments. In Chapter 4, we will extend this work in the case of non-circular beams with incomplete sky coverage resulting from the Galactic foreground emissions and point sources masking.

The main purpose of the non-circular beam smoothing was to assess the effect of the beam asymmetry on the TE power spectrum estimation by convolving the beam with a fiducial model of a spectrum computed with the CAMB software for a given cosmology. Afterwards, the non-circular and circularly symmetric beam convolutions are compared to estimate the systematic bias. This investigation allows us to depict the importance of the beam asymmetry for high resolution polarization experiments. Nevertheless, our work has been restricted to the ideal case of noiseless experiments and full sky survey. At the time of the writing of this thesis, the *Planck* experiment polarization data analysis has been under process and no polarization data was available. In practical applications, a careful consideration of all systematic effects must be carried out in order to obtain an unbiased estimation of the power spectrum. In this study, we have not applied our results to the existing $WMAP$ polarization data which are polluted by too much noise, as we find it unreasonable to derive cosmological parameters from such poor quality polarization data. However, for the forthcoming *Planck* data, we plan to complete this optics by deconvolving the *Planck* data with the asymmetric beam and including the cut-sky systematic effect as well. In such way we can retrieve the true power spectrum and derive the corresponding sets of cosmological parameters.

Then the comparison of the latter results with the current high resolution $WMAP$ and $Planck$ experiments best fit fiducial model enable us to quantify the change in cosmological parameters due to the beam asymmetry.

We resume that the fast pipeline implementation that we have developed in this work, provides a very convenient tool in the understandings of the beam systematics corrections of the TE power spectrum, in particular at large angular scales where many CMB anomalies have been previously observed by the high resolution $WMAP$ and $Planck$ experiments (e.g., see, $Planck$ collaboration [156]).

Chapter 4

Non-circular beam and cut-sky for TE polarized signals

4.1 Introduction

We have emphasized in the previous chapter the effect of the non-circularity (asymmetry) of the detectors beams on the estimation of the TE power spectrum by assuming a full sky coverage. This preliminary investigation allowed us to give some insights about the level of debiasing needed in order to correct the beam systematics. Practically, prior to the power spectrum estimation, it is necessary to remove the foreground contaminated CMB signals. This can be done by applying a mask along the Galactic plane where strong foreground emissions have been observed [157]. In this chapter, we consider the additional effect of the partial sky coverage besides the non-circularity of the beams. The polarization mask $w^P(\hat{q})$ covers larger area across the Galactic plane in comparison to the temperature mask $w^T(\hat{q})$. The smoothing of the sky map with the temperature and polarization masks in harmonic space adds an extra power to the variance of the temperature and polarization anisotropies and consequently biases the true power spectrum.

This chapter focuses on the derivation of the TE bias matrix by simultaneously considering the effect of the beam non-circularity (asymmetry) and the partial sky (cut-sky) coverage. The approach is similar to the non-circular beam case, though the presence of mask complicates the TE bias matrix calculation.

4.2 Sky multipole coefficients

We follow the same approach which has been developed in Chapter 3 for the calculation of the multipole coefficients of the harmonics expansion of the temperature fluctuation anisotropies and the E-mode polarization, though, we need to include in the process the CMB map masking weighted

by the mask functions (temperature and polarization) in order to suppress the foreground residuals. From the expansion of the sky true temperature anisotropy $\Delta T(\hat{q})$ in spherical harmonic basis

$$\Delta T(\hat{q}) = \sum_{lm} a_{lm}^{T} Y_{lm}(\hat{q}), \tag{4.1}$$

we can derive the sky multipoles as

$$a_{lm}^{T} = \int d\Omega_{\hat{q}} \Delta T(\hat{q}) Y_{lm}^{*}(\hat{q}), \tag{4.2}$$

where $Y_{lm}^{*}(\hat{q})$ denotes the complex conjugate of the spherical harmonic function. The integration is carried out over the solid angle $d\Omega_{\hat{q}} = \sin\theta d\theta d\phi$ in the given direction $\hat{q}$ in the spherical coordinates (θ, ϕ). We can connect the observed temperature $\widetilde{\Delta T}(\hat{q})$ to the multipole coefficients according to the relation

$$\tilde{a}_{lm}^{T} = \int d\Omega_{\hat{q}} \widetilde{\Delta T}(\hat{q}) Y_{lm}^{*}(\hat{q}). \tag{4.3}$$

The measured temperature fluctuations $\widetilde{\Delta T}(\hat{q})$ in CMB experiments is the convolution of the true temperature $\Delta T(\hat{q}')$ on the sky with the beam profile $B(\hat{q}, \hat{q}')$. Furthermore, the true temperature is contaminated by an instrumental noise $n(\hat{q})$. Now, we must eliminate the sky pixels contaminated by foregrounds by choosing an appropriate mask weight function $w(\hat{q})$ so that $w(\hat{q}) = 0$ for the corrupt pixels and $w(\hat{q}) = 1$ for the clean ones. Generally, the weight function $w(\hat{q})$ is a smooth function which can varies between zero and one. Then, the corresponding observed temperature is expressed as

$$\widetilde{\Delta T}(\hat{q}) = w^{T}(\hat{q}) \left[\int d\Omega_{\hat{q}'} B(\hat{q}, \hat{q}') \Delta T(\hat{q}') + n(\hat{q}) \right], \tag{4.4}$$

where $w^{T}(\hat{q})$ denotes the total intensity (temperature) mask. As our main purpose is to investigate the effect of the beam and cut-sky systematics, therefore, in the noiseless limit the sky multipoles can be written as

$$\tilde{a}_{lm}^{T} = \int d\Omega_{\hat{q}} w^{T}(\hat{q}) \int d\Omega_{\hat{q}'} B(\hat{q}, \hat{q}') \Delta T(\hat{q}') Y_{lm}^{*}(\hat{q}). \tag{4.5}$$

We expand the true temperature anisotropy in harmonic space as

$$\Delta T(\hat{q}') = \sum_{l'm'} a_{l'm'}^{T} Y_{l'm'}(\hat{q}'), \tag{4.6}$$

and plug in Eq. (4.5) to obtain the following expression

$$\tilde{a}^T_{lm} = \sum_{l'm'} a^T_{l'm'} \int d\Omega_{\hat{q}} w^T(\hat{q}) Y^*_{lm}(\hat{q}) \int d\Omega_{\hat{q}'} B(\hat{q}, \hat{q}') Y_{l'm'}(\hat{q}'). \tag{4.7}$$

Equivalently, we can take the complex conjugate of the sky multipoles, and from the reality condition of the beam we may write

$$\tilde{a}^{T*}_{lm} = \sum_{l'm'} a^{T*}_{l'm'} \int d\Omega_{\hat{q}} w^{T*}(\hat{q}) Y_{lm}(\hat{q}) \int d\Omega_{\hat{q}'} B(\hat{q}, \hat{q}') Y^*_{l'm'}(\hat{q}'). \tag{4.8}$$

By introducing the Wigner-D rotation matrices, we can write the integral containing the beam function $B(\hat{q}, \hat{q}')$ in the form

$$\int d\Omega_{\hat{q}'} B(\hat{q}, \hat{q}') Y^*_{l'm'}(\hat{q}') = \sum_{m''=-l'}^{l'} b^T_{l'm''} D^{l'}_{m'm''}(\hat{q}, \rho(\hat{q})), \tag{4.9}$$

where $b^T_{l'm''}$ is the temperature beam harmonic transform. Replacing Eq. (4.9) in Eq. (4.8), we get

$$\tilde{a}^{T*}_{lm} = \sum_{l'm'} a^{T*}_{l'm'} \sum_{n=-l'}^{l'} b^T_{l'n} \int d\Omega_{\hat{q}} w^{T*}(\hat{q}) Y_{lm}(\hat{q}) D^{l'}_{m'n}(\hat{q}, \rho(\hat{q})). \tag{4.10}$$

We expand in the same way the mask function as

$$w^{T*}(\hat{q}) = \sum_{l''m''} w^T_{l''m''} Y_{l''m''}(\hat{q}), \tag{4.11}$$

and substitute in Eq. (4.10) to obtain

$$\tilde{a}^{T*}_{lm} = \sum_{l'm'} \sum_{n=-l'}^{l'} \sum_{l''m''} a^{T*}_{l'm'} b^T_{l'n} w^T_{l''m''} \int d\Omega_{\hat{q}} Y_{lm}(\hat{q}) Y_{l''m''}(\hat{q}) D^{l'}_{m'n}(\hat{q}, \rho(\hat{q})). \tag{4.12}$$

The integral in Eq. (4.12) contains the product of spherical harmonic functions with the Wigner-D function. In fact, it is computationally advantageous to express these functions in term of Clebsch-Gordan coefficients, as the publicly available SLATEC Fortran subroutine DRC3JJ.f [148] allows the computation of the Clebsch-Gordan coefficients. The calculation of the term

$$I = \int d\Omega_{\hat{q}} Y_{lm}(\hat{q}) Y_{l''m''}(\hat{q}) D^{l'}_{m'n}(\hat{q}, \rho(\hat{q})) \tag{4.13}$$

involved in Eq. (4.12), is reported in Appendix D. Thus, the general form of the temperature

expansion multipoles reads

$$\tilde{a}^{T*}_{lm} = \sum_{l'm'} \sum_{n=-l'}^{l'} \sum_{l''m''} a^{T*}_{l'm'} b^{T}_{l'n} w^{T}_{l''m''} \times I. \tag{4.14}$$

The multipole expansion of the temperature defined by Eq. 4.14 combined with the E-polarization expansion that we derive in the next section, will allow the computation of the TE cross-correlation and the corresponding power spectrum.

4.3 E-polarization multipole coefficients

In order to estimate the TE power spectrum from the cross-correlation of the temperature and E-polarization in harmonic space, we need to derive the analytical expression of the E-mode multipoles. We proceed similarly to the full sky case but, obviously we have to apply a polarization mask $w^P(\hat{q})$. For CMB experiments with beams treated as non-circular, and in the presence of a cut-sky, the E-polarization multipoles take the form

$$\tilde{a}^{E}_{lm} = \frac{1}{2} \int d\Omega_{\hat{q}} w^P(\hat{q}) [(Q - iU)_{eff}(\hat{q})\ {}_2Y^*_{lm}(\hat{q}) + (Q + iU)_{eff}(\hat{q})\ {}_{-2}Y^*_{lm}(\hat{q})], \tag{4.15}$$

where the effective Stokes parameters Q_{eff} and U_{eff} of the smoothed beam are defined by [66]

$$Q_{eff} = 2 \sum_{lmM} [D^l_{mM}(\hat{q}, \rho(\hat{q}))]^*\ b^{E*}_{lM}\ a^{E}_{lm}, \tag{4.16}$$

$$U_{eff} = 2 \sum_{lmM} [D^l_{mM}(\hat{q}, \rho(\hat{q}))]^*\ b^{E*}_{lM}\ a^{B}_{lm}. \tag{4.17}$$

We substitute the effective Stokes parameters in Eq. (4.15), and obtain

$$\begin{aligned} \tilde{a}^{E}_{lm} &= \sum_{l'm'} \sum_{M=-l'}^{l'} \int d\Omega_{\hat{q}} w^P(\hat{q}) [D^{l'}_{m'M}(\hat{q}, \rho(\hat{q})) b^{E}_{l'M}]^* \\ &\times [a^{E}_{l'm'}(\ {}_2Y^*_{lm}(\hat{q}) + {}_{-2}\,Y^*_{lm}(\hat{q})) - i a^{B}_{l'm'}(\ {}_2Y^*_{lm}(\hat{q}) - {}_{-2}\,Y^*_{lm}(\hat{q}))]. \end{aligned} \tag{4.18}$$

Then, we expand in harmonic space the mask weight function $w^P(\hat{q})$ of the polarization

$$w^P(\hat{q}) = \sum_{l''m''} w^P_{l''m''} Y_{l''m''}(\hat{q}), \tag{4.19}$$

to derive the following expression of the polarization multipoles

$$\begin{aligned}\tilde{a}^{E}_{lm} &= \sum_{l'm'}\sum_{M=-l'}^{l'}\sum_{l''m''} w^{P}_{l''m''}\int d\Omega_{\hat{q}} Y_{l''m''}(\hat{q})[D^{l'}_{m'M}(\hat{q},\rho(\hat{q}))b^{E}_{l'M}]^{*} \\ &\times \; [a^{E}_{l'm'}({}_{2}Y^{*}_{lm}(\hat{q}) + {}_{-2}Y^{*}_{lm}(\hat{q})) - ia^{B}_{l'm'}({}_{2}Y^{*}_{lm}(\hat{q}) - {}_{-2}Y^{*}_{lm}(\hat{q}))]. \end{aligned} \tag{4.20}$$

We keep this final form of the E-multipoles harmonic transforms $\tilde{a}^{E}_{lm}$ which is convenient for the calculation of the multipole coefficients correlation in harmonic space. Due to the statistical isotropy of the CMB, only the real part of $\tilde{a}^{E}_{lm}$ gives non-vanishing contribution in the estimation of the power spectrum. In the next section, we derive in details the bias matrix involved in the TE power spectrum estimation corresponding to the asymmetric beam and cut-sky by using the pseudo-C_l estimator.

4.4 The bias matrix

For large data size, the pseudo-C_l method provides a rapid estimation of the power spectrum with a sufficient accuracy for high resolution maps. Prior to the estimation, we need to mask the polluted CMB signals on the Galactic plane which is a source of strong foreground emissions. From the definition of the pseudo-C_l

$$C^{TE}_{l} = \frac{1}{2l+1}\sum_{m=-l}^{l} a^{T}_{lm}a^{E*}_{lm}, \tag{4.21}$$

we can write the expectation value of the TE power spectrum as

$$\langle\tilde{C}^{TE}_{l}\rangle = \frac{1}{2l+1}\sum_{m=-l}^{l}\langle\tilde{a}^{T*}_{lm}\tilde{a}^{E}_{lm}\rangle = \sum_{l'} A^{TEcut}_{ll'}\, C^{TE}_{l'}, \tag{4.22}$$

where $A^{TEcut}_{ll'}$ denotes the bias matrix, which contains the coupling of power between multipoles due to the combined effects of the beam asymmetry and cut-sky. From Eq. (4.14) and Eq. (4.20) and using the parity conservation property $\langle a^{T*}_{l'm'}a^{B}_{l'_1m'_1}\rangle = 0$, we may write

$$\begin{aligned}\langle\tilde{C}^{TE}_{l}\rangle &= \frac{1}{2l+1}\sum_{m=-l}^{l}\sum_{l'm'}\sum_{n=-l'}^{l'}\sum_{l''m''}\sum_{l'_1m'_1}\sum_{M=-l'_1}^{l'_1}\sum_{l''_1m''_1}\langle a^{T*}_{l'm'}a^{E}_{l''_1m'_1}\rangle b^{T}_{l'n}w^{T}_{l''m''}w^{P}_{l''_1m''_1}\times I \\ &\times \int d\Omega_{\hat{q}} Y_{l''_1m''_1}(\hat{q})[D^{l''_1}_{m'_1M}(\hat{q},\rho(\hat{q}))b^{E}_{l''_1M}]^{*}({}_{2}Y^{*}_{lm}(\hat{q}) + {}_{-2}Y^{*}_{lm}(\hat{q})). \end{aligned} \tag{4.23}$$

Then, using the condition of statistical isotropy of the fluctuations $\langle a^{T*}_{l'm'} a^{E}_{l'_1 m'_1}\rangle = C^{TE}_{l'}\delta_{l'l'_1}\delta_{m'm'_1}$ where $C^{TE}_{l'}$ is the angular power spectrum, we get

$$\begin{aligned}\langle \tilde{C}^{TE}_{l}\rangle &= \frac{1}{2l+1}\sum_{m=-l}^{l}\sum_{l'm'}\sum_{n=-l'}^{l'}\sum_{l''m''}\sum_{l'_1 m'_1}\sum_{M=-l'_1}^{l'_1}\sum_{l''_1 m''_1} C^{TE}_{l'}\delta_{l'l'_1}\delta_{m'm'_1} b^{T}_{l'n} b^{E}_{l'_1 M} w^{T}_{l''m''} w^{P}_{l''_1 m''_1}\times I \\ &\times \int d\Omega_{\hat{q}}\Big[Y^{*}_{l''_1 m''_1}(\hat{q})\ {}_2Y_{lm}(\hat{q}) D^{l'_1}_{m'_1 M}(\hat{q},\rho(\hat{q})) \\ &+ Y^{*}_{l''_1 m''_1}(\hat{q})\ {}_{-2}Y_{lm}(\hat{q})) D^{l'_1}_{m'_1 M}(\hat{q},\rho(\hat{q}))\Big]^{*}, \end{aligned} \tag{4.24}$$

where we have made use of the reality condition of the beam harmonic transform $b^{E*}_{l'_1 M} = b^{E}_{l'_1 M}$. As only the terms that satisfy $l'_1 = l'$ and $m'_1 = m'$ contribute in the summations, we can simplify the above expression as

$$\begin{aligned}\langle \tilde{C}^{TE}_{l}\rangle &= \frac{1}{2l+1}\sum_{m=-l}^{l}\sum_{l'm'}\sum_{n=-l'}^{l'}\sum_{l''m''}\sum_{M=-l'}^{l'}\sum_{l''_1 m''_1} C^{TE}_{l'} b^{T}_{l'n} b^{E}_{l'M} w^{T}_{l''m''} w^{P}_{l''_1 m''_1}\times I \\ &\times \int d\Omega_{\hat{q}}\Big[Y^{*}_{l''_1 m''_1}(\hat{q})\ {}_2Y_{lm}(\hat{q}) D^{l'}_{m'M}(\hat{q},\rho(\hat{q})) + Y^{*}_{l''_1 m''_1}(\hat{q})\ {}_{-2}Y_{lm}(\hat{q})) D^{l'}_{m'M}(\hat{q},\rho(\hat{q}))\Big]^{*} \end{aligned} \tag{4.25}$$

from which we derive the following bias matrix

$$\begin{aligned}A^{TEcut}_{ll'} &= \frac{1}{2l+1}\sum_{m=-l}^{l}\sum_{m'=-l'}^{l'}\sum_{n=-l'}^{l'}\sum_{l''m''}\sum_{M=-l'}^{l'}\sum_{l''_1 m''_1} b^{T}_{l'n} b^{E}_{l'M} w^{T}_{l''m''} w^{P}_{l''_1 m''_1}\times I \\ &\times \int d\Omega_{\hat{q}}\Big[Y^{*}_{l''_1 m''_1}(\hat{q})\ {}_2Y_{lm}(\hat{q}) D^{l'}_{m'M}(\hat{q},\rho(\hat{q})) + Y^{*}_{l''_1 m''_1}(\hat{q})\ {}_{-2}Y_{lm}(\hat{q})) D^{l'}_{m'M}(\hat{q},\rho(\hat{q}))\Big]^{*} \end{aligned} \tag{4.26}$$

that contains the non-circular beam and cut-sky smoothing effects. In order to compute the bias matrix, we need to calculate analytically the following integral

$$J = \int d\Omega_{\hat{q}}\Big[Y^{*}_{l''_1 m''_1}(\hat{q})\ {}_2Y_{lm}(\hat{q}) D^{l'}_{m'M}(\hat{q},\rho(\hat{q})) + Y^{*}_{l''_1 m''_1}(\hat{q})\ {}_{-2}Y_{lm}(\hat{q})) D^{l'}_{m'M}(\hat{q},\rho(\hat{q}))\Big]^{*}, \tag{4.27}$$

that is involved in Eq. (4.26). We perform this task by using the relationship between the spherical harmonic functions, rotation matrices and Clebsch-Gordan coefficients. In the next section, we present a detailed derivation of the integral J which can be decomposed into the sum of two integrals $J^{*} = J_1 + J_2$ where

$$\begin{aligned} J_1 &= \int d\Omega_{\hat{q}} Y^{*}_{l''_1 m''_1}(\hat{q})\ {}_2Y_{lm}(\hat{q}) D^{l'}_{m'M}(\hat{q},\rho(\hat{q})), \\ J_2 &= \int d\Omega_{\hat{q}} Y^{*}_{l''_1 m''_1}(\hat{q})\ {}_{-2}Y_{lm}(\hat{q})) D^{l'}_{m'M}(\hat{q},\rho(\hat{q})). \end{aligned} \tag{4.28}$$

We report in Appendix E and F the derivations of the integrals J_1 and J_2, and obtain their sum J in the following form

$$\begin{aligned} J &= \frac{(-1)^m}{2}\sqrt{(2l_1''+1)(2l+1)}\sum_{L=|l-l'|}^{l+l'} C_{l-ml'm'}^{L(-m+m')}\sum_{L'=|l_1''-L|}^{l_1''+L} C_{l_1''(m-m')L(-m+m')}^{L'0} \\ &\times \left[C_{l2l'M}^{L(2+M)} C_{l_1''0L(2+M)}^{L'(2+M)} \sum_{N=-L'}^{L'} d_{0N}^{L'}(\frac{\pi}{2}) d_{N(2+M)}^{L'}(\frac{\pi}{2}) f_{(2+M)N} \right. \\ &+ \left. C_{l-2l'M}^{L(-2+M)} C_{l_1''0L(-2+M)}^{L'(-2+M)} \sum_{N=-L'}^{L'} d_{0N}^{L'}(\frac{\pi}{2}) d_{N(-2+M)}^{L'}(\frac{\pi}{2}) f_{(-2+M)N} \right]. \end{aligned} \tag{4.29}$$

By plugging Eq. (D.12) and Eq. (4.29) in Eq. (4.26), we may write the coupling matrix as follows

$$\begin{aligned} A_{ll'}^{TEcut} &= \frac{1}{2l+1}\sum_{m=-l}^{l}\sum_{m'=-l'}^{l'}\sum_{n=-l'}^{l'}\sum_{l''m''}\sum_{M=-l'}^{l'}\sum_{l_1''m_1''} b_{l'n}^{T} b_{l'M}^{E} w_{l''m''}^{T} w_{l_1''m_1''}^{P} (-1)^{m+m''}\frac{\sqrt{(2l+1)(2l''+1)}}{4\pi} \\ &\times \sum_{L=|l-l''|}^{l+l''} C_{l0l''0}^{L0}\, C_{lml''m''}^{L(m+m'')} \sum_{L'=|L-l'|}^{L+l'} C_{L-(m+m'')l'm'}^{L'(m'-m-m'')}\, C_{L0l'n}^{L'n}\, 2\pi \sum_{N=-L'}^{L'} d_{0N}^{L'}(\frac{\pi}{2}) d_{Nn}^{L'}(\frac{\pi}{2}) f_{nN} \\ &\times \frac{(-1)^m}{2}\sqrt{(2l_1''+1)(2l+1)}\sum_{L=|l-l'|}^{l+l'} C_{l-ml'm'}^{L(-m+m')}\sum_{L'=|l_1''-L|}^{l_1''+L} C_{l_1''(m-m')L(-m+m')}^{L'0} \\ &\times \left[C_{l2l'M}^{L(2+M)} C_{l_1''0L(2+M)}^{L'(2+M)} \sum_{N=-L'}^{L'} d_{0N}^{L'}(\frac{\pi}{2}) d_{N(2+M)}^{L'}(\frac{\pi}{2}) f_{(2+M)N} \right. \\ &+ \left. C_{l-2l'M}^{L(-2+M)} C_{l_1''0L(-2+M)}^{L'(-2+M)} \sum_{N=-L'}^{L'} d_{0N}^{L'}(\frac{\pi}{2}) d_{N(-2+M)}^{L'}(\frac{\pi}{2}) f_{(-2+M)N} \right]. \end{aligned} \tag{4.30}$$

The expression of this bias matrix can be simplified since we have seen that for the calculation of the integrals I and J, only the terms which satisfy $m'-m-m''=0$ and $m_1''-m+m'=0$ contribute in the summations. This means that the number of summations involved in the calculation is reduced by a factor of two since $m''=m'-m$ and $m_1''=m-m'$. We account for these conditions in the bias matrix summations, and after simplification we obtain the final expression of the bias in the

following form

$$
\begin{aligned}
A_{ll'}^{TEcut} &= \frac{1}{4}\sum_{m=-l}^{l}\sum_{m'=-l'}^{l'}\sum_{n=-l'}^{l'}\sum_{M=-l'}^{l'}\sum_{l''=0}^{\infty}\sum_{l_1''=0}^{\infty}(-1)^{m+m'}\sqrt{(2l''+1)(2l_1''+1)}b_{l'n}^{T}b_{l'M}^{E}w_{l''(m'-m)}^{T}w_{l_1''(m-m')}^{P} \\
&\times \sum_{L=|l-l''|}^{l+l''} C_{l0l''0}^{L0}\, C_{lml''(m'-m)}^{Lm'} \sum_{L'=|L-l'|}^{L+l'} C_{L-m'l'm'}^{L'0}\, C_{L0l'n}^{L'n} \sum_{N=-L'}^{L'} d_{0N}^{L'}(\frac{\pi}{2}) d_{Nn}^{L'}(\frac{\pi}{2}) f_{nN} \\
&\times \sum_{L=|l-l'|}^{l+l'} C_{l-ml'm'}^{L(-m+m')} \sum_{L'=|l_1''-L|}^{l_1''+L} C_{l_1''(m-m')L(-m+m')}^{L'0} \\
&\times \Bigg[C_{l2l'M}^{L(2+M)} C_{l_1''0L(2+M)}^{L'(2+M)} \sum_{N=-L'}^{L'} d_{0N}^{L'}(\frac{\pi}{2}) d_{N(2+M)}^{L'}(\frac{\pi}{2}) f_{(2+M)N} \\
&+ C_{l-2l'M}^{L(-2+M)} C_{l_1''0L(-2+M)}^{L'(-2+M)} \sum_{N=-L'}^{L'} d_{0N}^{L'}(\frac{\pi}{2}) d_{N(-2+M)}^{L'}(\frac{\pi}{2}) f_{(-2+M)N} \Bigg]. \qquad (4.31)
\end{aligned}
$$

The upper limits of the summations over l'' and l_1'' are fixed by the choice of the temperature and the polarization masks, and the summations over the indices m and m' are constrained by the number of modes $(m'-m)$. Mitra et al. [140] have demonstrated that the computational cost of the bias matrix calculation can be reduced by constructing azimuthally apodized masks. In such case, only the first 10-20 $(m'-m)$ modes contribute significantly when the sky temperature map is smoothed with an apodized mask. Then, we may write the general form of the bias matrix with a cut-sky smoothed with an apodized temperature mask $w_{l''(m'-m)}^{T}$ and polarization mask $w_{l_1''(m-m')}^{P}$ with a non-circular beam as

$$
\begin{aligned}
A_{ll'}^{TEcut} &= \frac{1}{4}\sum_{m=-l}^{l}\sum_{m'=-l'}^{l'}\sum_{n=-l'}^{l'}\sum_{M=-l'}^{l'}\sum_{l''=0}^{l''_{max}}\sum_{l_1''=0}^{l''_{1\max}}(-1)^{m+m'}\sqrt{(2l''+1)(2l_1''+1)}b_{l'n}^{T}b_{l'M}^{E}w_{l''(m'-m)}^{T}w_{l_1''(m-m')}^{P} \\
&\times \sum_{L=|l-l''|}^{l+l''} C_{l0l''0}^{L0}\, C_{lml''(m'-m)}^{Lm'} \sum_{L'=|L-l'|}^{L+l'} C_{L-m'l'm'}^{L'0}\, C_{L0l'n}^{L'n} \sum_{N=-L'}^{L'} d_{0N}^{L'}(\frac{\pi}{2}) d_{Nn}^{L'}(\frac{\pi}{2}) f_{nN} \\
&\times \sum_{L=|l-l'|}^{l+l'} C_{l-ml'm'}^{L(-m+m')} \sum_{L'=|l_1''-L|}^{l_1''+L} C_{l_1''(m-m')L(-m+m')}^{L'0} \\
&\times \Bigg[C_{l2l'M}^{L(2+M)} C_{l_1''0L(2+M)}^{L'(2+M)} \sum_{N=-L'}^{L'} d_{0N}^{L'}(\frac{\pi}{2}) d_{N(2+M)}^{L'}(\frac{\pi}{2}) f_{(2+M)N} \\
&+ C_{l-2l'M}^{L(-2+M)} C_{l_1''0L(-2+M)}^{L'(-2+M)} \sum_{N=-L'}^{L'} d_{0N}^{L'}(\frac{\pi}{2}) d_{N(-2+M)}^{L'}(\frac{\pi}{2}) f_{(-2+M)N} \Bigg], \qquad (4.32)
\end{aligned}
$$

where the summations over n and M are limited to the dominant modes $n = 0, \pm 2, \pm 4$ and $M = \pm 2, \pm 4, \pm 6$ of the temperature and polarized beam harmonic transforms $b^T_{l'n}$ and $b^E_{l'M}$.

Eq. (4.32) is the main result of this chapter. It allows the estimation of the bias when the non-circular beams in CMB polarization experiments are treated as circular, in the presence of a non-uniform/cut-sky coverage. The formula is valid for a non-rotating beam, although the formalism developed can be, in the future, extended to a broader class of scanning strategies. Given the model of beam, the bias matrix can be numerically computed. Similarly to the non-circular beam and full sky case, we may adopt the model of beam developed in Fosalba et al. [66]. In this model the bias estimate is sufficiently accurate by including a second order corrections to the beam ellipticity and considering three modes of the perturbative expansion for each beam harmonic transforms ($b^T_{l'n}$ and $b^E_{l'M}$). In the next section, we check the consistency of the above results by considering the limiting case of a full sky coverage and non-circular beams.

4.5 The full sky and non-circular beam limit for TE

In the case of a full sky coverage, we can recover the expression of the bias matrix by setting the weight function to one, i.e. $w(\hat{q}) = 1$. Then, we may use Eq. (1), Section 5.9.1 of [146] to write the harmonic transform of the mask in the form

$$w^T_{lm} = \int d\Omega_{\hat{q}} Y^*_{lm}(\hat{q}) = \sqrt{4\pi}\delta_{l0}\delta_{m0}. \tag{4.33}$$

Obviously, the only non-vanishing terms are obtained for $l = 0$ and $m = 0$. If we apply these conditions to the weight functions $w^T_{l''(m'-m)}$ and $w^P_{l''_1(m-m')}$, we see that only the terms that satisfy the conditions $l'' = 0$, $m' = m$ and $l''_1 = 0$ contribute in the summations of the bias matrix. From the lower limit of the summations involved in Eq. (4.32), we find that the conditions on l'' and l''_1 imply $L = l$ for the temperature, and $L' = l$ for the polarization part of the summations. Therefore, we can simplify the analytical expression of the bias matrix and write

$$\begin{aligned}
A^{TEfull}_{ll'} &= \pi \sum_{m=-l}^{l} \sum_{n=-l'}^{l'} \sum_{M=-l'}^{l'} b^T_{l'n} b^E_{l'M} C^{l0}_{l000}\, C^{lm}_{lm00} \\
&\times \sum_{L'=|l-l'|}^{l+l'} C^{L'0}_{l-ml'm}\, C^{L'n}_{l0l'n} \sum_{N=-L'}^{L'} d^{L'}_{0N}(\tfrac{\pi}{2}) d^{L'}_{Nn}(\tfrac{\pi}{2}) f_{nN} \sum_{L=|l-l'|}^{l+l'} C^{L0}_{l-ml'm} C^{L0}_{00L0} \\
&\times \Bigg[C^{L(2+M)}_{l2l'M} C^{L(2+M)}_{00L(2+M)} \sum_{N=-L}^{L} d^{L}_{0N}(\tfrac{\pi}{2}) d^{L}_{N(2+M)}(\tfrac{\pi}{2}) f_{(2+M)N} \\
&+ C^{L(-2+M)}_{l-2l'M} C^{L(-2+M)}_{00L(-2+M)} \sum_{N=-L}^{L} d^{L}_{0N}(\tfrac{\pi}{2}) d^{L}_{N(-2+M)}(\tfrac{\pi}{2}) f_{(-2+M)N} \Bigg].
\end{aligned} \tag{4.34}$$

We use Eq. (2) of Section 8.5 of [146] to derive the following relations

$$\begin{aligned} C^{l0}_{l000} &= 1, \\ C^{lm}_{lm00} &= 1. \end{aligned} \tag{4.35}$$

From the symmetry properties of the Clebsch-Gordan coefficients, we may write using Eq. (10), Section 8.4.3 of [146]

$$C^{L0}_{00L0} = C^{L0}_{L000} = 1. \tag{4.36}$$

Then we apply successively Eq. (10), Section 8.4.3 of [146] and Eq. (2) of Section 8.5 of [146] to obtain

$$\begin{aligned} C^{L(2+M)}_{00L(2+M)} &= C^{L(2+M)}_{L(2+M)00} = 1, \\ C^{L(-2+M)}_{00L(-2+M)} &= C^{L(-2+M)}_{L(-2+M)00} = 1, \end{aligned} \tag{4.37}$$

which yield the following bias matrix

$$\begin{aligned} A^{TEfull}_{ll'} &= \pi \sum_{m=-l}^{l} \sum_{n=-l'}^{l'} \sum_{M=-l'}^{l'} b^{T}_{l'n} b^{E}_{l'M} \\ &\times \sum_{L'=|l-l'|}^{l+l'} C^{L'0}_{l-ml'm}\, C^{L'n}_{l0l'n} \sum_{N=-L'}^{L'} d^{L'}_{0N}(\frac{\pi}{2}) d^{L'}_{Nn}(\frac{\pi}{2}) f_{nN} \sum_{L=|l-l'|}^{l+l'} C^{L0}_{l-ml'm} \\ &\times \Bigg[C^{L(2+M)}_{l2l'M} \sum_{N=-L}^{L} d^{L}_{0N}(\frac{\pi}{2}) d^{L}_{N(2+M)}(\frac{\pi}{2}) f_{(2+M)N} \\ &+ C^{L(-2+M)}_{l-2l'M} \sum_{N=-L}^{L} d^{L}_{0N}(\frac{\pi}{2}) d^{L}_{N(-2+M)}(\frac{\pi}{2}) f_{(-2+M)N} \Bigg]. \end{aligned} \tag{4.38}$$

It is convenient to rearrange the summation indices of the above equation in order to avoid any confusion on the modes coupling between the temperature and E-component of the polarization. We can change the dummy indices of the summations without altering the results as follows: $n \to m''$, $M \to M'$, and the index N of the summation involved in the first part of the correlation

(temperature expansion multipoles) is changed to M ($N \to M$). Then, the bias matrix reduces to

$$\begin{aligned} A_{ll'}^{TEfull} &= \pi \sum_{m=-l}^{l} \sum_{m''=-l'}^{l'} \sum_{M'=-l'}^{l'} b_{l'm''}^{T} b_{l'M'}^{E} \\ &\times \sum_{L'=|l-l'|}^{l+l'} C_{l-ml'm}^{L'0} \, C_{l0l'm''}^{L'm''} \sum_{M=-L'}^{L'} d_{0M}^{L'}(\frac{\pi}{2}) d_{Mm''}^{L'}(\frac{\pi}{2}) f_{m''M} \sum_{L=|l-l'|}^{l+l'} C_{l-ml'm}^{L0} \\ &\times \left[C_{l2l'M'}^{L(2+M')} \sum_{N=-L}^{L} d_{0N}^{L}(\frac{\pi}{2}) d_{N(2+M')}^{L}(\frac{\pi}{2}) f_{(2+M')N} \right. \\ &+ \left. C_{l-2l'M'}^{L(-2+M')} \sum_{N=-L}^{L} d_{0N}^{L}(\frac{\pi}{2}) d_{N(-2+M')}^{L}(\frac{\pi}{2}) f_{(-2+M')N} \right]. \end{aligned} \tag{4.39}$$

We can see that we have recovered Eq. (3.50) which gives the expression of the bias matrix in the full sky limit when the beam pattern is non-circular (asymmetric).

4.6 The cut-sky and circular beam limit

It is important to verify the consistency of the general formula of the TE bias matrix that we have obtained in the case of a non-circular beam and incomplete sky coverage. We have seen in the previous section that we have reproduced the result of the bias matrix expression in the limiting case of a non-circular beam and full sky coverage. Hereafter, we investigate the limiting case of a cut-sky and circular beam. This limit is practically very useful in CMB experiment analysis when the beam is assumed as circular (axisymmetric). A galactic mask is applied to remove the CMB foreground contaminants (polarized and non-polarized ones) resulting to a non-uniform/partial sky coverage.

In the following, we calculate the bias matrix that only accounts for the effect of the cut-sky. When the beam is circulary symmetric, the perturbative expansion of the beam in harmonic space reduces to the first term which is identical to a circular Gaussian window. This implies that in Eq. (4.32), $n = 0$ for the total intensity, and $M = \pm 2$ for the polarized beam transforms. Let Σ be the sum of the terms over M ($M = \pm 2$) which appear in Eq. (4.32). As a result of the reality condition of the beam harmonic transform, we have $b_{l-m} = b_{lm}$ so that we may write

$$\begin{aligned} \Sigma &= b_{l'2}^{E} \left[C_{l2l'-2}^{L0} C_{l''_1 0L0}^{L'0} \sum_{N=-L'}^{L'} d_{0N}^{L'}(\frac{\pi}{2}) d_{N0}^{L'}(\frac{\pi}{2}) f_{0N} + C_{l-2l'-2}^{L-4} C_{l''_1 0L-4}^{L'-4} \sum_{N=-L'}^{L'} d_{0N}^{L'}(\frac{\pi}{2}) d_{N-4}^{L'}(\frac{\pi}{2}) f_{-4N} \right. \\ &+ \left. C_{l2l'2}^{L4} C_{l''_1 0L4}^{L'4} \sum_{N=-L'}^{L'} d_{0N}^{L'}(\frac{\pi}{2}) d_{N4}^{L'}(\frac{\pi}{2}) f_{4N} + C_{l-2l'2}^{L0} C_{l''_1 0L0}^{L'0} \sum_{N=-L'}^{L'} d_{0N}^{L'}(\frac{\pi}{2}) d_{N0}^{L'}(\frac{\pi}{2}) f_{0N} \right]. \end{aligned} \tag{4.40}$$

We use the following Equation (A.6) derived in Appendix A to calculate the summation Σ:

$$\sum_{M=-L'}^{L'} d^{L'}_{0M}(\frac{\pi}{2}) d^{L'}_{M0}(\frac{\pi}{2}) f_{0M} = \frac{2}{2L'+1}\delta_{L'0}. \tag{4.41}$$

This implies that the only non-vanishing term in the summation $\sum_{M=-L'}^{L'} d^{L'}_{0M}(\frac{\pi}{2}) d^{L'}_{M0}(\frac{\pi}{2}) f_{0M}$ is obtained for $L' = 0$. This condition itself implies that the second and third terms of Σ do not contribute since the Clebsch-Gordan coefficients and Wigner-d function in these terms vanish unless $L' \geq 4$. Hence the summation reduces to

$$\begin{aligned} \Sigma &= 2b^E_{l'2}\left(C^{L0}_{l2l'-2}C^{00}_{l''_1 0L0} + C^{L0}_{l-2l'2}C^{00}_{l''_1 0L0}\right) \\ &= 2b^E_{l'2}\left(C^{L0}_{l2l'-2} + C^{L0}_{l-2l'2}\right)C^{00}_{l''_1 0L0}. \end{aligned} \tag{4.42}$$

Using Eq. (1) of Section 8.5 of [146] we have

$$C^{00}_{l''_1 0L0} = (-1)^{l''_1}\frac{\delta_{l''_1 L}}{\sqrt{2l''_1+1}}, \tag{4.43}$$

which results in the condition $l''_1 = L$ in the summation over the index l''_1. The symmetry properties defined by Eq. (11), Section 8.4.3 of [146] allow us to write

$$C^{L0}_{l2l'-2} = (-1)^{l+l'+L}C^{L0}_{l-2l'2}, \tag{4.44}$$

and therefore, Σ can be written as

$$\Sigma = 2b^E_{l'2}((-1)^{l+l'+L}+1)C^{L0}_{l-2l'2}(-1)^{l''_1}\frac{\delta_{l''_1 L}}{\sqrt{2l''_1+1}}. \tag{4.45}$$

Putting the conditions $L' = 0$ and $l''_1 = L$ all together and using Eq. (1) of Section 8.5 of [146], we obtain the following relations between the Clebsch coefficients:

$$C^{L'0}_{L-m'l'm'} = C^{00}_{L-m'l'm'} = (-1)^{L+m'}\frac{\delta_{Ll'}}{\sqrt{2L+1}}, \tag{4.46}$$

$$C^{L'n}_{L0l'n} = C^{00}_{L0l'0} = (-1)^{L}\frac{\delta_{Ll'}}{\sqrt{2L+1}}, \tag{4.47}$$

$$C^{L(-m+m')}_{l-ml'm'} = C^{l''_1(-m+m')}_{l-ml'm'}, \tag{4.48}$$

$$C^{L'0}_{l''_1(m-m')L(-m+m')} = C^{00}_{l''_1(m-m')L(-m+m')} = (-1)^{l''_1+m+m'}\frac{\delta_{l''_1 L}}{\sqrt{2l''_1+1}}, \tag{4.49}$$

from which we derive

$$C^{L'0}_{L-m'l'm'}C^{L'n}_{L0l'n} = \frac{(-1)^{m'}}{2L+1}\delta_{Ll'}. \tag{4.50}$$

This means that the summation over L in the term containing the polarized component of the multipole coefficients is reduced to $L = l'$, and zero elsewhere. Taking into account the different conditions on the summation indices, we resume the analytical expression of the bias matrix as follows

$$\begin{aligned} A^{TEcut}_{ll'circ} &= \frac{1}{4}\sum_{m=-l}^{l}\sum_{m'=-l'}^{l'}\sum_{l''=0}^{l''_{max}}\sum_{l''_1=0}^{l''_{1\max}}(-1)^{m+m'}\sqrt{(2l''+1)(2l''_1+1)}b^T_{l'0}b^E_{l'2}w^T_{l''(m'-m)}w^P_{l''_1(m-m')} \\ &\times C^{l'0}_{l0l''0}\, C^{l'm'}_{lml''(m'-m)}\frac{(-1)^{m'}}{2l'+1}\times 2 \\ &\times C^{l''_1(-m+m')}_{l-ml'm'}(-1)^{l''_1+m+m'}\frac{1}{\sqrt{2l''_1+1}} \\ &\times 2((-1)^{l+l'+l''_1}+1)C^{l''_10}_{l-2l'2}(-1)^{l''_1}\frac{1}{\sqrt{2l''_1+1}}, \end{aligned} \tag{4.51}$$

which translates to

$$\begin{aligned} A^{TEcut}_{ll'circ} &= \frac{1}{2l'+1}\sum_{m=-l}^{l}\sum_{m'=-l'}^{l'}\sum_{l''=0}^{l''_{max}}\sum_{l''_1=0}^{l''_{1\max}}(-1)^{m'}\sqrt{\frac{2l''+1}{2l''_1+1}}b^T_{l'0}b^E_{l'2}\; w^T_{l''(m'-m)}w^P_{l''_1(m-m')} \\ &\times ((-1)^{l+l'+l''_1}+1)C^{l'0}_{l0l''0}\, C^{l'm'}_{lml''(m'-m)}C^{l''_1(-m+m')}_{l-ml'm'}C^{l''_10}_{l-2l'2}. \end{aligned} \tag{4.52}$$

Replacing the beam harmonic transforms by their values, we obtain the bias matrix $A^{TEcut}_{ll'circ}$ in the limiting case of a circular beam and cut-sky in the following form

$$\begin{aligned} A^{TEcut}_{ll'circ} &= \frac{1}{8\pi}e^{-l'^2\sigma^2}\sum_{m=-l}^{l}\sum_{m'=-l'}^{l'}\sum_{l''=0}^{l''_{max}}\sum_{l''_1=0}^{l''_{1\max}}(-1)^{m'}\sqrt{\frac{2l''+1}{2l''_1+1}}\; w^T_{l''(m'-m)}w^P_{l''_1(m-m')} \\ &\times ((-1)^{l+l'+l''_1}+1)C^{l'0}_{l0l''0}\, C^{l'm'}_{lml''(m'-m)}C^{l''_1(-m+m')}_{l-ml'm'}C^{l''_10}_{l-2l'2}, \end{aligned} \tag{4.53}$$

where σ is the effective beam width (geometric mean) of the circular Gaussian beam. Prior to the power spectrum estimation, the sky must be smoothed with the temperature and polarization masks weighted by w^T and w^P. In the following section, we establish the validity of our formula by showing that it can recover the expression of the bias matrix $A^{TEfull}_{ll'circ}$ in the case of a complete sky coverage and symmetric beam.

4.7 The full sky and circular beam limit

The result of the bias matrix in the trivial case of a survey using a symmetric beam and full sky coverage has been already mentioned in Appendix A. We assign the value 1 to the mask function since we consider all sky pixels. Thus, the conditions $w^T(\hat{q}) = 1$ and $w^P(\hat{q}) = 1$ imply

$$\begin{aligned} w^T_{l''(m'-m)} &= \int d\Omega_{\hat{q}} Y^*_{l''(m'-m)}(\hat{q}) = \sqrt{4\pi}\delta_{l''0}\delta_{(m'-m)0}, \\ w^P_{l''_1(m-m')} &= \int d\Omega_{\hat{q}} Y^*_{l''_1(m-m')}(\hat{q}) = \sqrt{4\pi}\delta_{l''_1 0}\delta_{(m-m')0}. \end{aligned} \tag{4.54}$$

As a result, the only non-vanishing terms in the summations involved in the bias matrix are obtained for $m' = m$, $l'' = 0$ and $l''_1 = 0$. Replacing this in Eq. (4.53) we get

$$A^{TEcut}_{ll'circ} = \frac{1}{8\pi} e^{-l'^2\sigma^2} \sum_{m=-l}^{l} (-1)^m \times 4\pi((-1)^{l+l'} + 1) C^{l'0}_{l000}\, C^{l'm}_{lm00} C^{00}_{l-ml'm} C^{00}_{l-2l'2}. \tag{4.55}$$

The Clebsch-Gordan coefficients can be derived using Eq. (1) and Eq. (2), Section 8.5 of [146] as

$$\begin{aligned} C^{l'0}_{l000} &= \delta_{ll'}, \\ C^{l'm}_{lm00} &= \delta_{ll'}, \\ C^{00}_{l-ml'm} &= (-1)^{l+m} \frac{\delta_{ll'}}{\sqrt{2l+1}}, \\ C^{00}_{l-2l'2} &= (-1)^{l} \frac{\delta_{ll'}}{\sqrt{2l+1}}. \end{aligned} \tag{4.56}$$

Consequently, the only non-vanishing term is obtained for $l = l'$, and the bias matrix becomes diagonal. Plugging the above set of expressions in Eq. (4.55), we find

$$A^{TEcut}_{ll'circ} = \frac{1}{8\pi} e^{-l^2\sigma^2} \sum_{m=-l}^{l} (-1)^m \times 8\pi(-1)^m \frac{\delta_{ll'}}{2l+1}, \tag{4.57}$$

which after reduction, gives the following relation

$$A^{TEcut}_{ll'circ} = e^{-l^2\sigma^2}\delta_{ll'}. \tag{4.58}$$

Then, we have reproduced the well-known expression of the bias matrix of the TE correlation for a symmetric (circular) beam and complete sky (see, [145, 147]).

4.8 Discussion

We have considered in this chapter the derivation of the analytical expression of the TE bias matrix by simultaneously taking into account the beam asymmetry and partial sky coverage. Most CMB experiments deal with incomplete sky coverage since even for full sky missions, the parasitic foreground signals dominate the Galactic plane noise (see, [65]). The elimination of the corrupted signals across the Galactic plane along with the polarized astrophysical sources, realized through the masking of the corresponding regions, results in a cut-sky coverage. We have seen that the TE bias matrix obtained in Eq. (4.32) can reproduce the result of the TE bias matrix of non-circular beams in the limiting case of a full sky coverage. The latter has been derived in Chapter 3. We have also demonstrated the consistency of the TE bias matrix formula in the case of a CMB experiment using circularly symmetric beams in a partial sky.

The evaluation of the TE bias matrix in Eq. (4.32) requires the computation of nested loops. The outer loop which does not appear in the expression of the TE bias matrix, corresponds to the summation over the multipole l'. The summations over the beam harmonic transforms n and M modes do not contribute to the computational cost since they are limited to $n = 0,\ \pm 2,\ \pm 4$ and $M = \pm 2,\ \pm 4, \pm 6$. The summations over the masks multipoles l'' and l''_1 are fixed by the multipoles cut-off l''_{max} and l''_{1max}. A reduction in computation time by a large factor can be obtained by choosing the azimuthally apodized temperature mask of Mitra et al. [140] whose harmonic transforms rapidly decrease with the mode $(m' - m)$ for a given l'', and $|w^T_{l''(m'-m)}|^2$ also dies down with l''. Under this condition, only the first 10-20 modes $(m' - m)$ are significant and the multipole l'' cut-off is $l''_{max} \sim 100$. The bias matrix calculation involves nine loops which correspond to a computational cost $\sim O(l^9_{max})$. However, this can be reduced by introducing some constraints in the evaluation of the bias. As the modes m and m' are related through the mask modes cut-off, the computation time is reduced by a power of l. Further improvement of the computation time by a factor of $\sim l/\Delta l$ can also be obtained by considering a narrow band $\Delta l = |l - l'| \leq 20$ around the diagonal of the bias matrix. This operation is allowed without compromising the accuracy of the bias estimate since the coupling matrix is close to diagonal. The off-diagonal elements of the bias matrix just describe the significance of the power mixing between multipoles when non-circular beams and partial sky coverage are used in CMB experiments. The exploitation of the symmetry properties of the Wigner-d functions introduces a speedup factor of an order of magnitude (see, [140]).

As we have seen in Chapter 3, the computation time of the Wigner-d functions scales as $O(l^{4.2}_{max})$, then the precomputation of these functions will save a large amount of time. The computation time can be drastically reduced by precomputing all Wigner-d functions involved in the calculation of the TE bias matrix. The next step of the optimization of the computation time consists to evaluate the Clebsch-Gordan coefficients. It is more convenient to compute these coefficients directly on the fly as the corresponding computation time scales as $O(l^{2.6}_{max})$, and therefore they can be computed

more rapidly than the Wigner-d function. Finally, a parallel code should be implemented in order to compute the bias matrix in a reasonable time.

The numerical implementation of the TE bias matrix, which is computationally intensive, follows the same procedure as the full sky and non-circular beam case, but only differs by the utilization of a parallel computation on computer clusters. The latter step belongs to a future work.

Chapter 5

Non-circular beam and cut-sky for EE polarized signals

5.1 Introduction

We present in this chapter the derivation of the bias matrices $A^{EE}_{ll'}$ and $A^{BB}_{ll'}$ that relate the observed power spectrum $\tilde{C}^{EE}_{l}$ to the true power spectra $C^{EE}_{l'}$ and $C^{BB}_{l'}$ of the E and B-polarization autocorrelations. As the amplitude of the E-polarization signals is relatively weaker than the total intensity, it is necessary to take into account the foreground systematics (synchrotron and dust emission polarized sources) and correct the corresponding estimator bias. This naturally requires the suppression of the undesirable foreground contaminants of CMB polarized signals. A weighted mask function is applied to the sky polarization map in order to complete this operation. Unfortunately, the consideration of an incomplete sky as a result of the foreground residuals removal modifies the nature of the initial pseudo-C_l estimator: the B-mode is leaking to the E-mode and vice-versa [128]. This means that the estimator itself becomes a source of "noise" . For an ensemble of realizations containing only E-mode, the estimated power of the B-mode in each realization will not be zero, so that the E-mode power contributes to the variance of the B-mode. If the instrument noise is small, the estimator "noise" alone can dominate the sample variance in the lensing B-mode [45]. In the latter case, the B-mode originates from CMB gravitational lensing by large scale structure which generates B-mode from the primary E-mode [158].

This property of the standard pseudo-C_l estimator, which limits the tensor to scalar ratio (ratio between the primordial gravitational wave and curvature power spectra [159]) that can be detected to ~ 0.05, inevitably hinders the detection of primordial gravitational waves imprinted in the B-mode tensor perturbations since the leaking power $C^{EE}_{l'} \gg C^{BB}_{l'}$. As our main focus is on the estimation of the power spectrum $\tilde{C}^{EE}_{l}$ through the bias matrices, the main concern here is the B-mode leaking to the E-mode. In our calculations, we ignore this effect by estimating the power

spectrum of the E- mode signal using the standard pseudo-C_l since the variance $C_{l'}^{EE}$ is much larger than $C_{l'}^{BB}$.

In realistic CMB polarimetry experiments the decomposition of the electric and magnetic components of the polarized signals is not unique in the presence of boundaries as a result of the fraction of the sky observed. In other words, the E and B-modes are non-local quantities by construction. The elimination of the estimator "noise", leading to a clean separation between E and B-modes, is feasible by constructing the so-called "pure" pseudo-C_l estimator which does not mix the E and B-modes [128, 160–163]. Two methods have been proposed to alleviate the mixing problem: correction based on a heuristically-weighted correlation functions [42] and direct construction on pixels map [161].

Other approaches of the polarization power spectrum estimation which make a clean separation between the E and B-mode components of the polarized signals exist, though they are either hampered by the numerical complexity [164] or convergence [165] of the implementation. The "pure" pseudo-C_l estimator turns out to be a good alternative for handling those issues.

Nevertheless, our intention is not to compute the EE power spectrum with the "pure" estimators. In this chapter, we adopt the standard pseudo-C_l estimator and derive the expression of the bias matrices. This signifies that even in the absence of an instrumental noise, the mean variance of the EE power spectrum contains a leaking B-mode power.

In fact, the utilization of a mask function for the sky smoothing renders complicated the computation of the bias matrix as a result of the non-uniformity of the sky. We include the effect of both non-circular (asymmetric) beam and incomplete sky coverage, and evaluate the computational cost of the bias matrices numerical implementation. Then, we will address the calculation of the bias matrices in the full sky limit where on small angular scales the problem of mixing is negligible [128, 160] so that we can reasonably estimate the EE bias matrices with sufficient accuracy. However, at large angular scales, the power mixing between E and B remains an important issue in the CMB polarization power spectrum estimation.

5.2 E-polarization multipole coefficients

We follow the approach developed in Section 4.3 of Chapter 4 which provides the expression of the harmonic transform of the E-mode polarized field. We expand the linearly polarized E-mode radiation in spherical harmonic basis. The multipole expansions of the CMB polarized signals are connected to the observable Stokes parameters Q and U as (e.g., [145])

$$(Q \pm iU)(\hat{q}) = \sum_{lm} (a_{lm}^{E} \mp i a_{lm}^{B}) \; {}_{\mp 2}Y_{lm}(\hat{q}). \tag{5.1}$$

If we attempt to estimate directly the power spectrum from the autocorrelation of the multipole harmonics a^E_{lm}, we will achieve nothing in correcting the systematics bias. Instead, we must modify the above formula to account for the beam smoothing with an elliptical window and the masking of the sky corrupted pixels. Using a simple algebra, we derive from Eq. (5.1) the sky multipole harmonic transforms and write

$$a^E_{lm} = \frac{1}{2}\int d\Omega_{\hat{q}}[(Q-iU)(\hat{q})\ {}_2Y^*_{lm}(\hat{q}) + (Q+iU)(\hat{q})\ {}_{-2}Y^*_{lm}(\hat{q})]. \tag{5.2}$$

Fosalba et al. [66] have considered the beam systematic effects in polarization experiments and derived a formula which gives the expression of the corresponding smoothed (effective) Stokes parameters Q_{eff} and U_{eff} of the beam convolved with the sky as

$$Q_{eff} = 2\sum_{lmM}[D^l_{mM}(\hat{q},\rho(\hat{q}))]^*\ b^{E*}_{lM}\ a^E_{lm}, \tag{5.3}$$

$$U_{eff} = 2\sum_{lmM}[D^l_{mM}(\hat{q},\rho(\hat{q}))]^*\ b^{E*}_{lM}\ a^B_{lm}. \tag{5.4}$$

The correction of the non-uniformity of the sky coverage is done by following the approach described in the appendix of Kogut et al. [116]. If we include both corrections of the systematics, we get the following new multipole coefficients

$$\tilde{a}^E_{lm} = \frac{1}{2}\int d\Omega_{\hat{q}} w^P(\hat{q})[(Q-iU)_{eff}(\hat{q})\ {}_2Y^*_{lm}(\hat{q}) + (Q+iU)_{eff}(\hat{q})\ {}_{-2}Y^*_{lm}(\hat{q})], \tag{5.5}$$

where $w^P(\hat{q})$ denotes the polarization mask weighting function. We plug in Eq. (5.5) the Stokes parameters Q_{eff} and U_{eff} that yield

$$\begin{aligned}\tilde{a}^E_{lm} &= \sum_{l'm'}\sum_{M=-l'}^{l'}\int d\Omega_{\hat{q}} w^P(\hat{q})[D^{l'}_{m'M}(\hat{q},\rho(\hat{q}))b^E_{l'M}]^* \\ &\times\ [a^E_{l'm'}(\ {}_2Y^*_{lm}(\hat{q}) + {}_{-2}\,Y^*_{lm}(\hat{q})) - ia^B_{l'm'}(\ {}_2Y^*_{lm}(\hat{q}) - {}_{-2}\,Y^*_{lm}(\hat{q}))].\end{aligned} \tag{5.6}$$

The expansion of the polarization weight function in spherical harmonic space reads

$$w^P(\hat{q}) = \sum_{l''m''} w^P_{l''m''}Y_{l''m''}(\hat{q}), \tag{5.7}$$

which leads to the following expression of the multipole coefficients

$$\begin{aligned}\tilde{a}^{E}_{lm} &= \sum_{l'm'}\sum_{M=-l'}^{l'}\sum_{l''m''} w^{P}_{l''m''}\int d\Omega_{\hat{q}} Y_{l''m''}(\hat{q})[D^{l'}_{m'M}(\hat{q},\rho(\hat{q}))b^{E}_{l'M}]^{*} \\ &\times \; [a^{E}_{l'm'}(\,{}_{2}Y^{*}_{lm}(\hat{q}) + {}_{-2}Y^{*}_{lm}(\hat{q})) - ia^{B}_{l'm'}(\,{}_{2}Y^{*}_{lm}(\hat{q}) - {}_{-2}Y^{*}_{lm}(\hat{q}))]. \end{aligned} \tag{5.8}$$

The next step is now to evaluate the complex conjugate $\tilde{a}^{E*}_{lm}$ of the multipole coefficients in order to compute the autocorrelation of the sky multipoles $\tilde{a}^{E}_{lm}$. Thus, we have

$$\begin{aligned}\tilde{a}^{E*}_{lm} &= \sum_{l'_1m'_1}\sum_{M_1=-l'_1}^{l'_1}\sum_{l''_1m''_1} w^{P*}_{l''_1m''_1}\int d\Omega_{\hat{q}} Y^{*}_{l''_1m''_1}(\hat{q})D^{l'_1}_{m'_1M_1}(\hat{q},\rho(\hat{q}))b^{E}_{l'_1M_1} \\ &\times \; [a^{E*}_{l'_1m'_1}(\,{}_{2}Y_{lm}(\hat{q}) + {}_{-2}Y_{lm}(\hat{q})) + ia^{B*}_{l'_1m'_1}(\,{}_{2}Y_{lm}(\hat{q}) - {}_{-2}Y_{lm}(\hat{q}))]. \end{aligned} \tag{5.9}$$

From the above relations, we obtain the autocorrelation $\langle\tilde{a}^{E}_{lm}\tilde{a}^{E*}_{lm}\rangle$ of the multipole coefficients from which we construct the pseudo-C_l estimator for Gaussian fluctuations. The expectation value of the power spectrum is obtained from the estimator, and the coupling matrices that relate this observed power spectrum to the true one correspond to the bias matrices that will be the subject of the next section.

5.3 The bias matrices

In the absence of systematics the power spectrum of the E-component of the polarized radiation field is defined by

$$C^{EE}_{l} = \frac{1}{2l+1}\sum_{m=-l}^{l} a^{E}_{lm}a^{E*}_{lm}. \tag{5.10}$$

This is the true power spectrum corresponding to an ideal systematics-free CMB experiment. We correct the bias of this estimator by introducing the beam smoothing effects and cut-sky described by the autocorrelation $\langle\tilde{a}^{E}_{lm}\tilde{a}^{E*}_{lm}\rangle$. It is essential to account for the partial sky coverage in polarization experiments since the signals are relatively weak, and even for a full sky survey the foreground contaminants dominate the noise in the Galactic plane [65]. The suppression of the sky pixels dominated by the foreground residuals results in a non-uniform/partial sky coverage. The observed power spectrum is then obtained by taking the statistical average over all realizations, and we can write the unbiased estimator as

$$\langle\tilde{C}^{EE}_{l}\rangle = \frac{1}{2l+1}\sum_{m=-l}^{l}\langle\tilde{a}^{E}_{lm}\tilde{a}^{E*}_{lm}\rangle. \tag{5.11}$$

Using Eq. (5.8) and Eq. (5.9), the expectation value of the power spectrum reads

$$\begin{aligned}
\langle \tilde{C}_l^{EE} \rangle &= \frac{1}{2l+1} \sum_{m=-l}^{l} \sum_{l'm'} \sum_{M=-l'}^{l'} \sum_{l''m''} \sum_{l_1'm_1'} \sum_{M_1=-l_1'}^{l_1'} \sum_{l_1''m_1''} w^P_{l''m''} w^{P*}_{l_1''m_1''} \\
&\times \left[\int d\Omega_{\hat{q}} Y_{l''m''}(\hat{q}) [D^{l'}_{m'M}(\hat{q}, \rho(\hat{q})) b^E_{l'M}]^* \int d\Omega_{\hat{q}} Y^*_{l_1''m_1''}(\hat{q}) D^{l_1'}_{m_1'M_1}(\hat{q}, \rho(\hat{q})) b^E_{l_1'M_1} \langle a^E_{l'm'} a^{E*}_{l_1'm_1'} \rangle \right. \\
&\times ({}_2Y^*_{lm}(\hat{q}) + {}_{-2}Y^*_{lm}(\hat{q}))({}_2Y_{lm}(\hat{q}) + {}_{-2}Y_{lm}(\hat{q})) + \int d\Omega_{\hat{q}} Y_{l''m''}(\hat{q}) [D^{l'}_{m'M}(\hat{q}, \rho(\hat{q})) b^E_{l'M}]^* \\
&\times \left. \int d\Omega_{\hat{q}} Y^*_{l_1''m_1''}(\hat{q}) D^{l_1'}_{m_1'M_1}(\hat{q}, \rho(\hat{q})) b^E_{l_1'M_1} \langle a^B_{l'm'} a^{B*}_{l_1'm_1'} \rangle ({}_2Y^*_{lm}(\hat{q}) - {}_{-2}Y^*_{lm}(\hat{q}))({}_2Y_{lm}(\hat{q}) - {}_{-2}Y_{lm}(\hat{q})) \right],
\end{aligned}$$

where the bilinear correlations between the E and B-mode polarizations are defined by

$$\begin{aligned}
\langle a^E_{l'm'} a^{E*}_{l_1'm_1'} \rangle &= C^{EE}_{l'} \, \delta_{l'l_1'} \delta_{m'm_1'}, \\
\langle a^B_{l'm'} a^{B*}_{l_1'm_1'} \rangle &= C^{BB}_{l'} \, \delta_{l'l_1'} \delta_{m'm_1'}.
\end{aligned} \tag{5.12}$$

The other terms of the correlations vanish as a consequence of the rotational invariance of the random properties of the CMB multipole coefficients a_{lm}. The only non-zero terms in the summations are obtained for $l' = l_1'$ and $m' = m_1'$. These conditions yield

$$\begin{aligned}
\langle \tilde{C}_l^{EE} \rangle &= \frac{1}{2l+1} \sum_{m=-l}^{l} \sum_{l'm'} \sum_{M=-l'}^{l'} \sum_{l''m''} \sum_{M_1=-l_1'}^{l_1'} \sum_{l_1''m_1''} w^P_{l''m''} w^{P*}_{l_1''m_1''} \\
&\times \int d\Omega_{\hat{q}} Y_{l''m''}(\hat{q}) [D^{l'}_{m'M}(\hat{q}, \rho(\hat{q})) b^E_{l'M}]^* \int d\Omega_{\hat{q}} Y^*_{l_1''m_1''}(\hat{q}) D^{l_1'}_{m_1'M_1}(\hat{q}, \rho(\hat{q})) b^E_{l_1'M_1} \\
&\times \left[C^{EE}_{l'} ({}_2Y^*_{lm}(\hat{q}) + {}_{-2}Y^*_{lm}(\hat{q}))({}_2Y_{lm}(\hat{q}) + {}_{-2}Y_{lm}(\hat{q})) \right. \\
&+ \left. C^{BB}_{l'} ({}_2Y^*_{lm}(\hat{q}) - {}_{-2}Y^*_{lm}(\hat{q}))({}_2Y_{lm}(\hat{q}) - {}_{-2}Y_{lm}(\hat{q})) \right].
\end{aligned} \tag{5.13}$$

As we can see from Eq. (5.13), the observed spectrum $\langle \tilde{C}_l^{EE} \rangle$ depends on the angular power spectrum of the B-mode. As we have outlined in this chapter, the standard pseudo-C_l that we have defined here is mixing the E and B-modes in the sense that in the absence of E-mode the power spectrum of the E-mode polarization is non-zero (B-mode leaking to E); and in absence of B-mode polarization $C^{BB}_{l'} \neq 0$ (E-mode leaking to B). For the estimation of the EE power spectrum, we ignore this aspect of the estimator leaving for future prospect the utilization of the "pure" pseudo-C_l method.

Now, we decompose the expected power spectrum $\langle \tilde{C}_l^{EE} \rangle$ into two terms containing two matrices $A^{EE}_{ll'}$ and $A^{BB}_{ll'}$ that we derive next. For brevity, we adopt the following notations of the bias matrices

throughout this chapter:

$$A^{EE}_{ll'} = A^{E}_{ll'}, \tag{5.14}$$

$$A^{BB}_{ll'} = A^{B}_{ll'}. \tag{5.15}$$

We may write Eq. (5.13) as

$$\langle \tilde{C}^{EE}_{l} \rangle = \sum_{l'} A^{E}_{ll'} C^{EE}_{l'} + \sum_{l'} A^{B}_{ll'} C^{BB}_{l'}, \tag{5.16}$$

where the bias matrices $A^{E}_{ll'}$ and $A^{B}_{ll'}$ are defined by

$$\begin{aligned} A^{E}_{ll'} &= \frac{1}{2l+1} \sum_{m=-l}^{l} \sum_{m'=-l'}^{l'} \sum_{M=-l'}^{l'} \sum_{l''m''} \sum_{M_1=-l'}^{l'} \sum_{l''_1 m''_1} w^{P}_{l''m''} w^{P*}_{l''_1 m''_1} b^{E}_{l'M} b^{E}_{l'M_1} \\ &\times \int d\Omega_{\hat{q}} Y_{l''m''}(\hat{q}) [D^{l'}_{m'M}(\hat{q}, \rho(\hat{q}))]^{*} \int d\Omega_{\hat{q}} Y^{*}_{l''_1 m''_1}(\hat{q}) D^{l'}_{m'M_1}(\hat{q}, \rho(\hat{q})) \\ &\times ({}_2Y^{*}_{lm}(\hat{q}) + {}_{-2}Y^{*}_{lm}(\hat{q}))({}_2Y_{lm}(\hat{q}) + {}_{-2}Y_{lm}(\hat{q})), \end{aligned} \tag{5.17}$$

and

$$\begin{aligned} A^{B}_{ll'} &= \frac{1}{2l+1} \sum_{m=-l}^{l} \sum_{m'=-l'}^{l'} \sum_{M=-l'}^{l'} \sum_{l''m''} \sum_{M_1=-l'}^{l'} \sum_{l''_1 m''_1} w^{P}_{l''m''} w^{P*}_{l''_1 m''_1} b^{E}_{l'M} b^{E}_{l'M_1} \\ &\times \int d\Omega_{\hat{q}} Y_{l''m''}(\hat{q}) [D^{l'}_{m'M}(\hat{q}, \rho(\hat{q}))]^{*} \int d\Omega_{\hat{q}} Y^{*}_{l''_1 m''_1}(\hat{q}) D^{l'}_{m'M_1}(\hat{q}, \rho(\hat{q})) \\ &\times ({}_2Y^{*}_{lm}(\hat{q}) - {}_{-2}Y^{*}_{lm}(\hat{q}))({}_2Y_{lm}(\hat{q}) - {}_{-2}Y_{lm}(\hat{q})). \end{aligned} \tag{5.18}$$

The bias matrices $A^{E}_{ll'}$ and $A^{B}_{ll'}$ relate the true power spectra $C^{EE}_{l'}$ and $C^{BB}_{l'}$ to the observed power spectrum $\langle \tilde{C}^{EE}_{l} \rangle$. The theoretical values of the power spectra are obtained from the best fit fiducial model computed by the CAMB software. In the following sections, we derive the analytical forms of the bias matrices $A^{E}_{ll'}$ and $A^{B}_{ll'}$, then reduce their expressions by only including the Clebsch-Gordan coefficients and Wigner-d functions, instead of spherical harmonics, in the expression of the bias matrices.

5.4 Calculation of the bias matrix $A^{E}_{ll'}$

In this section, we treat the derivation of the integrals of the spherical harmonic functions and rotation matrices involved in the expression of the bias matrix $A^{E}_{ll'}$. The first step of the calculations

consists to derive the following integral

$$I = \int d\Omega_{\hat{q}} Y_{l''m''}(\hat{q}) [D^{l'}_{m'M}(\hat{q}, \rho(\hat{q}))]^*. \tag{5.19}$$

The complex conjugate of the integral I reads

$$I^* = \int d\Omega_{\hat{q}} Y^*_{l''m''}(\hat{q}) [D^{l'}_{m'M}(\hat{q}, \rho(\hat{q}))]. \tag{5.20}$$

We use Eq. (1), Section 4.17 of [146] and write

$$Y^*_{l''m''}(\hat{q}) = \sqrt{\frac{2l''+1}{4\pi}} D^{l''}_{m''0}(\hat{q}, \rho(\hat{q})), \tag{5.21}$$

and the integral I^* can be expressed as

$$I^* = \sqrt{\frac{2l''+1}{4\pi}} \int d\Omega_{\hat{q}} D^{l''}_{m''0}(\hat{q}, \rho(\hat{q})) D^{l'}_{m'M}(\hat{q}, \rho(\hat{q})). \tag{5.22}$$

The product of two Wigner-D rotation matrices can be expanded and expressed in terms of Clebsch-Gordan coefficients using Eq. (1), Section 4.6 of [146], and we get

$$D^{l''}_{m''0}(\hat{q}, \rho(\hat{q})) D^{l'}_{m'M}(\hat{q}, \rho(\hat{q})) = \sum_{L=|l''-l'|}^{l''+l'} C^{L(m''+m')}_{l''m''l'm'} D^{L}_{(m''+m')M}(\hat{q}, \rho(\hat{q})) C^{LM}_{l''0l'M}, \tag{5.23}$$

that yields

$$I^* = \sqrt{\frac{2l''+1}{4\pi}} \sum_{L=|l''-l'|}^{l''+l'} C^{L(m''+m')}_{l''m''l'm'} C^{LM}_{l''0l'M} \int d\Omega_{\hat{q}} D^{L}_{(m''+m')M}(\hat{q}, \rho(\hat{q})). \tag{5.24}$$

As we have seen in Eq. (E.9), for an equal declination scan $\rho(\hat{q}) = \rho(\theta)$; the last integral in the above equation vanishes unless $m'' + m' = 0$, and the integral I^* reduces to

$$I^* = \sqrt{\frac{2l''+1}{4\pi}} \sum_{L=|l''-l'|}^{l''+l'} C^{L0}_{l''-m'l'm'} C^{LM}_{l''0l'M} \; \chi^{L}_{0M}[\rho(\hat{q})]. \tag{5.25}$$

The second step of the calculation of the bias matrix $A^E_{ll'}$ consists to derive the following integral

$$\begin{aligned} J &= \int d\Omega_{\hat{q}} Y^*_{l''_1 m''_1}(\hat{q}) D^{l'}_{m'M_1}(\hat{q}, \rho(\hat{q})) \\ &\times ({}_2Y^*_{lm}(\hat{q}) + {}_{-2}Y^*_{lm}(\hat{q}))({}_2Y_{lm}(\hat{q}) + {}_{-2}Y_{lm}(\hat{q})), \end{aligned} \tag{5.26}$$

which is reported to the following section.

5.5 Calculation of the integral J

In this section, we present the derivation of the integral J involved in the calculation of the bias matrix $A^E_{ll'}$. We write the integral J in the following form

$$\begin{aligned} J &= \int d\Omega_{\hat{q}} Y^*_{l''_1 m''_1}(\hat{q}) D^{l'}_{m' M_1}(\hat{q}, \rho(\hat{q})) \\ &\times \; (\, {}_2Y^*_{lm}(\hat{q}) \; {}_2Y_{lm}(\hat{q}) + {}_2 \, Y^*_{lm}(\hat{q}) \; {}_{-2}Y_{lm}(\hat{q}) \\ &+ \quad {}_{-2}Y^*_{lm}(\hat{q}) \; {}_2Y_{lm}(\hat{q}) + {}_{-2} \, Y^*_{lm}(\hat{q}) \; {}_{-2}Y_{lm}(\hat{q})). \end{aligned} \tag{5.27}$$

We can decompose the integral J into the sum of two integrals and then, calculate each integral involved in the summation. First, we calculate the following integral

$$J_1 = \int d\Omega_{\hat{q}} Y^*_{l''_1 m''_1}(\hat{q}) D^{l'}_{m' M_1}(\hat{q}, \rho(\hat{q})) \; {}_2Y^*_{lm}(\hat{q}) \; {}_2Y_{lm}(\hat{q}). \tag{5.28}$$

From Eq. (1), Section 4.17 of [146] we have

$$Y^*_{l''_1 m''_1}(\hat{q}) = \sqrt{\frac{2l''_1 + 1}{4\pi}} D^{l''_1}_{m''_1 0}(\hat{q}, \rho(\hat{q})), \tag{5.29}$$

and may write

$$Y^*_{l''_1 m''_1}(\hat{q}) D^{l'}_{m' M_1}(\hat{q}, \rho(\hat{q})) = \sqrt{\frac{2l''_1 + 1}{4\pi}} D^{l''_1}_{m''_1 0}(\hat{q}, \rho(\hat{q})) D^{l'}_{m' M_1}(\hat{q}, \rho(\hat{q})), \tag{5.30}$$

which after the insertion of the Clebsch-Gordan series yields

$$Y^*_{l''_1 m''_1}(\hat{q}) D^{l'}_{m' M_1}(\hat{q}, \rho(\hat{q})) = \sqrt{\frac{2l''_1 + 1}{4\pi}} \sum_{L=|l''_1 - l'|}^{l''_1 + l'} C^{L(m''_1 + m')}_{l''_1 m''_1 l' m'} D^L_{(m''_1 + m') M_1}(\hat{q}, \rho(\hat{q})) C^{L M_1}_{l''_1 0 l' M_1}. \tag{5.31}$$

Then, we calculate the product of the spin-2 spherical harmonics. From Eq. (3.3) of [147] we may write the following relation

$${}_2Y_{lm}(\hat{q}) = (-1)^m \, {}_{-2}Y^*_{l-m}(\hat{q}) \tag{5.32}$$

that we combine with Eq. (3.11) of [125]

$$ {}_2Y_{lm}(\hat{q}) = (-1)^m \sqrt{\frac{2l+1}{4\pi}} D^l_{-m2}(\hat{q}, \rho(\hat{q})), \tag{5.33} $$

in order to derive the following relation

$$ {}_2Y^*_{lm}(\hat{q})\ {}_2Y_{lm}(\hat{q}) = \sqrt{\frac{2l+1}{4\pi}} D^l_{-m2}(\hat{q}, \rho(\hat{q}))(-1)^m \sqrt{\frac{2l+1}{4\pi}} D^l_{-m2}(\hat{q}, \rho(\hat{q})). \tag{5.34} $$

We replace the product of the Wigner-D matrices by their Clebsch expansions using Eq. (1) of Section 4.6 of [146] and get

$$ {}_2Y^*_{lm}(\hat{q})\ {}_2Y_{lm}(\hat{q}) = \frac{2l+1}{4\pi}(-1)^m \sum_{L'=0}^{2l} C^{L'0}_{lml-m} D^{L'}_{00}(\hat{q}, \rho(\hat{q})) C^{L'0}_{l-2l2}. \tag{5.35} $$

Furthermore, we repeat the expansion of the product of Wigner-D functions using Eq. (1) of Section 4.6 of [146] and write

$$ D^L_{(m''_1+m')M_1}(\hat{q}, \rho(\hat{q})) D^{L'}_{00}(\hat{q}, \rho(\hat{q})) = \sum_{L''=|L-L'|}^{L+L'} C^{L''(m''_1+m')}_{L(m''_1+m')L'0} D^{L''}_{(m''_1+m')M_1}(\hat{q}, \rho(\hat{q})) C^{L''M_1}_{LM_1L'0}, \tag{5.36} $$

and plugging this in Eq. (5.28) yields the following expression of the integral

$$ \begin{aligned} J_1 &= \sqrt{\frac{2l''_1+1}{4\pi}} \sum_{L=|l''_1-l'|}^{l''_1+l'} C^{L(m''_1+m')}_{l''_1m''_1l'm'} C^{LM_1}_{l''_10l'M_1} \frac{2l+1}{4\pi}(-1)^m \sum_{L'=0}^{2l} C^{L'0}_{lml-m} C^{L'0}_{l-2l2} \\ &\times \sum_{L''=|L-L'|}^{L+L'} C^{L''(m''_1+m')}_{L(m''_1+m')L'0} C^{L''M_1}_{LM_1L'0} \int d\Omega_{\hat{q}} D^{L''}_{(m''_1+m')M_1}(\hat{q}, \rho(\hat{q})). \end{aligned} \tag{5.37} $$

Thereafter, we calculate the following integral

$$ J_2 = \int d\Omega_{\hat{q}} Y^*_{l''_1m''_1}(\hat{q}) D^{l'}_{m'M_1}(\hat{q}, \rho(\hat{q}))\ {}_2Y^*_{lm}(\hat{q})\ {}_{-2}Y_{lm}(\hat{q}), \tag{5.38} $$

which can be derived by repeating the previous steps. We combine Eq. (3.3) of [147] and Eq. (3.11) of [125] to derive

$$ {}_2Y^*_{lm}(\hat{q})\ {}_{-2}Y_{lm}(\hat{q}) = \sqrt{\frac{2l+1}{4\pi}} D^l_{m-2}(\hat{q}, \rho(\hat{q}))(-1)^m \sqrt{\frac{2l+1}{4\pi}} D^l_{-m-2}(\hat{q}, \rho(\hat{q})), \tag{5.39} $$

which after the expansion of the Wigner-D matrices as in Eq. (1), Section 4.6 of [146] reduces to

$$ {}_2Y^*_{lm}(\hat{q})\ {}_2Y_{lm}(\hat{q}) = \frac{2l+1}{4\pi}(-1)^m \sum_{L'=0}^{2l} C^{L'0}_{lml-m} D^{L'}_{0-4}(\hat{q},\rho(\hat{q})) C^{L'-4}_{l-2l-2}. \tag{5.40} $$

The Clebsch-Gordan series of Eq. (1), Section 4.6 of [146] imply the following relation

$$ D^{L}_{(m''_1+m')M_1}(\hat{q},\rho(\hat{q})) D^{L'}_{0-4}(\hat{q},\rho(\hat{q})) = \sum_{L''=|L-L'|}^{L+L'} C^{L''(m''_1+m')}_{L(m''_1+m')L'0} D^{L''}_{(m''_1+m')(M_1-4)}(\hat{q},\rho(\hat{q})) C^{L''(M_1-4)}_{LM_1L'-4}, $$

which replaced in the integral of Eq. (5.38) gives the following relation

$$ \begin{aligned} J_2 &= \sqrt{\frac{2l''_1+1}{4\pi}} \sum_{L=|l''_1-l'|}^{l''_1+l'} C^{L(m''_1+m')}_{l''_1m''_1l'm'} C^{LM_1}_{l''_10l'M_1} \frac{2l+1}{4\pi}(-1)^m \sum_{L'=0}^{2l} C^{L'0}_{lml-m} C^{L'-4}_{l-2l-2} \\ &\times \sum_{L''=|L-L'|}^{L+L'} C^{L''(m''_1+m')}_{L(m''_1+m')L'0} C^{L''(M_1-4)}_{LM_1L'-4} \int d\Omega_{\hat{q}} D^{L''}_{(m''_1+m')(M_1-4)}(\hat{q},\rho(\hat{q})). \end{aligned} \tag{5.41} $$

Similarly, we derive the next integral

$$ J_3 = \int d\Omega_{\hat{q}} Y^*_{l''_1m''_1}(\hat{q}) D^{l'}_{m'M_1}(\hat{q},\rho(\hat{q}))\ {}_{-2}Y^*_{lm}(\hat{q})\ {}_2Y_{lm}(\hat{q}), \tag{5.42} $$

by using the same steps and relations that link the spin-2 spherical harmonics to the Wigner-D matrices and Clebsch-Gordan series. Then, we obtain the following expressions

$$ \begin{aligned} {}_{-2}Y^*_{lm}(\hat{q})\ {}_2Y_{lm}(\hat{q}) &= \sqrt{\frac{2l+1}{4\pi}} D^{l}_{m2}(\hat{q},\rho(\hat{q}))(-1)^m \sqrt{\frac{2l+1}{4\pi}} D^{l}_{-m2}(\hat{q},\rho(\hat{q})), \\ &= \frac{2l+1}{4\pi}(-1)^m \sum_{L'=0}^{2l} C^{L'0}_{lml-m} D^{L'}_{04}(\hat{q},\rho(\hat{q})) C^{L'4}_{l2l2}, \end{aligned} \tag{5.43} $$

and

$$ D^{L}_{(m''_1+m')M_1}(\hat{q},\rho(\hat{q})) D^{L'}_{04}(\hat{q},\rho(\hat{q})) = \sum_{L''=|L-L'|}^{L+L'} C^{L''(m''_1+m')}_{L(m''_1+m')L'0} D^{L''}_{(m''_1+m')(M_1+4)}(\hat{q},\rho(\hat{q})) C^{L''(M_1+4)}_{LM_1L'4}, $$

from which we get

$$J_3 = \sqrt{\frac{2l_1''+1}{4\pi}} \sum_{L=|l_1''-l'|}^{l_1''+l'} C^{L(m_1''+m')}_{l_1''m_1''l'm'} C^{LM_1}_{l_1''0l'M_1} \frac{2l+1}{4\pi}(-1)^m \sum_{L'=0}^{2l} C^{L'0}_{lml-m} C^{L'4}_{l2l2}$$
$$\times \sum_{L''=|L-L'|}^{L+L'} C^{L''(m_1''+m')}_{L(m_1''+m')L'0} C^{L''(M_1+4)}_{LM_1L'4} \int d\Omega_{\hat{q}} D^{L''}_{(m_1''+m')(M_1+4)}(\hat{q},\rho(\hat{q})). \quad (5.44)$$

We similarly proceed as above for the derivation of the last integral

$$J_4 = \int d\Omega_{\hat{q}} Y^*_{l_1''m_1''}(\hat{q}) D^{l'}_{m'M_1}(\hat{q},\rho(\hat{q}))\ {}_{-2}Y^*_{lm}(\hat{q})\ {}_{-2}Y_{lm}(\hat{q}), \quad (5.45)$$

and obtain the following relations

$$\begin{aligned} {}_{-2}Y^*_{lm}(\hat{q})\ {}_{-2}Y_{lm}(\hat{q}) &= \sqrt{\frac{2l+1}{4\pi}} D^l_{m2}(\hat{q},\rho(\hat{q}))(-1)^m \sqrt{\frac{2l+1}{4\pi}} D^l_{-m-2}(\hat{q},\rho(\hat{q})), \\ &= \frac{2l+1}{4\pi}(-1)^m \sum_{L'=0}^{2l} C^{L'0}_{lml-m} D^{L'}_{00}(\hat{q},\rho(\hat{q})) C^{L'0}_{l2l-2}, \end{aligned} \quad (5.46)$$

and

$$D^L_{(m_1''+m')M_1}(\hat{q},\rho(\hat{q})) D^{L'}_{00}(\hat{q},\rho(\hat{q})) = \sum_{L''=|L-L'|}^{L+L'} C^{L''(m_1''+m')}_{L(m_1''+m')L'0} D^{L''}_{(m_1''+m')M_1}(\hat{q},\rho(\hat{q})) C^{L''M_1}_{LM_1L'0},$$

which yield the following expression

$$J_4 = \sqrt{\frac{2l_1''+1}{4\pi}} \sum_{L=|l_1''-l'|}^{l_1''+l'} C^{L(m_1''+m')}_{l_1''m_1''l'm'} C^{LM_1}_{l_1''0l'M_1} \frac{2l+1}{4\pi}(-1)^m \sum_{L'=0}^{2l} C^{L'0}_{lml-m} C^{L'0}_{l2l-2}$$
$$\times \sum_{L''=|L-L'|}^{L+L'} C^{L''(m_1''+m')}_{L(m_1''+m')L'0} C^{L''M_1}_{LM_1L'0} \int d\Omega_{\hat{q}} D^{L''}_{(m_1''+m')M_1}(\hat{q},\rho(\hat{q})). \quad (5.47)$$

Then, we obtain the integral $J = J_1 + J_2 + J_3 + J_4$. If we assume an equal declination scan strategies $\rho(\hat{q}) = \rho(\theta)$ of the CMB polarimetry experiment, we can write according to Eq. (E.9) of the appendix the following relation

$$\chi^{L''}_{(m_1''+m')M_1}[\rho(\theta)] \equiv \int d\Omega_{\hat{q}} D^{L''}_{(m_1''+m')M_1}(\hat{q},\rho(\hat{q})) = \chi^{L''}_{0M_1}[\rho(\theta)], \quad (5.48)$$

and for the particular case of a non-rotating beam $\rho(\hat{q}) = 0$, we can evaluate analytically the function χ, which is defined by $\chi^{L''}_{0M_1}[\rho(\theta)] = 2\pi \sum_{N=-L''}^{L''} d^{L''}_{0N}(\frac{\pi}{2}) d^{L''}_{NM_1}(\frac{\pi}{2}) f_{M_1 N}$. Note that the only non-vanishing term of the integral of the Wigner-D matrix is obtained for $m''_1 + m' = 0$ implying the condition $m''_1 = -m'$. Thus, the integral J reduces to

$$
\begin{aligned}
J &= \sqrt{\frac{2l''_1+1}{4\pi}} \sum_{L=|l''_1-l'|}^{l''_1+l'} C^{L(m''_1+m')}_{l''_1 m''_1 l' m'} C^{LM_1}_{l''_1 0 l' M_1} \frac{2l+1}{4\pi} (-1)^m \sum_{L'=0}^{2l} C^{L'0}_{lml-m} \sum_{L''=|L-L'|}^{L+L'} C^{L''(m''_1+m')}_{L(m''_1+m')L'0} \\
&\times \Big[C^{L'0}_{l-2l2} C^{L''M_1}_{LM_1L'0}\ \chi^{L''}_{0M_1}[\rho(\theta)] + C^{L'-4}_{l-2l-2} C^{L''(M_1-4)}_{LM_1L'-4}\ \chi^{L''}_{0(M_1-4)}[\rho(\theta)] \\
&+ C^{L'4}_{l2l2} C^{L''(M_1+4)}_{LM_1L'4}\ \chi^{L''}_{0(M_1+4)}[\rho(\theta)] + C^{L'0}_{l2l-2} C^{L''M_1}_{LM_1L'0}\ \chi^{L''}_{0M_1}[\rho(\theta)] \Big]. \qquad (5.49)
\end{aligned}
$$

Finally, using the relation $C^{L'0}_{l-2l2} = (-1)^{L'} C^{L'0}_{l2l-2}$ from Eq. (11), Section 8.4.3 of [146], and replacing the function χ we get

$$
\begin{aligned}
J &= \sqrt{\frac{2l''_1+1}{4\pi}} \sum_{L=|l''_1-l'|}^{l''_1+l'} C^{L(m''_1+m')}_{l''_1 m''_1 l' m'} C^{LM_1}_{l''_1 0 l' M_1} \frac{2l+1}{4\pi} (-1)^m \sum_{L'=0}^{2l} C^{L'0}_{lml-m} \sum_{L''=|L-L'|}^{L+L'} C^{L''(m''_1+m')}_{L(m''_1+m')L'0} \\
&\times \Big[((-1)^{L'}+1) C^{L'0}_{l2l-2} C^{L''M_1}_{LM_1L'0}\ \chi^{L''}_{0M_1}[\rho(\theta)] + C^{L'-4}_{l-2l-2} C^{L''(M_1-4)}_{LM_1L'-4}\ \chi^{L''}_{0(M_1-4)}[\rho(\theta)] \\
&+ C^{L'4}_{l2l2} C^{L''(M_1+4)}_{LM_1L'4}\ \chi^{L''}_{0(M_1+4)}[\rho(\theta)] \Big], \\
&= \sqrt{\frac{2l''_1+1}{4\pi}} \sum_{L=|l''_1-l'|}^{l''_1+l'} C^{L(m''_1+m')}_{l''_1 m''_1 l' m'} C^{LM_1}_{l''_1 0 l' M_1} \frac{2l+1}{4\pi} (-1)^m \sum_{L'=0}^{2l} C^{L'0}_{lml-m} \sum_{L''=|L-L'|}^{L+L'} C^{L''(m''_1+m')}_{L(m''_1+m')L'0} \\
&\times \Bigg[((-1)^{L'}+1) C^{L'0}_{l2l-2} C^{L''M_1}_{LM_1L'0}\ 2\pi \sum_{N=-L''}^{L''} d^{L''}_{0N}(\frac{\pi}{2}) d^{L''}_{NM_1}(\frac{\pi}{2}) f_{M_1 N} \\
&+ C^{L'-4}_{l-2l-2} C^{L''(M_1-4)}_{LM_1L'-4}\ 2\pi \sum_{N=-L''}^{L''} d^{L''}_{0N}(\frac{\pi}{2}) d^{L''}_{N(M_1-4)}(\frac{\pi}{2}) f_{(M_1-4)N} \\
&+ C^{L'4}_{l2l2} C^{L''(M_1+4)}_{LM_1L'4}\ 2\pi \sum_{N=-L''}^{L''} d^{L''}_{0N}(\frac{\pi}{2}) d^{L''}_{N(M_1+4)}(\frac{\pi}{2}) f_{(M_1+4)N} \Bigg]. \qquad (5.50)
\end{aligned}
$$

The non-rotating beam assumption implies that the integral I is real so that $I^* = I$. Then, we may write the form of the bias matrix $A^E_{ll'}$ as follows

$$
A^E_{ll'} = \frac{1}{2l+1} \sum_{m=-l}^{l} \sum_{m'=-l'}^{l'} \sum_{M=-l'}^{l'} \sum_{l''m''} \sum_{M_1=-l'}^{l'} \sum_{l''_1 m''_1} w^P_{l''m''} w^{P*}_{l''_1 m''_1} b^E_{l'M} b^E_{l'M_1}\ I \times J. \qquad (5.51)
$$

Replacing the integrals I and J by their expressions, we get

$$
\begin{aligned}
A^E_{ll'} &= \frac{1}{2l+1}\sum_{m=-l}^{l}\sum_{m'=-l'}^{l'}\sum_{M=-l'}^{l'}\sum_{l''m''}\sum_{M_1=-l'}^{l'}\sum_{l''_1m''_1} w^P_{l''m''}w^{P*}_{l''_1m''_1}b^E_{l'M}b^E_{l'M_1}\\
&\times \sqrt{\frac{2l''+1}{4\pi}}\sum_{L=|l''-l'|}^{l''+l'} C^{L0}_{l''-m'l'm'}C^{LM}_{l''0l'M}\ 2\pi\sum_{N=-L}^{L} d^L_{0N}(\frac{\pi}{2})d^L_{NM}(\frac{\pi}{2})f_{MN}\\
&\times \sqrt{\frac{2l''_1+1}{4\pi}}\sum_{L=|l''_1-l'|}^{l''_1+l'} C^{L(m''_1+m')}_{l''_1m''_1l'm'}C^{LM_1}_{l''_10l'M_1}\frac{2l+1}{4\pi}(-1)^m\sum_{L'=0}^{2l} C^{L'0}_{lml-m}\sum_{L''=|L-L'|}^{L+L'} C^{L''(m''_1+m')}_{L(m''_1+m')L'0}\\
&\times \Bigg[((-1)^{L'}+1)C^{L'0}_{l2l-2}C^{L''M_1}_{LM_1L'0}\ 2\pi\sum_{N=-L''}^{L''} d^{L''}_{0N}(\frac{\pi}{2})d^{L''}_{NM_1}(\frac{\pi}{2})f_{M_1N}\\
&+ C^{L'-4}_{l-2l-2}C^{L''(M_1-4)}_{LM_1L'-4}\ 2\pi\sum_{N=-L''}^{L''} d^{L''}_{0N}(\frac{\pi}{2})d^{L''}_{N(M_1-4)}(\frac{\pi}{2})f_{(M_1-4)N}\\
&+ C^{L'4}_{l2l2}C^{L''(M_1+4)}_{LM_1L'4}\ 2\pi\sum_{N=-L''}^{L''} d^{L''}_{0N}(\frac{\pi}{2})d^{L''}_{N(M_1+4)}(\frac{\pi}{2})f_{(M_1+4)N}\Bigg], \qquad (5.52)
\end{aligned}
$$

which after simplification reduces to the following form

$$
\begin{aligned}
A^E_{ll'} &= \frac{1}{4}\sum_{m=-l}^{l}\sum_{m'=-l'}^{l'}\sum_{M=-l'}^{l'}\sum_{M_1=-l'}^{l'}\sum_{l''=0}^{l''_{max}}\sum_{l''_1=0}^{l''_{1max}}(-1)^m\sqrt{(2l''+1)(2l''_1+1)}w^P_{l''-m'}w^{P*}_{l''_1-m'}b^E_{l'M}b^E_{l'M_1}\\
&\times \sum_{L=|l''-l'|}^{l''+l'} C^{L0}_{l''-m'l'm'}C^{LM}_{l''0l'M}\sum_{N=-L}^{L} d^L_{0N}(\frac{\pi}{2})d^L_{NM}(\frac{\pi}{2})f_{MN}\\
&\times \sum_{L=|l''_1-l'|}^{l''_1+l'} C^{L0}_{l''_1-m'l'm'}C^{LM_1}_{l''_10l'M_1}\sum_{L'=0}^{2l} C^{L'0}_{lml-m}\sum_{L''=|L-L'|}^{L+L'} C^{L''0}_{L0L'0}\\
&\times \Bigg[((-1)^{L'}+1)C^{L'0}_{l2l-2}C^{L''M_1}_{LM_1L'0}\sum_{N=-L''}^{L''} d^{L''}_{0N}(\frac{\pi}{2})d^{L''}_{NM_1}(\frac{\pi}{2})f_{M_1N}\\
&+ C^{L'-4}_{l-2l-2}C^{L''(M_1-4)}_{LM_1L'-4}\sum_{N=-L''}^{L''} d^{L''}_{0N}(\frac{\pi}{2})d^{L''}_{N(M_1-4)}(\frac{\pi}{2})f_{(M_1-4)N}\\
&+ C^{L'4}_{l2l2}C^{L''(M_1+4)}_{LM_1L'4}\sum_{N=-L''}^{L''} d^{L''}_{0N}(\frac{\pi}{2})d^{L''}_{N(M_1+4)}(\frac{\pi}{2})f_{(M_1+4)N}\Bigg]. \qquad (5.53)
\end{aligned}
$$

In this formula, l''_{max} and l''_{1max} are the cut-off at the multipole l of the polarization mask. The expansions of the beam harmonic transforms are limited to the multipoles $M,\ M_1 = \pm 2,\ \pm 4,\ \pm 6$, as we have used the same model of simulated beam as that adopted in Chapter 3.

5.6 Calculation of the bias matrix $A^B_{ll'}$

We derive in this section the bias $A^B_{ll'}$ which results from the B-mode contribution to the EE bias matrix. We note that the bias matrix $A^B_{ll'}$ calculations involve the same integrals as those ones $(J_1,\ J_2,\ J_3,\ J_4)$ derived in the previous section, except some changes in the integrals sign. The bias matrix $A^B_{ll'}$ can be written as follows

$$\begin{aligned} A^B_{ll'} &= \frac{1}{2l+1}\sum_{m=-l}^{l}\sum_{m'=-l'}^{l'}\sum_{M=-l'}^{l'}\sum_{l''m''}\sum_{M_1=-l'}^{l'}\sum_{l''_1 m''_1} w^P_{l''m''} w^{P*}_{l''_1 m''_1} b^E_{l'M} b^E_{l'M_1} \\ &\times \int d\Omega_{\hat{q}} Y_{l''m''}(\hat{q})[D^{l'}_{m'M}(\hat{q},\rho(\hat{q}))]^* \int d\Omega_{\hat{q}} Y^*_{l''_1 m''_1}(\hat{q}) D^{l'}_{m'M_1}(\hat{q},\rho(\hat{q})) \\ &\times ({}_2Y^*_{lm}(\hat{q}) - {}_{-2}Y^*_{lm}(\hat{q}))({}_2Y_{lm}(\hat{q}) - {}_{-2}Y_{lm}(\hat{q})), \\ &= \frac{1}{2l+1}\sum_{m=-l}^{l}\sum_{m'=-l'}^{l'}\sum_{M=-l'}^{l'}\sum_{l''m''}\sum_{M_1=-l'}^{l'}\sum_{l''_1 m''_1} w^P_{l''m''} w^{P*}_{l''_1 m''_1} b^E_{l'M} b^E_{l'M_1}\ I \times K, \end{aligned} \tag{5.54}$$

where K is defined by

$$\begin{aligned} K &= \int d\Omega_{\hat{q}} Y^*_{l''_1 m''_1}(\hat{q}) D^{l'}_{m'M_1}(\hat{q},\rho(\hat{q})) \\ &\times ({}_2Y^*_{lm}(\hat{q}) - {}_{-2}Y^*_{lm}(\hat{q}))({}_2Y_{lm}(\hat{q}) - {}_{-2}Y_{lm}(\hat{q})). \end{aligned} \tag{5.55}$$

The integral I has been already previously derived, then we only need to find the integral K which can be written as $K = J_1 - J_2 - J_3 + J_4$. Obviously, we can see that the integral K can be obtained directly from the integral $J = J_1 + J_2 + J_3 + J_4$ by putting the negative sign in front of the integrals

J_2 and J_3. Therefore, under the non-rotating beam condition, the bias matrix $A^B_{ll'}$ reads

$$
\begin{aligned}
A^B_{ll'} &= \frac{1}{4}\sum_{m=-l}^{l}\sum_{m'=-l'}^{l'}\sum_{M=-l'}^{l'}\sum_{M_1=-l'}^{l'}\sum_{l''=0}^{l''_{max}}\sum_{l''_1=0}^{l''_{1max}}(-1)^m\sqrt{(2l''+1)(2l''_1+1)}w^P_{l''-m'}w^{P*}_{l''_1-m'}b^E_{l'M}b^E_{l'M_1}\\
&\times \sum_{L=|l''-l'|}^{l''+l'}C^{L0}_{l''-m'l'm'}C^{LM}_{l''0l'M}\sum_{N=-L}^{L}d^L_{0N}(\frac{\pi}{2})d^L_{NM}(\frac{\pi}{2})f_{MN}\\
&\times \sum_{L=|l''_1-l'|}^{l''_1+l'}C^{L0}_{l''_1-m'l'm'}C^{LM_1}_{l''_10l'M_1}\sum_{L'=0}^{2l}C^{L'0}_{lml-m}\sum_{L''=|L-L'|}^{L+L'}C^{L''0}_{L0L'0}\\
&\times \Bigg[((-1)^{L'}+1)C^{L'0}_{l2l-2}C^{L''M_1}_{LM_1L'0}\sum_{N=-L''}^{L''}d^{L''}_{0N}(\frac{\pi}{2})d^{L''}_{NM_1}(\frac{\pi}{2})f_{M_1N}\\
&- C^{L'-4}_{l-2l-2}C^{L''(M_1-4)}_{LM_1L'-4}\sum_{N=-L''}^{L''}d^{L''}_{0N}(\frac{\pi}{2})d^{L''}_{N(M_1-4)}(\frac{\pi}{2})f_{(M_1-4)N}\\
&- C^{L'4}_{l2l2}C^{L''(M_1+4)}_{LM_1L'4}\sum_{N=-L''}^{L''}d^{L''}_{0N}(\frac{\pi}{2})d^{L''}_{N(M_1+4)}(\frac{\pi}{2})f_{(M_1+4)N}\Bigg],
\end{aligned}
\tag{5.56}
$$

where as previously mentioned, the beam expansions in harmonic space are limited to the multipoles $M,\ M_1 = \pm 2,\ \pm 4,\ \pm 6$ which provide sufficient accuracy for mildly elliptical beams [66].

Thus, we resume the expectation value of the EE power spectrum with the following formula

$$
\begin{aligned}
\langle \tilde{C}_l^{EE} \rangle &= \frac{1}{4}\sum_{l'}\sum_{m=-l}^{l}\sum_{m'=-l'}^{l'}\sum_{M=-l'}^{l'}\sum_{M_1=-l'}^{l'}\sum_{l''=0}^{l''_{max}}\sum_{l''_1=0}^{l''_{1max}}(-1)^m\sqrt{(2l''+1)(2l''_1+1)}w^P_{l''-m'}w^{P*}_{l''_1-m'}b^E_{l'M}b^E_{l'M_1} \\
&\times \sum_{L=|l''-l'|}^{l''+l'} C^{L0}_{l''-m'l'm'}C^{LM}_{l''0l'M}\sum_{N=-L}^{L} d^L_{0N}(\frac{\pi}{2})d^L_{NM}(\frac{\pi}{2})f_{MN} \\
&\times \sum_{L=|l''_1-l'|}^{l''_1+l'} C^{L0}_{l''_1-m'l'm'}C^{LM_1}_{l''_10l'M_1}\sum_{L'=0}^{2l} C^{L'0}_{lml-m}\sum_{L''=|L-L'|}^{L+L'} C^{L''0}_{L0L'0} \\
&\times \Bigg[((-1)^{L'}+1)C^{L'0}_{l2l-2}C^{L''M_1}_{LM_1L'0}\sum_{N=-L''}^{L''} d^{L''}_{0N}(\frac{\pi}{2})d^{L''}_{NM_1}(\frac{\pi}{2})f_{M_1N} \\
&+ C^{L'-4}_{l-2l-2}C^{L''(M_1-4)}_{LM_1L'-4}\sum_{N=-L''}^{L''} d^{L''}_{0N}(\frac{\pi}{2})d^{L''}_{N(M_1-4)}(\frac{\pi}{2})f_{(M_1-4)N} \\
&+ C^{L'4}_{l2l2}C^{L''(M_1+4)}_{LM_1L'4}\sum_{N=-L''}^{L''} d^{L''}_{0N}(\frac{\pi}{2})d^{L''}_{N(M_1+4)}(\frac{\pi}{2})f_{(M_1+4)N}\Bigg] C^{EE}_{l'} \\
&+ \frac{1}{4}\sum_{l'}\sum_{m=-l}^{l}\sum_{m'=-l'}^{l'}\sum_{M=-l'}^{l'}\sum_{M_1=-l'}^{l'}\sum_{l''=0}^{l''_{max}}\sum_{l''_1=0}^{l''_{1max}}(-1)^m\sqrt{(2l''+1)(2l''_1+1)}w^P_{l''-m'}w^{P*}_{l''_1-m'}b^E_{l'M}b^E_{l'M_1} \\
&\times \sum_{L=|l''-l'|}^{l''+l'} C^{L0}_{l''-m'l'm'}C^{LM}_{l''0l'M}\sum_{N=-L}^{L} d^L_{0N}(\frac{\pi}{2})d^L_{NM}(\frac{\pi}{2})f_{MN} \\
&\times \sum_{L=|l''_1-l'|}^{l''_1+l'} C^{L0}_{l''_1-m'l'm'}C^{LM_1}_{l''_10l'M_1}\sum_{L'=0}^{2l} C^{L'0}_{lml-m}\sum_{L''=|L-L'|}^{L+L'} C^{L''0}_{L0L'0} \\
&\times \Bigg[((-1)^{L'}+1)C^{L'0}_{l2l-2}C^{L''M_1}_{LM_1L'0}\sum_{N=-L''}^{L''} d^{L''}_{0N}(\frac{\pi}{2})d^{L''}_{NM_1}(\frac{\pi}{2})f_{M_1N} \\
&- C^{L'-4}_{l-2l-2}C^{L''(M_1-4)}_{LM_1L'-4}\sum_{N=-L''}^{L''} d^{L''}_{0N}(\frac{\pi}{2})d^{L''}_{N(M_1-4)}(\frac{\pi}{2})f_{(M_1-4)N} \\
&- C^{L'4}_{l2l2}C^{L''(M_1+4)}_{LM_1L'4}\sum_{N=-L''}^{L''} d^{L''}_{0N}(\frac{\pi}{2})d^{L''}_{N(M_1+4)}(\frac{\pi}{2})f_{(M_1+4)N}\Bigg] C^{BB}_{l'},
\end{aligned}
\tag{5.57}
$$

which can be reduced to the following form

$$
\begin{aligned}
\langle \tilde{C}_l^{EE} \rangle &= \frac{1}{4} \sum_{l'} \sum_{m=-l}^{l} \sum_{m'=-l'}^{l'} \sum_{M=-l'}^{l'} \sum_{M_1=-l'}^{l'} \sum_{l''=0}^{l''_{max}} \sum_{l''_1=0}^{l''_{1max}} (-1)^m \sqrt{(2l''+1)(2l''_1+1)} w^P_{l''-m'} w^{P*}_{l''_1-m'} b^E_{l'M} b^E_{l'M_1} \\
&\times \sum_{L=|l''-l'|}^{l''+l'} C^{L0}_{l''-m'l'm'} C^{LM}_{l''0l'M} \sum_{N=-L}^{L} d^L_{0N}(\frac{\pi}{2}) d^L_{NM}(\frac{\pi}{2}) f_{MN} \\
&\times \sum_{L=|l''_1-l'|}^{l''_1+l'} C^{L0}_{l''_1-m'l'm'} C^{LM_1}_{l''_10l'M_1} \sum_{L'=0}^{2l} C^{L'0}_{lml-m} \sum_{L''=|L-L'|}^{L+L'} C^{L''0}_{L0L'0} \\
&\times \Bigg\{ \Bigg[((-1)^{L'}+1) C^{L'0}_{l2l-2} C^{L''M_1}_{LM_1L'0} \sum_{N=-L''}^{L''} d^{L''}_{0N}(\frac{\pi}{2}) d^{L''}_{NM_1}(\frac{\pi}{2}) f_{M_1N} \\
&+ C^{L'-4}_{l-2l-2} C^{L''(M_1-4)}_{LM_1L'-4} \sum_{N=-L''}^{L''} d^{L''}_{0N}(\frac{\pi}{2}) d^{L''}_{N(M_1-4)}(\frac{\pi}{2}) f_{(M_1-4)N} \\
&+ C^{L'4}_{l2l2} C^{L''(M_1+4)}_{LM_1L'4} \sum_{N=-L''}^{L''} d^{L''}_{0N}(\frac{\pi}{2}) d^{L''}_{N(M_1+4)}(\frac{\pi}{2}) f_{(M_1+4)N} \Bigg] C^{EE}_{l'} \\
&+ \Bigg[((-1)^{L'}+1) C^{L'0}_{l2l-2} C^{L''M_1}_{LM_1L'0} \sum_{N=-L''}^{L''} d^{L''}_{0N}(\frac{\pi}{2}) d^{L''}_{NM_1}(\frac{\pi}{2}) f_{M_1N} \\
&- C^{L'-4}_{l-2l-2} C^{L''(M_1-4)}_{LM_1L'-4} \sum_{N=-L''}^{L''} d^{L''}_{0N}(\frac{\pi}{2}) d^{L''}_{N(M_1-4)}(\frac{\pi}{2}) f_{(M_1-4)N} \\
&- C^{L'4}_{l2l2} C^{L''(M_1+4)}_{LM_1L'4} \sum_{N=-L''}^{L''} d^{L''}_{0N}(\frac{\pi}{2}) d^{L''}_{N(M_1+4)}(\frac{\pi}{2}) f_{(M_1+4)N} \Bigg] C^{BB}_{l'} \Bigg\}. \qquad (5.58)
\end{aligned}
$$

Eq. (5.58) represents the final expression of the EE power spectrum of a CMB polarimetry experiment with non-circular beams in the presence of a cut-sky weighted by the polarization mask function. We must not forget that the estimated EE power spectrum obtained in the above calculations contains a leaking B-mode power since for a finite patch of the sky the standard pseudo-C_l estimator is mixing the E and B-mode. This can be interpreted as a leaking power of the B-mode into the E-power spectrum induced by the boundary conditions. Providing the beam harmonic transforms of the model of beam and polarization mask, the bias matrices $A^E_{ll'}$ and $A^B_{ll'}$ are readily computable. Thereafter, we apply these matrices to the true power spectra in accordance with Eq. (5.16) in order to obtain the observed power spectrum of the EE autocorrelation. The true power spectra $C^{EE}_{l'}$ and $C^{BB}_{l'}$ correspond to the simulated best fiducial model computed from CAMB, for a given cosmological model. Note that once the numerical implementation of the Clebsch-Gordan coefficients and Wigner-d functions involved in the bias matrix $A^E_{ll'}$ is done, no further calculation

of those coefficients is needed for the computation of the bias matrix $A^B_{ll'}$. The reason is that the bias matrix $A^B_{ll'}$ can be simply obtained from $A^E_{ll'}$ by changing to the opposite sign the last two terms inside the square brackets (see, Eq. (5.53) and Eq. (5.56)).

5.7 The full sky and non-circular beam limit for EE

The contribution of the variance of the B-mode to the EE power spectrum can be reduced by observing an important fraction of the sky. A full-sky observation is unrealistic for polarimetry experiments, though the observation over an extended area of the sky on small angular scales can reduce to some extent the mean power $C^{BB}_{l'}$. In this case, the weight of the polarization mask $w^P(\hat{q}) \simeq 1$, then we may write the harmonic transforms of the polarization mask as

$$w^P_{l''-m'} = \int d\Omega_{\hat{q}} Y^*_{l''-m'}(\hat{q}) = \sqrt{4\pi}\delta_{l''0}\delta_{m'0}, \tag{5.59}$$

$$w^P_{l''_1-m'} = \int d\Omega_{\hat{q}} Y^*_{l''_1-m'}(\hat{q}) = \sqrt{4\pi}\delta_{l''_10}\delta_{m'0}. \tag{5.60}$$

The only non-vanishing terms of the summations in Eq. (5.53) are obtained for $l'' = l''_1 = m' = 0$ which yield the following expression of the bias matrix $A^E_{ll'}$

$$\begin{aligned}
A^E_{ll'} &= \pi \sum_{m=-l}^{l} \sum_{M=-l'}^{l'} \sum_{M_1=-l'}^{l'} (-1)^m b^E_{l'M} b^E_{l'M_1} \\
&\times C^{l'0}_{00l'0} C^{l'M}_{00l'M} \sum_{N=-l'}^{l'} d^{l'}_{0N}(\frac{\pi}{2}) d^{l'}_{NM}(\frac{\pi}{2}) f_{MN} \\
&\times C^{l'0}_{00l'0} C^{l'M_1}_{00l'M_1} \sum_{L'=0}^{2l} C^{L'0}_{lml-m} \sum_{L''=|l'-L'|}^{l'+L'} C^{L''0}_{l'0L'0} \\
&\times \Bigg[((-1)^{L'}+1) C^{L'0}_{l2l-2} C^{L''M_1}_{l'M_1L'0} \sum_{N=-L''}^{L''} d^{L''}_{0N}(\frac{\pi}{2}) d^{L''}_{NM_1}(\frac{\pi}{2}) f_{M_1N} \\
&+ C^{L'-4}_{l-2l-2} C^{L''(M_1-4)}_{l'M_1L'-4} \sum_{N=-L''}^{L''} d^{L''}_{0N}(\frac{\pi}{2}) d^{L''}_{N(M_1-4)}(\frac{\pi}{2}) f_{(M_1-4)N} \\
&+ C^{L'4}_{l2l2} C^{L''(M_1+4)}_{l'M_1L'4} \sum_{N=-L''}^{L''} d^{L''}_{0N}(\frac{\pi}{2}) d^{L''}_{N(M_1+4)}(\frac{\pi}{2}) f_{(M_1+4)N} \Bigg].
\end{aligned} \tag{5.61}$$

From Eq. (10), Section 8.4.3 and Eq. (2), Section 8.5 of [146], we obtain the following relations

$$C^{l'0}_{00l'0} = C^{l'0}_{l'000} = 1, \tag{5.62}$$

$$C^{l'M}_{00l'M} = C^{l'M}_{l'M00} = 1, \tag{5.63}$$

which plugged in the above equation yield

$$\begin{aligned}
A^E_{ll'} &= \pi \sum_{m=-l}^{l} \sum_{M=-l'}^{l'} \sum_{M_1=-l'}^{l'} (-1)^m b^E_{l'M} b^E_{l'M_1} \\
&\times \sum_{N=-l'}^{l'} d^{l'}_{0N}(\frac{\pi}{2}) d^{l'}_{NM}(\frac{\pi}{2}) f_{MN} \sum_{L'=0}^{2l} C^{L'0}_{lml-m} \sum_{L''=|l'-L'|}^{l'+L'} C^{L''0}_{l'0L'0} \\
&\times \Bigg[((-1)^{L'}+1) C^{L'0}_{l2l-2} C^{L''M_1}_{l'M_1L'0} \sum_{N=-L''}^{L''} d^{L''}_{0N}(\frac{\pi}{2}) d^{L''}_{NM_1}(\frac{\pi}{2}) f_{M_1N} \\
&+ C^{L'-4}_{l-2l-2} C^{L''(M_1-4)}_{l'M_1L'-4} \sum_{N=-L''}^{L''} d^{L''}_{0N}(\frac{\pi}{2}) d^{L''}_{N(M_1-4)}(\frac{\pi}{2}) f_{(M_1-4)N} \\
&+ C^{L'4}_{l2l2} C^{L''(M_1+4)}_{l'M_1L'4} \sum_{N=-L''}^{L''} d^{L''}_{0N}(\frac{\pi}{2}) d^{L''}_{N(M_1+4)}(\frac{\pi}{2}) f_{(M_1+4)N} \Bigg].
\end{aligned} \tag{5.64}$$

The analogue of the bias matrix $A^B_{ll'}$ formula reads

$$\begin{aligned}
A^B_{ll'} &= \pi \sum_{m=-l}^{l} \sum_{M=-l'}^{l'} \sum_{M_1=-l'}^{l'} (-1)^m b^E_{l'M} b^E_{l'M_1} \\
&\times \sum_{N=-l'}^{l'} d^{l'}_{0N}(\frac{\pi}{2}) d^{l'}_{NM}(\frac{\pi}{2}) f_{MN} \sum_{L'=0}^{2l} C^{L'0}_{lml-m} \sum_{L''=|l'-L'|}^{l'+L'} C^{L''0}_{l'0L'0} \\
&\times \Bigg[((-1)^{L'}+1) C^{L'0}_{l2l-2} C^{L''M_1}_{l'M_1L'0} \sum_{N=-L''}^{L''} d^{L''}_{0N}(\frac{\pi}{2}) d^{L''}_{NM_1}(\frac{\pi}{2}) f_{M_1N} \\
&- C^{L'-4}_{l-2l-2} C^{L''(M_1-4)}_{l'M_1L'-4} \sum_{N=-L''}^{L''} d^{L''}_{0N}(\frac{\pi}{2}) d^{L''}_{N(M_1-4)}(\frac{\pi}{2}) f_{(M_1-4)N} \\
&- C^{L'4}_{l2l2} C^{L''(M_1+4)}_{l'M_1L'4} \sum_{N=-L''}^{L''} d^{L''}_{0N}(\frac{\pi}{2}) d^{L''}_{N(M_1+4)}(\frac{\pi}{2}) f_{(M_1+4)N} \Bigg].
\end{aligned} \tag{5.65}$$

Then, we can summarize the expression of the expectation value of the power spectrum $\langle \tilde{C}_l^{EE} \rangle$ as follows

$$
\begin{aligned}
\langle \tilde{C}_l^{EE} \rangle &= \frac{1}{4} \sum_{l'} \sum_{m=-l}^{l} \sum_{m'=-l'}^{l'} \sum_{M=-l'}^{l'} \sum_{M_1=-l'}^{l'} \sum_{l''=0}^{l''_{max}} \sum_{l''_1=0}^{l''_{1max}} (-1)^m \sqrt{(2l''+1)(2l''_1+1)} w^P_{l''-m'} w^{P*}_{l''_1-m'} b^E_{l'M} b^E_{l'M_1} \\
&\times \sum_{L=|l''-l'|}^{l''+l'} C^{L0}_{l''-m'l'm'} C^{LM}_{l''0l'M} \sum_{N=-L}^{L} d^L_{0N}(\frac{\pi}{2}) d^L_{NM}(\frac{\pi}{2}) f_{MN} \\
&\times \sum_{L=|l''_1-l'|}^{l''_1+l'} C^{L0}_{l''_1-m'l'm'} C^{LM_1}_{l''_10l'M_1} \sum_{L'=0}^{2l} C^{L'0}_{lml-m} \sum_{L''=|L-L'|}^{L+L'} C^{L''0}_{L0L'0} \\
&\times \Bigg\{ \Bigg[((-1)^{L'}+1) C^{L'0}_{l2l-2} C^{L''M_1}_{LM_1L'0} \sum_{N=-L''}^{L''} d^{L''}_{0N}(\frac{\pi}{2}) d^{L''}_{NM_1}(\frac{\pi}{2}) f_{M_1N} \\
&+ C^{L'-4}_{l-2l-2} C^{L''(M_1-4)}_{LM_1L'-4} \sum_{N=-L''}^{L''} d^{L''}_{0N}(\frac{\pi}{2}) d^{L''}_{N(M_1-4)}(\frac{\pi}{2}) f_{(M_1-4)N} \\
&+ C^{L'4}_{l2l2} C^{L''(M_1+4)}_{LM_1L'4} \sum_{N=-L''}^{L''} d^{L''}_{0N}(\frac{\pi}{2}) d^{L''}_{N(M_1+4)}(\frac{\pi}{2}) f_{(M_1+4)N} \Bigg] C^{EE}_{l'} \\
&+ \Bigg[((-1)^{L'}+1) C^{L'0}_{l2l-2} C^{L''M_1}_{LM_1L'0} \sum_{N=-L''}^{L''} d^{L''}_{0N}(\frac{\pi}{2}) d^{L''}_{NM_1}(\frac{\pi}{2}) f_{M_1N} \\
&- C^{L'-4}_{l-2l-2} C^{L''(M_1-4)}_{LM_1L'-4} \sum_{N=-L''}^{L''} d^{L''}_{0N}(\frac{\pi}{2}) d^{L''}_{N(M_1-4)}(\frac{\pi}{2}) f_{(M_1-4)N} \\
&- C^{L'4}_{l2l2} C^{L''(M_1+4)}_{LM_1L'4} \sum_{N=-L''}^{L''} d^{L''}_{0N}(\frac{\pi}{2}) d^{L''}_{N(M_1+4)}(\frac{\pi}{2}) f_{(M_1+4)N} \Bigg] C^{BB}_{l'} \Bigg\}. \qquad (5.66)
\end{aligned}
$$

5.8 Discussion

The implication of the cut-sky observation is the contamination of the E-mode by the B-mode signal and vice-versa. This is produced by the non-uniqueness of the decomposition of the polarization radiation fields in a finite area of the sky (see, [160]). This is aggravated by the variance of the CMB lensing induced B-mode from the initial E-mode.

We note that the bias matrices $A^E_{ll'}$ and $A^B_{ll'}$ have the same computational cost as they contain exactly the same number of loops. The summations over the polarized beam modes M and M_1 are finite as $M,\ M_1 = \pm 2,\ \pm 4,\ \pm 6$. The summations over the mask multipoles l'' and l''_1 are fixed by the highest multipoles of the mask (cut-off), l''_{max} and l''_{1max}. The computation time of each bias

matrix can be reduced by choosing an apodizing polarization mask whose harmonic transforms fall off rapidly enough with the multipoles l'' and l''_1. This can be achieved, for example by constructing azimuthally apodized masks as indicated in Mitra et al. [140]. In that case, we can restrain the computation to $l''_{max},\ l''_{1max} \sim 100$. In addition, for each mask multipole l'' or l''_1, only the first 10 to 20 m' modes have significant power and consequently the summations over the mask multipoles l'' and l''_1 are finite as well. This implies that the computation time can be reduced by a large factor. We are left with nine summations involved in each Eq. (5.53) and Eq. (5.56). One of the summations which does not appear in Eq. (5.53) and Eq. (5.56), is related to the loop over the multipole l' of the bias matrix. This leads to a computation time that scales as $O(l^9_{max})$, which becomes rapidly prohibitive for large l.

The smoothing of the sky map with an apodized mask weighted by the mask function w^P, increases the variance of the predicted power spectrum and couples the power between adjacent multipoles. The combined effects of the beam non-circularity and cut-sky are localized in the multipole space around the diagonal of the bias matrix. In fact, the bias matrix is not far from diagonal. This allows us to reduce the computation time by choosing a narrow band ($\Delta l \leq 20$ for example) around the diagonal of the bias matrix. This reduces the computation time by a power of l. Furthermore, we can exploit the symmetry relations of the Wigner-d functions in order to reduce the computation cost by an order of magnitude. If we account for all above modifications, the bias matrix calculation can be feasible in a reasonable time by means of a parallel computation.

In the limiting case of a CMB experiment using a full sky survey and non-circular beams, the mixing of power between E and B-modes (estimator "noise") becomes less significant on small angular scales (higher multipoles). Each bias matrix in Eq. (5.64) and Eq. (5.65) contains six independent summations: one of them is over the multipole l' of the bias matrix $A^E_{ll'}$ or $A^B_{ll'}$. The corresponding computational cost scales as $O(l^6_{max})$. We again introduce, as previously suggested, the symmetry properties of the Clebsch-Gordan coefficients and Wigner-d functions and compute the bias matrices around the diagonal band $\Delta l \leq 20$. This allows the reduction of the computation time by a factor of l, and the final computational cost estimate is $\sim O(l^6_{max})$. This is comparable to the computation time estimate, obtained by Mitra et al. [140], of the TT (temperature) bias matrix using non-circular beams and cut-sky.

As mentioned in the previous chapter, an important reduction of the computation time is obtained by precomputing all Wigner-d functions. However at large $l \sim 1000$, the efficiency of the method is limited by disc/memory storage and programme input/output overhead [140]. The idea of parallel computation discussed in [140] can be equally applied in order to compute the EE bias matrix in a reasonable time. The numerical implementation of the EE bias matrix will be carried out using high performance computing, which belongs to our future prospects.

Chapter 6

Conclusion

The cosmic microwave background radiation is an imprint of the radiation fluid at the time of decoupling. The angular power spectra of the CMB temperature and polarization provide a direct test of cosmological models, and lead to the determination of the cosmological parameters. The CMB contains all information about the dynamical parameters of the Universe, and on the standard cosmology and other cosmologies, model of inflations and their variants, and dark energy. The theoretical predictions based on the standard model can be corroborated from the observed CMB maps by means of fast and accurate estimators. On the observational side, the CMB data quantity and quality have been remarkably improved to the extent that the estimation of the angular power spectrum from the measurements becomes a stiff challenge. Correspondingly, several methods have been developed to handle the huge amount of data sets, and estimate the angular power spectrum with a reasonable time. Broadly speaking, CMB power spectra estimators belong to one of the two categories: the maximum likelihood and pseudo-C_l methods. We have mentioned in Chapter 3 that the ML requires extremely heavy computation, and is prohibitive for small angular scales in high resolution CMB experiments. For this reason, alternative methods such as the pseudo-C_l estimator is desirable. Throughout this thesis the power spectra of the temperature and polarization anisotropies have been estimated using the fast suboptimal pseudo-C_l estimator. In CMB surveys, the actual data collected by the telescope detectors contain both the CMB and non-negligible parasitic signals induced by the systematic effects. These systematic errors must be taken into account prior the power spectrum estimation using the estimator of choice. The new estimator that accounts for the systematics, constructed from the initial pseudo-C_l is now unbiased, and can be exploited to retrieve the true power spectra. In CMB data analysis, this is known as the deconvolution process. All information about the systematics are encoded in a matrix called bias matrix or coupling matrix, meaning that the instrument systematics and other effects provoke a coupling and mixing of power between multipoles.

The evaluation of this bias matrix that relates the observed power spectrum to the true one, has

been the ultimate goal of this thesis. Among the systematics, our main focus has been the study of the effects of the non-circular beams and incomplete sky coverage in the TE and EE correlations which have not been carefully considered till date. Our investigation is based on the comparison between the TE power spectra smoothed by a non-circular (elliptical) beam and symmetrized circular Gaussian beam. The main issue of the bias matrix numerical evaluation in most CMB high resolution experiments is the huge computational time. In this thesis, great efforts have been made to compute the bias matrix as fast as possible in the case of CMB polarimetry experiments using non-circular (asymmetric) beams and full sky coverage (Chapter 3), in the trivial case of a non-rotating beam scanning strategy.

We have demonstrated in Chapter 3 that an adequate numerical implementation of the pseudo-C_l estimator allows the computation of the bias matrix with a computational gain that scales as $O(l^{1.8)}$. The corresponding investigations have been restricted to non-circular beams with a complete sky coverage, and we have assumed a non-rotating beam scan. Two important new results have been obtained in Chapter 3: the analytical derivation and numerical evaluation of the TE bias matrix. The new formula obtained which is valid in the limiting case of a simple scanning strategy of non-rotating beam, has been checked for consistency; and we found that it has reproduced the well-known result of the bias matrix of the TE cross-correlation of a CMB experiment using circular (symmetric) Gaussian beams. Although, the most remarkable achievement in this thesis is the optimization of the computation time of the TE bias matrix which has been realized through the smart algorithm implementation of the bias exposed in Chapter 3. Previous work (see, [140]) done in this direction, has utilized computer-intensive parallel processing in order to reduce the computation time ($\sim$ few weeks). Instead, our method can be readily implemented in a computer working with a single CPU processor and a memory of moderate size (2.55 GHz and 4 GB laptop). The pipeline implementation has been proved to be relatively extremely fast ($\sim$ few seconds for $l_{max} = 500$), and the computational time (in seconds) scales as $O(l_{max})$. This computation cost estimate is new, as existing algorithm based on spherical harmonic like the "total convolution" of Wandelt & Górski [22] and Challinor et al. [145] scales as $\sim l_{max}^3 m_{max}$, where l_{max} and m_{max} are the highest multipole and azimuthal beam multipole. This indicates a speed-up factor of $\sim l_{max}^2$ of our algorithm implementation.

The bias matrix of the correlation between T and E using non-circular beams in the presence of a cut-sky has been explicitly calculated for the first time in Chapter 4. We have successively verified the consistency of our new formula. In the limiting case of a full sky coverage and non-circular beam, we have seen that the TE bias matrix reduces to the expression of the bias already obtained in Chapter 3. In addition, we have checked that the new formula can directly reproduce the well-known formula of the bias matrix in the limiting case of a full sky and circularly symmetric beam. Similar investigation has been done in the case of a CMB experiment using a circular beam and incomplete sky, and starting from the new formula obtained, we have shown that, again it reproduces the well-known result of the TE bias matrix of a circular (axisymmetric) beam and

full sky in CMB polarization experiments. The consistency of the bias matrix results in Chapter 4 provides a sufficient proof of the exactness of our formula. The insertion of the mask in the process of foreground removals drastically complicates the computation of the bias matrix. The sky is now non-uniform, and the mask multipoles are coupled to the sky multipoles through the Clebsch-Gordan coefficients and the Wigner-d functions. As a result, the Clebsch-Gordan coefficients and Wigner rotation matrices symmetry relations introduced in Chapter 3 might not be applicable and the bias matrix numerical implementation becomes a huge computational challenge. Nevertheless, one can construct [140] apodized temperature masks whose harmonic transforms die down rapidly with the multipoles, in order to reduce the computation time. At the time of the writing of this thesis, no known numerical work has been done in this direction in the view of computing the bias matrix of the correlation between the temperature T and E-polarization for a CMB experiment using non-circular beams and partial sky coverage. Although, the new analytical results of the bias matrix constitute a stepping-stone for future work that includes the numerical implementation of the TE bias matrix.

New expressions of the EE bias matrices have been obtained in Chapter 5. The analytical derivation of the bias is rather complicated as the EE auto-correlation involves the B-mode component of the polarization power spectrum. The effect of the beam non-circularity and incomplete/non-uniform sky coverage has been included in the calculations of the bias matrices $A^E_{ll'}$ and $A^B_{ll'}$. Apart from the exploitation of the symmetry properties of the Clebsch-Gordan coefficients and Wigner-d functions, a parallel computation can be carried out in order to reduce the computational cost of the bias matrices $A^E_{ll'}$ and $A^B_{ll'}$ numerical evaluations. The numerical implementation of those bias matrices is relatively complicated because of the presence of the polarization mask whose harmonic transforms do not always fall-off rapidly. In such case, the presence of the loops over the mask multipoles up to the multipole cut-off might be problematic as this considerably increases the computation time of each bias matrix. However, by computing the bias matrix within a diagonal band $|l - l'| \leq 20$, and using the Wigner-d function symmetry relations, a reduction of the computation time by a power of l is possible. The computation of the EE bias matrices using high performance parallel processing allows further reduction in the computation time. This is a line of activity we plan to undertake in the future.

For the BB power spectrum that we have not considered in this work, the mixing is worse since $C^{EE}_{l'} \gg C^{BB}_{l'}$. The estimation of the $\tilde{C}_l^{\,BB}$ power spectrum through the EE and BB bias matrices for the extremely faint B-mode signals, which have not been detected up to date; in the presence of a beam asymmetry and cut-sky with the "pure" pseudo-C_l estimator demands deep investigations and belongs to future prospects.

Throughout this work, a precomputation of the Clebsch-Gordan coefficients and Wigner-d functions has been implemented, whenever possible (disc/memory storage dependent) in order to reduce the computation time of the bias matrix.

The *Planck* polarization data is expected to be released in 2014. The high sensitivity and resolution of the *Planck* experiment will provide a high quality and large polarization data size with unprecedented accuracy. After the *Planck* polarization data release, the simulation work described in this thesis, especially the TE power spectrum estimation in the full sky limit, will become particularly valuable and contribute mostly to the understanding of the beam corrections needed in high resolution CMB experiments. Our work provides a very rapid and convenient tool for the TE power spectrum estimation by means of a modest computational resource.

We summarize this thesis by making three insightful remarks. All results have been obtained in the non-rotating beam limit, though the same formalism can be developed in the future to accommodate more general and real CMB polarization experiments scanning strategies. The second remark concerns the ellipticity (eccentricity) of the beam which is assumed to be constant across the sky in the model of beam of Fosalba et al. [66]. Finally, we have used the standard "pseudo-C_l" estimator for the evaluation of the EE bias matrix. In practical applications, the "pure" pseudo-C_l estimator should be employed for the estimation of the EE and BB power spectra in order to avoid the E and B-mode mixing in the standard pseudo-C_l method. This topic is presently outside the scope of this thesis, but in the future the exploitation of this "pure" estimator will be an integral part of our research activities.

Appendices

Appendix A

Consistency checks

We will show in this appendix that for the particular case of a circular beam, the general expression of the bias matrix Eq. (3.50) reduces to the usual form of the window function of a symmetric and co-polar beams in polarization experiments. Only the modes $m'' = 0$ and $M' = \pm 2$ contribute when the beam is circulary symmetric. Replacing this into Eq. (3.50) we get

$$\begin{aligned} A^{TE}_{ll'} &= \pi b^T_{l'0} b^E_{l'2} \sum_{m=-l}^{l} \sum_{L=|l-l'|}^{l+l'} C^{L0}_{l-ml'm} C^{L0}_{l0l'0} \sum_{M=-L}^{L} d^L_{0M}(\frac{\pi}{2}) d^L_{M0}(\frac{\pi}{2}) f_{0M} \sum_{L'=|l-l'|}^{l+l'} C^{L'0}_{l-ml'm} \\ &\times \left[C^{L'0}_{l2l'-2} \sum_{N=-L'}^{L'} d^{L'}_{0N}(\frac{\pi}{2}) d^{L'}_{N0}(\frac{\pi}{2}) f_{0N} + C^{L'-4}_{l-2l'-2} \sum_{N=-L'}^{L'} d^{L'}_{0N}(\frac{\pi}{2}) d^{L'}_{N-4}(\frac{\pi}{2}) f_{-4N} \right. \\ &+ \left. C^{L'4}_{l2l'2} \sum_{N=-L'}^{L'} d^{L'}_{0N}(\frac{\pi}{2}) d^{L'}_{N4}(\frac{\pi}{2}) f_{4N} + C^{L'0}_{l-2l'2} \sum_{N=-L'}^{L'} d^{L'}_{0N}(\frac{\pi}{2}) d^{L'}_{N0}(\frac{\pi}{2}) f_{0N} \right]. \end{aligned} \tag{A.1}$$

The integral $\sum_{M=-L}^{L} d^L_{0M}(\frac{\pi}{2}) d^L_{M0}(\frac{\pi}{2}) f_{0M}$ can be evaluated from the following relation involving spherical harmonics (Eq. (1) of Section 5.9.1 of [146])

$$\int_{4\pi} Y^*_{Lm}(\hat{q}) d\Omega_{\hat{q}} = \sqrt{4\pi} \delta_{L0} \delta_{m0}.$$

Then we introduce the relation between the rotation matrices and spherical harmonics using Eq. (1), Section 4.17 of [146]

$$Y^*_{Lm}(\hat{q}) = \sqrt{\frac{2L+1}{4\pi}} D^L_{m0}(\hat{q}, 0), \tag{A.2}$$

and making use of the following formula (Eq. (E14) of [140]) that relates the rotation matrices to the Wigner-d function

$$D^L_{mm'}(\phi,\theta,\rho) \;=\; i^{m+m'}\, e^{-im\phi} \sum_{M=-L}^{L} \left[(-1)^M\, d^L_{mM}\left(\frac{\pi}{2}\right)\, e^{iM\theta}\, d^L_{Mm'}\left(\frac{\pi}{2}\right)\right] e^{-im'\rho}, \tag{A.3}$$

we derive

$$\sqrt{\frac{2L+1}{4\pi}} i^m \sum_{M=-L}^{L} (-1)^M d^L_{mM}\left(\frac{\pi}{2}\right) d^L_{M0}\left(\frac{\pi}{2}\right) \int e^{-im\phi} d\phi \int e^{iM\theta} \sin\theta d\theta = \sqrt{4\pi}\delta_{L0}\delta_{m0}, \tag{A.4}$$

where $\int e^{-im\phi} d\phi = 2\pi\delta_{m0}$. We identify both sides of Eq. (A.4) and by taking into account the definition

$$f_{0M} = (-1)^M \int_0^\pi d\theta \sin\theta e^{iM\theta} \tag{A.5}$$

derived from Eq. (3.43) in the case of non-rotating beam, it follows that

$$\sum_{M=-L}^{L} d^L_{0M}(\frac{\pi}{2}) d^L_{M0}(\frac{\pi}{2}) f_{0M} = \frac{2}{2L+1}\delta_{L0}. \tag{A.6}$$

This implies that the only non-vanishing terms in Eq. (A.1) are obtained for $L = L' = 0$ which yields

$$A^{TE}_{ll'} = 4\pi b^T_{l'0} b^E_{l'2} \sum_{m=-l}^{l} C^{00}_{l-ml'm} C^{00}_{l0l'0} C^{00}_{l-ml'm} (C^{00}_{l2l'-2} + C^{00}_{l-2l'2}), \tag{A.7}$$

since the other terms of the summations containing the Wigner-d function vanish unless $L' \geq 4$. We can further simplify the above equation by using the properties of the Clebsch-Gordan coefficients. From Eq. (1) of Section 8.5.1 and Eq. (11) of Section 8.4.2 of [146]

$$C^{00}_{a\alpha b\beta} \;=\; (-1)^{a-\alpha} \frac{\delta_{ab}\delta_{\alpha,-\beta}}{\sqrt{2a+1}}, \tag{A.8}$$

$$C^{c\gamma}_{a\alpha b\beta} \;=\; (-1)^{a+b-c} C^{c\gamma}_{a-\alpha b-\beta}, \tag{A.9}$$

we can derive using a simple algebra the following expression of the bias matrix

$$\begin{aligned} A^{TE}_{ll'} &= \frac{8\pi}{2l+1} b^T_{l'0} b^E_{l'2}\ \delta_{ll'} \sum_{m=-l}^{l} (C^{00}_{l-ml'm})^2, \\ &= \frac{8\pi}{2l+1} b^T_{l'0} b^E_{l'2}\ \delta_{ll'}, \end{aligned} \tag{A.10}$$

and finally from the analytical definition of the beam harmonic transforms in Eq. (3.24) where we plug in $\chi = 0$, we recover

$$A^{TE}_{ll'} = e^{-l^2\sigma^2}\ \delta_{ll'}, \tag{A.11}$$

which is the well-known result of the bias matrix for a symmetric beam (see, [147]; [145]).

Appendix B

Evaluation of the integrals I_1, I_2 and I_3

In this appendix we will give the explicit forms of the integrals by using the properties of the spin-s spherical harmonics and Wigner-D functions and their relations to the Clebsch-Gordan coefficients. We use the Eq. (11), Section 5.1.5 and Eq. (1), Section 4.17 of [146]

$$Y^*_{lm}(\hat{q}) = (-1)^m Y_{l-m}(\hat{q}), \tag{B.1}$$

$$Y^*_{lm}(\hat{q}) = \sqrt{\frac{2l+1}{4\pi}} D^l_{m0}(\hat{q}, \rho(\hat{q})), \tag{B.2}$$

and write the spherical harmonic function in the form

$$Y_{lm}(\hat{q}) = (-1)^m \sqrt{\frac{2l+1}{4\pi}} D^l_{-m0}(\hat{q}, \rho(\hat{q})), \tag{B.3}$$

to derive

$$I_1 = (-1)^m \sqrt{\frac{2l+1}{4\pi}} \int d\Omega_{\hat{q}} D^l_{-m0}(\hat{q}, \rho(\hat{q})) D^{l'}_{m'm''}(\hat{q}, \rho(\hat{q})). \tag{B.4}$$

The product of the two Wigner-D functions is expanded in terms of the Clebsch-Gordan coefficients and can be expressed using Eq. (1), Section 4.6 of [146] as follows

$$D^l_{-m0}(\hat{q}, \rho(\hat{q})) D^{l'}_{m'm''}(\hat{q}, \rho(\hat{q})) = \sum_{L=|l-l'|}^{l+l'} C^{L(-m+m')}_{l-ml'm'} D^L_{(-m+m')m''}(\hat{q}, \rho(\hat{q})) C^{Lm''}_{l0l'm''}, \tag{B.5}$$

and then, the integral I_1 can be written as

$$I_1 = (-1)^m \sqrt{\frac{2l+1}{4\pi}} \sum_{L=|l-l'|}^{l+l'} C^{L(-m+m')}_{l-ml'm'} C^{Lm''}_{l0l'm''} \int d\Omega_{\hat{q}} D^L_{(-m+m')m''}(\hat{q}, \rho(\hat{q})). \tag{B.6}$$

We calculate the integrals I_2 and I_3 by making use of the following relation (Eq. (3.11) of [125])

$$ {}_sY_{lm}(\hat{q}) = (-1)^m \sqrt{\frac{2l+1}{4\pi}} D^l_{-ms}(\hat{q}, \rho(\hat{q})) \tag{B.7} $$

for the spin-s spherical harmonics. The integral I_2 can be expressed as

$$ I_2 \;=\; (-1)^m \sqrt{\frac{2l+1}{4\pi}} \int d\Omega_{\hat{q}} D^l_{-m2}(\hat{q}, \rho(\hat{q})) D^{l'}_{m'M}(\hat{q}, \rho(\hat{q})), \tag{B.8} $$

and from Eq. (1), Section 4.6 of [146], the expression reduces to the following form

$$ I_2 \;=\; (-1)^m \sqrt{\frac{2l+1}{4\pi}} \sum_{L=|l-l'|}^{l+l'} C^{L(-m+m')}_{l-ml'm'} C^{L(2+M)}_{l2l'M} \int d\Omega_{\hat{q}} D^L_{(-m+m')(2+M)}(\hat{q}, \rho(\hat{q})). \tag{B.9} $$

We follow the same procedure to evaluate the integral I_3 and find

$$ I_3 \;=\; (-1)^m \sqrt{\frac{2l+1}{4\pi}} \int d\Omega_{\hat{q}} D^l_{-m-2}(\hat{q}, \rho(\hat{q})) D^{l'}_{m'M}(\hat{q}, \rho(\hat{q})), \tag{B.10} $$

which after expansion of the product of Wigner-D functions leads to

$$ I_3 \;=\; (-1)^m \sqrt{\frac{2l+1}{4\pi}} \sum_{L=|l-l'|}^{l+l'} C^{L(-m+m')}_{l-ml'm'} C^{L(-2+M)}_{l-2l'M} \int d\Omega_{\hat{q}} D^L_{(-m+m')(-2+M)}(\hat{q}, \rho(\hat{q})). \tag{B.11} $$

Appendix C

Decomposition of the bias matrix

From Eq. (3.50) we may decompose the general form of the bias matrix corresponding to the beam harmonic transform expansion ($m'' = 0, \pm 2, \pm 4$ for the temperature and $M' = \pm 2, \pm 4, \pm 6$ for the E-mode) as follows

$$\begin{aligned} A^{TE}_{ll'}(term\ 1) &= \pi b^T_{l'0} b^E_{l'2} \sum_{m=-l}^{l} \sum_{L=|l-l'|}^{l+l'} C^{L0}_{l-ml'm} C^{L0}_{l0l'0} \sum_{M=-L}^{L} d^L_{0M}(\tfrac{\pi}{2}) d^L_{M0}(\tfrac{\pi}{2}) f_{0M} \sum_{L'=|l-l'|}^{l+l'} C^{L'0}_{l-ml'm} \\ &\times \left[C^{L'0}_{l2l'-2} \sum_{N=-L'}^{L'} d^{L'}_{0N}(\tfrac{\pi}{2}) d^{L'}_{N0}(\tfrac{\pi}{2}) f_{0N} + C^{L'-4}_{l-2l'-2} \sum_{N=-L'}^{L'} d^{L'}_{0N}(\tfrac{\pi}{2}) d^{L'}_{N-4}(\tfrac{\pi}{2}) f_{-4N} \right. \\ &+ \left. C^{L'4}_{l2l'2} \sum_{N=-L'}^{L'} d^{L'}_{0N}(\tfrac{\pi}{2}) d^{L'}_{N4}(\tfrac{\pi}{2}) f_{4N} + C^{L'0}_{l-2l'2} \sum_{N=-L'}^{L'} d^{L'}_{0N}(\tfrac{\pi}{2}) d^{L'}_{N0}(\tfrac{\pi}{2}) f_{0N} \right], \end{aligned} \tag{C.1}$$

$$\begin{aligned} A^{TE}_{ll'}(term\ 2) &= \pi b^T_{l'2} b^E_{l'2} \sum_{m=-l}^{l} \sum_{L=|l-l'|}^{l+l'} C^{L0}_{l-ml'm} \left(C^{L-2}_{l0l'-2} \sum_{M=-L}^{L} d^L_{0M}(\tfrac{\pi}{2}) d^L_{M-2}(\tfrac{\pi}{2}) f_{-2M} \right. \\ &+ \left. C^{L2}_{l0l'2} \sum_{M=-L}^{L} d^L_{0M}(\tfrac{\pi}{2}) d^L_{M2}(\tfrac{\pi}{2}) f_{2M} \right) \sum_{L'=|l-l'|}^{l+l'} C^{L'0}_{l-ml'm} \\ &\times \left[C^{L'0}_{l2l'-2} \sum_{N=-L'}^{L'} d^{L'}_{0N}(\tfrac{\pi}{2}) d^{L'}_{N0}(\tfrac{\pi}{2}) f_{0N} + C^{L'-4}_{l-2l'-2} \sum_{N=-L'}^{L'} d^{L'}_{0N}(\tfrac{\pi}{2}) d^{L'}_{N-4}(\tfrac{\pi}{2}) f_{-4N} \right. \\ &+ \left. C^{L'4}_{l2l'2} \sum_{N=-L'}^{L'} d^{L'}_{0N}(\tfrac{\pi}{2}) d^{L'}_{N4}(\tfrac{\pi}{2}) f_{4N} + C^{L'0}_{l-2l'2} \sum_{N=-L'}^{L'} d^{L'}_{0N}(\tfrac{\pi}{2}) d^{L'}_{N0}(\tfrac{\pi}{2}) f_{0N} \right], \end{aligned} \tag{C.2}$$

$$
\begin{aligned}
A^{TE}_{ll'}(term\ 3) &= \pi b^T_{l'0} b^E_{l'4} \sum_{m=-l}^{l} \sum_{L=|l-l'|}^{l+l'} C^{L0}_{l-ml'm} C^{L0}_{l0l'0} \sum_{M=-L}^{L} d^L_{0M}(\tfrac{\pi}{2}) d^L_{M0}(\tfrac{\pi}{2}) f_{0M} \sum_{L'=|l-l'|}^{l+l'} C^{L'0}_{l-ml'm} \\
&\times \left[C^{L'-2}_{l2l'-4} \sum_{N=-L'}^{L'} d^{L'}_{0N}(\tfrac{\pi}{2}) d^{L'}_{N-2}(\tfrac{\pi}{2}) f_{-2N} + C^{L'-6}_{l-2l'-4} \sum_{N=-L'}^{L'} d^{L'}_{0N}(\tfrac{\pi}{2}) d^{L'}_{N-6}(\tfrac{\pi}{2}) f_{-6N} \right. \\
&+ \left. C^{L'6}_{l2l'4} \sum_{N=-L'}^{L'} d^{L'}_{0N}(\tfrac{\pi}{2}) d^{L'}_{N6}(\tfrac{\pi}{2}) f_{6N} + C^{L'2}_{l-2l'4} \sum_{N=-L'}^{L'} d^{L'}_{0N}(\tfrac{\pi}{2}) d^{L'}_{N2}(\tfrac{\pi}{2}) f_{2N} \right], \qquad \text{(C.3)}
\end{aligned}
$$

$$
\begin{aligned}
A^{TE}_{ll'}(term\ 4) &= \pi b^T_{l'4} b^E_{l'2} \sum_{m=-l}^{l} \sum_{L=|l-l'|}^{l+l'} C^{L0}_{l-ml'm} \left(C^{L-4}_{l0l'-4} \sum_{M=-L}^{L} d^L_{0M}(\tfrac{\pi}{2}) d^L_{M-4}(\tfrac{\pi}{2}) f_{-4M} \right. \\
&+ \left. C^{L4}_{l0l'4} \sum_{M=-L}^{L} d^L_{0M}(\tfrac{\pi}{2}) d^L_{M4}(\tfrac{\pi}{2}) f_{4M} \right) \sum_{L'=|l-l'|}^{l+l'} C^{L'0}_{l-ml'm} \\
&\times \left[C^{L'0}_{l2l'-2} \sum_{N=-L'}^{L'} d^{L'}_{0N}(\tfrac{\pi}{2}) d^{L'}_{N0}(\tfrac{\pi}{2}) f_{0N} + C^{L'-4}_{l-2l'-2} \sum_{N=-L'}^{L'} d^{L'}_{0N}(\tfrac{\pi}{2}) d^{L'}_{N-4}(\tfrac{\pi}{2}) f_{-4N} \right. \\
&+ \left. C^{L'4}_{l2l'2} \sum_{N=-L'}^{L'} d^{L'}_{0N}(\tfrac{\pi}{2}) d^{L'}_{N4}(\tfrac{\pi}{2}) f_{4N} + C^{L'0}_{l-2l'2} \sum_{N=-L'}^{L'} d^{L'}_{0N}(\tfrac{\pi}{2}) d^{L'}_{N0}(\tfrac{\pi}{2}) f_{0N} \right], \qquad \text{(C.4)}
\end{aligned}
$$

$$
\begin{aligned}
A^{TE}_{ll'}(term\ 5) &= \pi b^T_{l'0} b^E_{l'6} \sum_{m=-l}^{l} \sum_{L=|l-l'|}^{l+l'} C^{L0}_{l-ml'm} C^{L0}_{l0l'0} \sum_{M=-L}^{L} d^L_{0M}(\tfrac{\pi}{2}) d^L_{M0}(\tfrac{\pi}{2}) f_{0M} \sum_{L'=|l-l'|}^{l+l'} C^{L'0}_{l-ml'm} \\
&\times \left[C^{L'-4}_{l2l'-6} \sum_{N=-L'}^{L'} d^{L'}_{0N}(\tfrac{\pi}{2}) d^{L'}_{N-4}(\tfrac{\pi}{2}) f_{-4N} + C^{L'-8}_{l-2l'-6} \sum_{N=-L'}^{L'} d^{L'}_{0N}(\tfrac{\pi}{2}) d^{L'}_{N-8}(\tfrac{\pi}{2}) f_{-8N} \right. \\
&+ \left. C^{L'8}_{l2l'6} \sum_{N=-L'}^{L'} d^{L'}_{0N}(\tfrac{\pi}{2}) d^{L'}_{N8}(\tfrac{\pi}{2}) f_{8N} + C^{L'4}_{l-2l'6} \sum_{N=-L'}^{L'} d^{L'}_{0N}(\tfrac{\pi}{2}) d^{L'}_{N4}(\tfrac{\pi}{2}) f_{4N} \right]. \qquad \text{(C.5)}
\end{aligned}
$$

The idea behind the above decomposition is to separately compute the bias contribution of the leading terms and higher order corrections to the product of the beam harmonic transforms $b^T_{l'm''} b^E_{l'M'}$ where $m'' = 0, \pm 2, \pm 4$ and $M' = \pm 2, \pm 4, \pm 6$, which are sketched in Fig. 3.1 of Chapter 3.

Appendix D

Calculation of the integral I

Using Eq. (9) of Section 5.6 of [146] the product of two spherical functions can be expressed as

$$Y_{lm}(\hat{q})Y_{l''m''}(\hat{q}) = \sum_{L=|l-l''|}^{l+l''} \sqrt{\frac{(2l+1)(2l''+1)}{4\pi(2L+1)}}\; C^{L0}_{l0l''0}\; C^{L(m+m'')}_{lml''m''} Y_{L(m+m'')}(\hat{q}). \tag{D.1}$$

Then, we may write the integral I in Eq. (4.13) as

$$I = \sum_{L=|l-l''|}^{l+l''} \sqrt{\frac{(2l+1)(2l''+1)}{4\pi(2L+1)}}\; C^{L0}_{l0l''0}\; C^{L(m+m'')}_{lml''m''} \int d\Omega_{\hat{q}} Y_{L(m+m'')}(\hat{q}) D^{l'}_{m'n}(\hat{q},\rho(\hat{q})). \tag{D.2}$$

We make use of Eq. (11) of Section 5.1.5 and Eq. (1) of Sec. 4.17 of [146] to derive

$$Y_{L(m+m'')}(\hat{q}) = (-1)^{m+m''}\sqrt{\frac{2L+1}{4\pi}} D^{L}_{-(m+m'')0}(\hat{q},\rho(\hat{q})), \tag{D.3}$$

which leads to the following expression of the integral

$$\begin{aligned} \int d\Omega_{\hat{q}} Y_{L(m+m'')}(\hat{q}) D^{l'}_{m'n}(\hat{q},\rho(\hat{q})) &= (-1)^{m+m''}\sqrt{\frac{2L+1}{4\pi}} \\ &\times \int d\Omega_{\hat{q}} D^{L}_{-(m+m'')0}(\hat{q},\rho(\hat{q})) D^{l'}_{m'n}(\hat{q},\rho(\hat{q})). \end{aligned} \tag{D.4}$$

The product of the Wigner-D functions can be expressed in term of Clebsch-Gordan coefficients by using Eq. (1) of Section 4.6 of [146]

$$\begin{aligned}\int d\Omega_{\hat{q}} D^{L}_{-(m+m'')0}(\hat{q},\rho(\hat{q}))D^{l'}_{m'n}(\hat{q},\rho(\hat{q})) &= \sum_{L'=|L-l'|}^{L+l'} C^{L'(m'-m-m'')}_{L-(m+m'')l'm'}\; C^{L'n}_{L0l'n} \\ &\times \int d\Omega_{\hat{q}} D^{L'}_{(m'-m-m'')n}(\hat{q},\rho(\hat{q})),\end{aligned} \tag{D.5}$$

which after simplification yields the following form

$$\begin{aligned}I &= (-1)^{m+m''}\frac{\sqrt{(2l+1)(2l''+1)}}{4\pi}\sum_{L=|l-l''|}^{l+l''} C^{L0}_{l0l''0}\; C^{L(m+m'')}_{lml''m''} \\ &\times \sum_{L'=|L-l'|}^{L+l'} C^{L'(m'-m-m'')}_{L-(m+m'')l'm'}\; C^{L'n}_{L0l'n}\; \chi^{L'}_{(m'-m-m'')n}[\rho(\hat{q})],\end{aligned} \tag{D.6}$$

where the quantity χ is defined by

$$\chi^{L'}_{(m'-m-m'')n}[\rho(\hat{q})] = \int d\Omega_{\hat{q}} D^{L'}_{(m'-m-m'')n}(\hat{q},\rho(\hat{q})). \tag{D.7}$$

We have seen in Section 3.4, Eq. (3.40) that for the particular case of an equal declination scan strategy $\rho(\hat{q}) = \rho(\theta)$, the above integral can be simplified, and we may write

$$\begin{aligned}\chi^{L'}_{(m'-m-m'')n}[\rho(\theta)] &= 2\pi\delta_{(m'-m-m'')0}\int_0^{\pi} d\theta\,\sin\theta\; d^{L'}_{(m'-m-m'')n}(\theta)e^{-in\rho(\theta)}, \\ &= \chi^{L'}_{0n}[\rho(\theta)].\end{aligned} \tag{D.8}$$

In the above formula the function χ, describing the scanning strategy adopted, is defined by

$$\chi^{L'}_{0n}[\rho(\theta)] = 2\pi\sum_{N=-L'}^{L'} d^{L'}_{0N}(\frac{\pi}{2})d^{L'}_{Nn}(\frac{\pi}{2})\Gamma_{nN}[\rho(\theta)], \tag{D.9}$$

where

$$\Gamma_{nN}[\rho(\theta)] = i^n(-1)^N\int_0^{\pi} d\theta\,\sin\theta\; e^{iN\theta}e^{-in\rho(\theta)}. \tag{D.10}$$

The only non-vanishing term of the integral χ is obtained for $m'-m-m''=0$. Furthermore, if the beam is non-rotating $\rho(\theta)=0$, we have seen that it is possible to calculate analytically the function $\Gamma_{nN}[\rho(\theta)]$. Under this assumption, only the real part of the function Γ contributes, and is

expressed by $\Re\left[\Gamma_{nN}[\rho(\hat{q})=0]\right] \;=\; f_{nN}$ where the function f is defined by

$$f_{nN} \;=\; \begin{cases} (-1)^{(n\pm1)/2}\,\pi/2 & \text{if } n\text{=odd and } N=\pm1 \\ (-1)^{n/2}\,2/(1-N^2) & \text{if both } n,N=0 \text{ or even} \\ 0 & \text{otherwise.} \end{cases} \tag{D.11}$$

Conclusively, Eq. (D.6) plugged in Eq. (4.14), allows us to derive the sky multipoles of the temperature expansion in spherical harmonics, solely in term of Clebsh-Gordan coefficients. The quantity $\chi^{L'}_{0n}[\rho(\hat{q})]$ only depends on the scanning strategy adopted, and can be solved analytically in the simple case of non-rotating beam (i.e. $\rho(\hat{q})=0$). Then, we resume the expression of the integral I as

$$\begin{aligned} I \;&=\; (-1)^{m+m''}\,\frac{\sqrt{(2l+1)(2l''+1)}}{4\pi}\sum_{L=|l-l''|}^{l+l''} C^{L0}_{l0l''0}\; C^{L(m+m'')}_{lml''m''} \\ &\times\; \sum_{L'=|L-l'|}^{L+l'} C^{L'(m'-m-m'')}_{L-(m+m'')l'm'}\; C^{L'n}_{L0l'n}\; \chi^{L'}_{0n}[\rho(\hat{q})=0], \\ &=\; (-1)^{m+m''}\,\frac{\sqrt{(2l+1)(2l''+1)}}{4\pi}\sum_{L=|l-l''|}^{l+l''} C^{L0}_{l0l''0}\; C^{L(m+m'')}_{lml''m''} \\ &\times\; \sum_{L'=|L-l'|}^{L+l'} C^{L'(m'-m-m'')}_{L-(m+m'')l'm'}\; C^{L'n}_{L0l'n}\; 2\pi \sum_{N=-L'}^{L'} d^{L'}_{0N}(\tfrac{\pi}{2}) d^{L'}_{Nn}(\tfrac{\pi}{2}) f_{nN}. \end{aligned} \tag{D.12}$$

Appendix E

Calculation of the integral J_1

First, we derive the integral J_1, then following the same analogy we derive the analytical expression of the integral J_2. We know that the spin-two spherical harmonic function is linked to the Wigner-D function through Eq. (3.11) of [125] which reads

$$\begin{aligned} {}_2Y_{lm}(\hat{q}) &= (-1)^m\sqrt{\frac{2l+1}{4\pi}}D^{l}_{-m2}(\hat{q},\rho(\hat{q})), \\ {}_2Y_{lm}(\hat{q})D^{l'}_{m'M}(\hat{q},\rho(\hat{q})) &= (-1)^m\sqrt{\frac{2l+1}{4\pi}}D^{l}_{-m2}(\hat{q},\rho(\hat{q}))D^{l'}_{m'M}(\hat{q},\rho(\hat{q})). \end{aligned} \tag{E.1}$$

We expand the product of the two Wigner-D functions in terms of Clebsch-Gordan series using Eq. (1), Section 4.6 of [146] as follows

$$D^{l}_{-m2}(\hat{q},\rho(\hat{q}))D^{l'}_{m'M}(\hat{q},\rho(\hat{q})) = \sum_{L=|l-l'|}^{l+l'} C^{L(-m+m')}_{l-ml'm'}D^{L}_{(-m+m')(2+M)}(\hat{q},\rho(\hat{q}))C^{L(2+M)}_{l2l'M}, \tag{E.2}$$

which yields

$${}_2Y_{lm}(\hat{q})D^{l'}_{m'M}(\hat{q},\rho(\hat{q})) = (-1)^m\sqrt{\frac{2l+1}{4\pi}}\sum_{L=|l-l'|}^{l+l'} C^{L(-m+m')}_{l-ml'm'}D^{L}_{(-m+m')(2+M)}(\hat{q},\rho(\hat{q}))C^{L(2+M)}_{l2l'M}. \tag{E.3}$$

Then, we use Eq. (1), Section 4.17 of [146]

$$Y^{*}_{l''_1m''_1}(\hat{q}) = \sqrt{\frac{2l''_1+1}{4\pi}}D^{l''_1}_{m''_10}(\hat{q},\rho(\hat{q})) \tag{E.4}$$

to get the expression of the integral J_1 in the following form

$$\begin{aligned} J_1 &= \sqrt{\frac{2l_1''+1}{4\pi}}(-1)^m\sqrt{\frac{2l+1}{4\pi}}\sum_{L=|l-l'|}^{l+l'} C^{L(-m+m')}_{l-ml'm'}C^{L(2+M)}_{l2l'M} \\ &\times \int d\Omega_{\hat{q}} D^{l_1''}_{m_1''0}(\hat{q},\rho(\hat{q}))D^{L}_{(-m+m')(2+M)}(\hat{q},\rho(\hat{q})). \end{aligned} \tag{E.5}$$

The integral involved in the last term of J_1 can be again calculated by expanding the product of the Wigner-D functions using Eq. (1), Section 4.6 of [146] which reads

$$\begin{aligned} \int d\Omega_{\hat{q}} D^{l_1''}_{m_1''0}(\hat{q},\rho(\hat{q}))D^{L}_{(-m+m')(2+M)}(\hat{q},\rho(\hat{q})) &= \sum_{L'=|l_1''-L|}^{l_1''+L} C^{L'(m_1''-m+m')}_{l_1''m_1''L(-m+m')}C^{L'(2+M)}_{l_1''0L(2+M)} \\ &\times \int d\Omega_{\hat{q}} D^{L'}_{(m_1''-m+m')(2+M)}(\hat{q},\rho(\hat{q})), \end{aligned} \tag{E.6}$$

and finally we may write the integral J_1 as

$$\begin{aligned} J_1 &= (-1)^m\frac{\sqrt{(2l_1''+1)(2l+1)}}{4\pi}\sum_{L=|l-l'|}^{l+l'} C^{L(-m+m')}_{l-ml'm'}C^{L(2+M)}_{l2l'M} \\ &\times \sum_{L'=|l_1''-L|}^{l_1''+L} C^{L'(m_1''-m+m')}_{l_1''m_1''L(-m+m')}C^{L'(2+M)}_{l_1''0L(2+M)}\chi^{L'}_{(m_1''-m+m')(2+M)}[\rho(\hat{q})], \end{aligned} \tag{E.7}$$

where

$$\chi^{L'}_{(m_1''-m+m')(2+M)}[\rho(\hat{q})] = \int d\Omega_{\hat{q}} D^{L'}_{(m_1''-m+m')(2+M)}(\hat{q},\rho(\hat{q})). \tag{E.8}$$

For the particular case of an equal declination scan strategy $\rho(\hat{q}) = \rho(\theta)$, the above integral can be simplified, and we may write (see Section 3.4)

$$\begin{aligned} \chi^{L'}_{(m_1''-m+m')(2+M)}[\rho(\theta)] &= 2\pi\delta_{(m_1''-m+m')0}\int_0^\pi d\theta\ \sin\theta\ d^{L'}_{(m_1''-m+m')(2+M)}(\theta)e^{-i(2+M)\rho(\theta)}, \\ &= \chi^{L'}_{0(2+M)}[\rho(\theta)]. \end{aligned} \tag{E.9}$$

The function χ that describes the scanning strategy adopted is defined by

$$\chi^{L'}_{0(2+M)}[\rho(\theta)] = 2\pi\sum_{N=-L'}^{L'} d^{L'}_{0N}(\frac{\pi}{2})d^{L'}_{N(2+M)}(\frac{\pi}{2})\Gamma_{(2+M)N}[\rho(\theta)], \tag{E.10}$$

where

$$\Gamma_{(2+M)N}[\rho(\theta)] = i^M(-1)^{N+1}\int_0^\pi d\theta\ \sin\theta\ e^{iN\theta}e^{-i(2+M)\rho(\theta)}. \tag{E.11}$$

Assuming that the beam is non-rotating $\rho(\theta) = 0$, we can derive a simple expression of the function $\Re\left[\Gamma_{(2+M)N}[\rho(\hat{q}) = 0]\right] = f_{(2+M)N}$ which reads

$$f_{(2+M)N} = \begin{cases} (-1)^{(2+M\pm1)/2}\,\pi/2 & \text{if } M\text{=odd and } N = \pm1 \\ (-1)^{M/2}\,2/(1-N^2) & \text{if both } (2+M), N = 0 \text{ or even} \\ 0 & \text{otherwise.} \end{cases} \tag{E.12}$$

Hence the analytical expression of the integral J_1 reduces to

$$\begin{aligned} J_1 &= (-1)^m\frac{\sqrt{(2l_1''+1)(2l+1)}}{4\pi}\sum_{L=|l-l'|}^{l+l'} C_{l-ml'm'}^{L(-m+m')}C_{l2l'M}^{L(2+M)} \\ &\times \sum_{L'=|l_1''-L|}^{l_1''+L} C_{l_1''(m-m')L(-m+m')}^{L'0}C_{l_1''0L(2+M)}^{L'(2+M)}f_{(2+M)N}. \end{aligned} \tag{E.13}$$

Appendix F

Calculation of the integral J_2

We can proceed in the same way for the calculation of the second integral J_2. We use Eq. (3.11) of [125] and write

$$\begin{aligned} {}_{-2}Y_{lm}(\hat{q}) &= (-1)^m \sqrt{\frac{2l+1}{4\pi}} D^l_{-m-2}(\hat{q},\rho(\hat{q})), \\ {}_{-2}Y_{lm}(\hat{q}) D^{l'}_{m'M}(\hat{q},\rho(\hat{q})) &= (-1)^m \sqrt{\frac{2l+1}{4\pi}} D^l_{-m-2}(\hat{q},\rho(\hat{q})) D^{l'}_{m'M}(\hat{q},\rho(\hat{q})). \end{aligned} \tag{F.1}$$

We transform the product of the Wigner-D rotation matrices into Clebsch-Gordan series using Eq. (1), Section 4.6 of [146] and obtain

$$\begin{aligned} {}_{-2}Y_{lm}(\hat{q}) D^{l'}_{m'M}(\hat{q},\rho(\hat{q})) &= (-1)^m \sqrt{\frac{2l+1}{4\pi}} \\ &\times \sum_{L=|l-l'|}^{l+l'} C^{L(-m+m')}_{l-ml'm'} D^L_{(-m+m')(-2+M)}(\hat{q},\rho(\hat{q})) C^{L(-2+M)}_{l-2l'M}. \end{aligned} \tag{F.2}$$

We replace, using Eq. (1), Section 4.17 of [146], the spherical harmonic function in term of Wigner-D function and then, obtain the expression of the integral J_2 as follows

$$\begin{aligned} J_2 &= (-1)^m \frac{\sqrt{(2l''_1+1)(2l+1)}}{4\pi} \sum_{L=|l-l'|}^{l+l'} C^{L(-m+m')}_{l-ml'm'} C^{L(-2+M)}_{l-2l'M} \\ &\times \int d\Omega_{\hat{q}} D^{l''_1}_{m''_1 0}(\hat{q},\rho(\hat{q})) D^L_{(-m+m')(-2+M)}(\hat{q},\rho(\hat{q})). \end{aligned} \tag{F.3}$$

We can again evaluate the last integral by using Eq. (1), Section 4.6 of [146], and get

$$\int d\Omega_{\hat{q}} D^{l''_1}_{m''_1 0}(\hat{q},\rho(\hat{q})) D^{L}_{(-m+m')(-2+M)}(\hat{q},\rho(\hat{q})) = \sum_{L'=|l''_1-L|}^{l''_1+L} C^{L'(m''_1-m+m')}_{l''_1 m''_1 L(-m+m')} C^{L'(-2+M)}_{l''_1 0 L(-2+M)} \times \int d\Omega_{\hat{q}} D^{L'}_{(m''_1-m+m')(-2+M)}(\hat{q},\rho(\hat{q})), \quad \text{(F.4)}$$

from which we derive

$$J_2 = (-1)^m \frac{\sqrt{(2l''_1+1)(2l+1)}}{4\pi} \sum_{L=|l-l'|}^{l+l'} C^{L(-m+m')}_{l-ml'm'} C^{L(-2+M)}_{l-2l'M} \times \sum_{L'=|l''_1-L|}^{l''_1+L} C^{L'(m''_1-m+m')}_{l''_1 m''_1 L(-m+m')} C^{L'(-2+M)}_{l''_1 0 L(-2+M)} \chi^{L'}_{(m''_1-m+m')(-2+M)}[\rho(\hat{q})]. \quad \text{(F.5)}$$

For an equal declination scan $\rho(\hat{q}) = \rho(\theta)$, the integral

$$\chi^{L'}_{(m''_1-m+m')(-2+M)}[\rho(\hat{q})] = \int d\Omega_{\hat{q}} D^{L'}_{(m''_1-m+m')(-2+M)}(\hat{q},\rho(\hat{q})) \quad \text{(F.6)}$$

vanishes unless $m''_1 - m + m' = 0$; then under the non-rotating beam assumption $\rho(\hat{q}) = 0$, we end up with the following integral

$$J_2 = (-1)^m \frac{\sqrt{(2l''_1+1)(2l+1)}}{4\pi} \sum_{L=|l-l'|}^{l+l'} C^{L(-m+m')}_{l-ml'm'} C^{L(-2+M)}_{l-2l'M} \times \sum_{L'=|l''_1-L|}^{l''_1+L} C^{L'0}_{l''_1(m-m')L(-m+m')} C^{L'(-2+M)}_{l''_1 0 L(-2+M)} f_{(-2+M)N}. \quad \text{(F.7)}$$

Now, we may obtain the expression of the integral J from the relation $J^* = J_1 + J_2$. The condition of non-rotating beam allows us to write $J = (J_1 + J_2)^* = J_1 + J_2$ since only the real part of the

function Γ contributes. This implies

$$
\begin{aligned}
J &= (-1)^m \frac{\sqrt{(2l_1''+1)(2l+1)}}{4\pi} \sum_{L=|l-l'|}^{l+l'} C_{l-ml'm'}^{L(-m+m')} \sum_{L'=|l_1''-L|}^{l_1''+L} C_{l_1''(m-m')L(-m+m')}^{L'0} \\
&\times \left[C_{l2l'M}^{L(2+M)} C_{l_1''0L(2+M)}^{L'(2+M)} \, 2\pi \sum_{N=-L'}^{L'} d_{0N}^{L'}(\frac{\pi}{2}) d_{N(2+M)}^{L'}(\frac{\pi}{2}) f_{(2+M)N} \right. \\
&+ \left. C_{l-2l'M}^{L(-2+M)} C_{l_1''0L(-2+M)}^{L'(-2+M)} \, 2\pi \sum_{N=-L'}^{L'} d_{0N}^{L'}(\frac{\pi}{2}) d_{N(-2+M)}^{L'}(\frac{\pi}{2}) f_{(-2+M)N} \right], \\
&= \frac{(-1)^m}{2} \sqrt{(2l_1''+1)(2l+1)} \sum_{L=|l-l'|}^{l+l'} C_{l-ml'm'}^{L(-m+m')} \sum_{L'=|l_1''-L|}^{l_1''+L} C_{l_1''(m-m')L(-m+m')}^{L'0} \\
&\times \left[C_{l2l'M}^{L(2+M)} C_{l_1''0L(2+M)}^{L'(2+M)} \sum_{N=-L'}^{L'} d_{0N}^{L'}(\frac{\pi}{2}) d_{N(2+M)}^{L'}(\frac{\pi}{2}) f_{(2+M)N} \right. \\
&+ \left. C_{l-2l'M}^{L(-2+M)} C_{l_1''0L(-2+M)}^{L'(-2+M)} \sum_{N=-L'}^{L'} d_{0N}^{L'}(\frac{\pi}{2}) d_{N(-2+M)}^{L'}(\frac{\pi}{2}) f_{(-2+M)N} \right]. \qquad \text{(F.8)}
\end{aligned}
$$

Appendix G

Useful formulae

We provide a set of the most notably used formulae from Varshalovich et. al. [146], and the relationship between the spin-s spherical harmonics and Wigner-D functions of Goldberg [125].

- The Clebsch-Gordan coefficients:
  Let $\mathbf{j}_1$ and $\mathbf{j}_2$ be two angular momenta with projections m_1 and m_2. The Clebsch-Gordan coefficient denoted by $C^{jm}_{j_1 m_1 j_2 m_2}$ represents the probability amplitude that $\mathbf{j}_1$ and $\mathbf{j}_2$ are coupled into a resultant angular momentum $\mathbf{j}$ with projection m [146]. The Clebsch-Gordan coefficient vanishes unless the following conditions are satisfied:

$$|j_1 - j_2| \leq j \leq j_1 + j_2, \text{ (triangular inequalities)} \tag{G.1}$$

$$m_1 + m_2 = m. \tag{G.2}$$

  In addition, the Clebsch-Gordan coefficients satisfy the following conditions:

  (a) j_1, j_2, j are non-negative integers or half-integers,

  (b) m_1, m_2, m are positive or negative integers or half-integers,

  (c) $|m_1| \leq j_1$, $|m_2| \leq j_2$, $|m| \leq j$,

  (d) $j_1 + m_1$, $j_2 + m_2$, $j + m$, $j_1 + j_2 + j$ are non-negative integers.

- The spherical harmonics, Wigner-D and Wigner-d functions relations:

$$D^l_{mm'}(\hat{q},\rho) = e^{-im\phi} d^l_{mm'}(\theta) e^{-im'\rho}, \qquad \text{Eq. (1), Section 4.3 of [146]}$$

$$Y^*_{lm}(\hat{q}) = \sqrt{\frac{2l+1}{4\pi}}\, D^l_{m0}(\hat{q},\rho), \qquad \text{Eq. (1), Section 4.17 of [146]}$$

$$d^J_{MM'}(\beta) = (-1)^{M-M'}\, d^J_{-M-M'}(\beta) = (-1)^{M-M'} d^J_{M'M}(\beta), \qquad \text{Eq. (1), Section 4.4 of [146]}$$

$$d^J_{MM'}(-\beta) = (-1)^{M-M'}\, d^J_{MM'}(\beta), \qquad \text{Eq. (1), Section 4.4 of [146]}$$

$$d^J_{MM'}(\pi-\beta) = (-1)^{J-M'}\, d^J_{-MM'}(\beta) = (-1)^{J+M}\, d^J_{M-M'}(\beta), \qquad \text{Eq. (1), Section 4.4 of [146]}$$

$$D^{l*}_{mm'}(\hat{q},\rho) = (-1)^{m-m'} D^l_{-m-m'}(\hat{q},\rho), \qquad \text{Eq. (2), Section 4.4 of [146]}$$

$$Y^*_{lm}(\hat{q}) = (-1)^m Y_{l-m}(\hat{q}) \qquad \text{Eq. (1), Section 5.4 of [146]}$$

- The Clebsch-Gordan series: expansion of the product of two Wigner-D functions, Eq.(1), Section 4.6 of [146]:

$$D^{l_1}_{m_1 n_1}(\hat{q},\rho) D^{l_2}_{m_2 n_2}(\hat{q},\rho) = \sum_{l=|l_1-l_2|}^{l_1+l_2} C^{l(m_1+m_2)}_{l_1 m_1 l_2 m_2} D^l_{(m_1+m_2)(n_1+n_2)}(\hat{q},\rho) C^{l(n_1+n_2)}_{l_1 n_1 l_2 n_2}. \qquad \text{(G.3)}$$

- The product of two spherical harmonics, Eq. (9), Section 5.6 of [146]:

$$Y_{l_1 m_1}(\hat{q}) Y_{l_2 m_2}(\hat{q}) = \sum_{l=|l_1-l_2|}^{l_1+l_2} \sqrt{\frac{(2l_1+1)(2l_2+1)}{4\pi(2l+1)}}\, C^{l0}_{l_1 0 l_2 0} C^{l(m_1+m_2)}_{l_1 m_1 l_2 m_2} Y_{l(m_1+m_2)}(\hat{q}). \qquad \text{(G.4)}$$

- The integral over a total solid angle, Eq. (1), Section 5.9.1 of [146]:

$$\int d\Omega_{\hat{q}} Y_{lm}(\hat{q}) = \sqrt{4\pi}\, \delta_{l0}\delta_{m0}. \qquad \text{(G.5)}$$

- The properties of Clebsch-Gordan coefficients:

$$C^{c\gamma}_{a\alpha b\beta} = (-1)^{a+b-c}\, C^{c\gamma}_{b\beta a\alpha}, \qquad \text{Eq. (10), Section 8.4.3 of [146]} \qquad \text{(G.6)}$$

$$C^{c\gamma}_{a\alpha b\beta} = (-1)^{a+b-c}\, C^{c-\gamma}_{a-\alpha b-\beta}, \qquad \text{Eq. (11), Section 8.4.3 of [146]} \qquad \text{(G.7)}$$

$$C^{00}_{a\alpha b\beta} = (-1)^{a-\alpha}\, \frac{\delta_{ab}\, \delta_{\alpha,-\beta}}{\sqrt{2a+1}}, \qquad \text{Eq. (1), Section 8.5 of [146]} \qquad \text{(G.8)}$$

$$C^{c\gamma}_{a\alpha 00} = \delta_{ac}\, \delta_{\alpha\gamma}. \qquad \text{Eq. (2). Section 8.5 of [146]} \qquad \text{(G.9)}$$

- The spin-s spherical harmonics and Wigner-D function (rotation matrices) relations, Eq.

(3.11) of [125]:

$$ {}_sY_{lm}(\hat{q}) = (-1)^m \sqrt{\frac{2l+1}{4\pi}}\, D^l_{-ms}(\hat{q}, \rho(\hat{q})). \tag{G.10} $$

Bibliography

[1] Hu, W. and Dodelson, S., "Cosmic Microwave Background Anisotropies," *ARAA*, vol. 40, pp. 171–216, 2002.

[2] Bennett, C. L. et al., "First-Year Wilkinson Microwave Anisotropy Probe (*WMAP*) Observations: Preliminary Maps and Basic Results," *ApJS*, vol. 148, pp. 1–27, 2003.

[3] M. Kamionkowski, A. Kosowsky, and A. Stebbins, "A Probe of Primordial Gravity Waves and Vorticity," *Physical Review Letters*, vol. 78, pp. 2058–2061, 1997.

[4] Seljak, U. and Zaldarriaga, M., "Signature of Gravity Waves in the Polarization of the Microwave Background," *Physical Review Letters*, vol. 78, pp. 2054–2057, 1997.

[5] M. J. Rees, "Polarization and Spectrum of the Primeval Radiation in an Anisotropic Universe," *ApJL*, vol. 153, p. L1, 1968.

[6] Page, L. et al., "First-Year Wilkinson Microwave Anisotropy Probe (*WMAP*) Observations: Beam Profiles and Window Functions," *ApJS*, vol. 148, 2003.

[7] Crill, B. P. et al., "*BOOMERANG*: A Balloon-borne Millimeter-Wave Telescope and Total Power Receiver for Mapping Anisotropy in the Cosmic Microwave Background," *ApJS*, vol. 148, pp. 527–541, 2003.

[8] Masi, S. et al., "Instrument, method, brightness, and polarization maps from the 2003 flight of *BOOMERANG*," *AAP*, vol. 458, pp. 687–716, 2006.

[9] Huffenberger, K. M. et al., "Measuring *Planck* beams with planets," *AAP*, vol. 510, p. A58, 2010.

[10] Macías-Pérez, J. F. et al., "*Archeops* in-flight performance, data processing, and map making," *AAP*, vol. 467, pp. 1313–1344, 2007.

[11] Chiang, L.-Y. et al., "Asymmetry of the *PLANCK* antenna beam shape and its manifestation in the CMB data," *AAP*, vol. 392, pp. 369–376, 2002.

[12] Górski, K. M. et al., "HEALPix: A Framework for High-Resolution Discretization and Fast Analysis of Data Distributed on the Sphere," *ApJ*, vol. 622, pp. 759–771, 2005.

[13] Ashdown, M. A. J. et al., "Making maps from *Planck* LFI 30 GHz data with asymmetric beams and cooler noise," *AAP*, vol. 493, pp. 753–783, 2009.

[14] Wu, J. H. P. et al., "Asymmetric Beams in Cosmic Microwave Background Anisotropy Experiments," *ApJS*, vol. 132, pp. 1–17, 2001.

[15] Souradeep, T. and Ratra, B., "Window Function for Noncircular Beam Cosmic Microwave Background Anisotropy Experiment," *ApJ*, vol. 560, pp. 28–40, 2001.

[16] Jarosik, N. et al., "Three-Year Wilkinson Microwave Anisotropy Probe (*WMAP*) Observations: Beam Profiles, Data Processing, Radiometer Characterization, and Systematic Error Limits," *ApJS*, vol. 170, pp. 263–287, 2007.

[17] Hill, R. S. et al., "Five-Year Wilkinson Microwave Anisotropy Probe Observations: Beam Maps and Window Functions," *ApJS*, vol. 180, pp. 246–264, 2009.

[18] Maffei, B. et al., "*Planck* pre-launch status: HFI beam expectations from the optical optimisation of the focal plane," *AAP*, vol. 520, p. A12, 2010.

[19] Mitra, S. et al., "Fast Pixel Space Convolution for Cosmic Microwave Background Surveys with Asymmetric Beams and Complex Scan Strategies: FEBeCoP," *ApJS*, vol. 193, p. 5, 2011.

[20] *Planck* Collaboration, "*Planck* 2013 results. IV. Low Frequency Instrument beams and window functions," *ArXiv e-prints*, 2013.

[21] *Planck* Collaboration, "*Planck* 2013 results. VII. HFI time response and beams," *ArXiv e-prints*, 2013.

[22] Wandelt, B. D. and Górski, K. M., "Fast convolution on the sphere," *PRD*, vol. 63, p. 123002, 2001.

[23] Burigana, C. and Gruppuso, A. and Finelli, F., "On the dipole straylight contamination in spinning space missions dedicated to cosmic microwave background anisotropy," *MNRAS*, vol. 371, pp. 1570–1586, 2006.

[24] Gorski, K. M., "On determining the spectrum of primordial inhomogeneity from the *COBE* DMR sky maps: Method," *ApJL*, vol. 430, pp. L85–L88, 1994.

[25] Gorski, K. M. et al., "On determining the spectrum of primordial inhomogeneity from the *COBE* DMR sky maps: Results of two-year data analysis," *ApJL*, vol. 430, pp. L89–L92, 1994.

[26] Tegmark, M., "How to measure CMB power spectra without losing information," *PRD*, vol. 55, pp. 5895–5907, 1997.

[27] J. R. Bond, A. H. Jaffe, and L. Knox, "Estimating the power spectrum of the cosmic microwave background," *PRD*, vol. 57, pp. 2117–2137, 1998.

[28] J. Borrill, "Power spectrum estimators for large CMB datasets," *PRD*, vol. 59, p. 027302, 1999.

[29] Bond, J. R. et al., "Computing challenges of the cosmic microwave background," *Comput. Sci. Eng.*, vol. 1, pp. 21–35, 1999.

[30] Oh, S. P. and Spergel, D. N. and Hinshaw, G., "An Efficient Technique to Determine the Power Spectrum from Cosmic Microwave Background Sky Maps," *ApJ*, vol. 510, pp. 551–563, 1999.

[31] Doré, O. and Knox, L. and Peel, A., "CMB power spectrum estimation via hierarchical decomposition," *PRD*, vol. 64, p. 083001, 2001.

[32] Pen, U.-L., "Fast power spectrum estimation," *MNRAS*, vol. 346, pp. 619–626, 2003.

[33] Challinor, A. D. et al., "Harmonic analysis of cosmic microwave background data - II. From ring-sets to the sky," *MNRAS*, vol. 331, pp. 994–1010, 2002.

[34] van Leeuwen, F. et al., "Harmonic analysis of cosmic microwave background data - I. Ring reductions and point-source catalogue," *MNRAS*, vol. 331, pp. 975–993, 2002.

[35] Wandelt, B. D. and Hansen, F. K., "Fast, exact CMB power spectrum estimation for a certain class of observational strategies," *PRD*, vol. 67, p. 023001, 2003.

[36] Knox, L. and Christensen, N. and Skordis, C., "The Age of the Universe and the Cosmological Constant Determined from Cosmic Microwave Background Anisotropy Measurements," *ApJL*, vol. 563, pp. L95–L98, 2001.

[37] Wandelt, B., "Statistical Challenges of Cosmic Microwave Background Analysis," in *Statistical Problems in Particle Physics, Astrophysics, and Cosmology*, p. 280, 2003.

[38] Jewell, J. and Levin, S. and Anderson, C. H., "Application of Monte Carlo Algorithms to the Bayesian Analysis of the Cosmic Microwave Background," *ApJ*, vol. 609, pp. 1–14, 2004.

[39] Yu, J. T. and Peebles, P. J. E., "Superclusters of Galaxies?," *ApJ*, vol. 158, p. 103, 1969.

[40] Peebles, P. J. E., "Statistical Analysis of Catalogs of Extragalactic Objects. I. Theory," *ApJ*, vol. 185, pp. 413–440, 1973.

[41] Szapudi, I. et al., "Fast Cosmic Microwave Background Analyses via Correlation Functions," *ApJL*, vol. 548, pp. L115–L118, 2001.

[42] Chon, G. et al., "Fast estimation of polarization power spectra using correlation functions," *MNRAS*, vol. 350, pp. 914–926, 2004.

[43] Hivon, E. et al., "MASTER of the Cosmic Microwave Background Anisotropy Power Spectrum: A Fast Method for Statistical Analysis of Large and Complex Cosmic Microwave Background Data Sets," *ApJ*, vol. 567, pp. 2–17, 2002.

[44] Hansen, F. K. and Górski, K. M., "Fast cosmic microwave background power spectrum estimation of temperature and polarization with Gabor transforms," *MNRAS*, vol. 343, pp. 559–584, 2003.

[45] Challinor, A. and Chon, G., "Error analysis of quadratic power spectrum estimates for cosmic microwave background polarization: sampling covariance," *MNRAS*, vol. 360, no. 509-532, 2005.

[46] Brown, M. L. and Castro, P. G. and Taylor, A. N., "Cosmic microwave background temperature and polarization pseudo-C_l estimators and covariances," *MNRAS*, vol. 360, pp. 1262–1280, 2005.

[47] Efstathiou, G., "Myths and truths concerning estimation of power spectra: the case for a hybrid estimator," *MNRAS*, vol. 349, pp. 603–626, 2004.

[48] G. Efstathiou, "Hybrid estimation of cosmic microwave background polarization power spectra," *MNRAS*, vol. 370, pp. 343–362, 2006.

[49] Hinshaw, G. et al., "Three-Year Wilkinson Microwave Anisotropy Probe (*WMAP*) Observations: Temperature Analysis," *ApJS*, vol. 170, pp. 288–334, 2007.

[50] Wandelt, B. D. and Larson, D. L. and Lakshminarayanan, A., "Global, exact cosmic microwave background data analysis using Gibbs sampling," *PRD*, vol. 70, p. 083511, 2004.

[51] Eriksen, H. K. et al., "Power Spectrum Estimation from High-Resolution Maps by Gibbs Sampling," *ApJS*, vol. 155, pp. 227–241, 2004.

[52] Peacock, J. A., *Cosmological Physics*. Cambridge University Press, 1999.

[53] Roos, M., *Introduction to Cosmology*. Chichester: Wiley, 1997.

[54] Dodelson, S., *Modern Cosmology*. Academic Press, 2003.

[55] Gamow, G., "Expanding Universe and the Origin of Elements," *Physical Review*, vol. 70, pp. 572–573, 1946.

[56] Alpher, R. A. and Bethe, H. and Gamow, G., "The Origin of Chemical Elements," *Physical Review*, vol. 73, pp. 803–804, 1948.

[57] Gamow, G., "The origin of elements and the separation of galaxies," *Physical Review*, vol. 74, pp. 505–506, 1948.

[58] Alpher, R. A. and Herman, R. and Gamow, G. A., "Thermonuclear Reactions in the Expanding Universe," *Physical Review*, vol. 74, pp. 1198–1199, 1948.

[59] Alpher, R. A. and Herman, R. C., "Theory of the Origin and Relative Abundance Distribution of the Elements," *Reviews of Modern Physics*, vol. 22, pp. 153–212, 1950.

[60] Penzias, A. A. and Wilson, R. W., "A Measurement of Excess Antenna Temperature at 4080 Mc/s," *ApJ*, vol. 142, pp. 419–421, 1965.

[61] Dicke, R. H. et al., "Cosmic Black-Body Radiation," *ApJ*, vol. 142, pp. 414–419, 1965.

[62] Mather, J. C. et al., "A preliminary measurement of the cosmic microwave background spectrum by the Cosmic Background Explorer (*COBE*) satellite," *ApJL*, vol. 354, pp. L37–L40, 1990.

[63] Fixsen, D. J. and Mather, J. C., "The Spectral Results of the Far-Infrared Absolute Spectrophotometer Instrument on *COBE*," *ApJ*, vol. 581, pp. 817–822, 2002.

[64] Bennett, C. L. et al., "Four-Year *COBE* DMR Cosmic Microwave Background Observations: Maps and Basic Results," *ApJL*, vol. 464, p. L1, 1996.

[65] M. Tristram and K. Ganga, "Data analysis methods for the cosmic microwave background," *Reports on Progress in Physics*, vol. 70, pp. 899–946, 2007.

[66] Fosalba, P. and Doré, O. and Bouchet, F. R., "Elliptical beams in CMB temperature and polarization anisotropy experiments: An analytic approach," *PRD*, vol. 65, p. 063003, 2002.

[67] Sachs, R. K. and Wolfe, A. M., "Perturbations of a Cosmological Model and Angular Variations of the Microwave Background," *ApJ*, vol. 147, p. 73, 1967.

[68] Bennett, C. L. et al., "The Microwave Anisotropy Probe Mission," *ApJ*, vol. 583, pp. 1–23, 2003.

[69] Bennett, C. L. et al., "Nine-year Wilkinson Microwave Anisotropy Probe (*WMAP*) Observations: Final Maps and Results," *ApJS*, vol. 208, p. 20, 2013.

[70] *Planck* Collaboration, "*Planck* 2013 results. XV. CMB power spectra and likelihood," *ArXiv e-prints*, 2013.

[71] Mukhanov, V., *Physical Foundations of Cosmology*. Cambridge University Press, 2005.

[72] Masi, S. et al., "Foregrounds Removal and CMB Fluctuations in a Multiband Anisotropy Experiment: *ARGO* 1993," *ApJL*, vol. 463, p. L47, 1996.

[73] Subrahmanyan, R. et al., "An Australia Telescope survey for CMB anisotropies," *MNRAS*, vol. 315, pp. 808–822, 2000.

[74] Tucker, G. S. et al., "Anisotropy in the Microwave Sky: Results from the First Flight of the Balloon-borne Anisotropy Measurement (*BAM*)," *ApJL*, vol. 475, p. L73, 1997.

[75] Dawson, K. S. et al., "A Preliminary Detection of Arcminute-Scale Cosmic Microwave Background Anisotropy with the *BIMA* Array," *ApJL*, vol. 553, pp. L1–L4, 2001.

[76] Mauskopf, P. D. et al., "Measurement of a Peak in the Cosmic Microwave Background Power Spectrum from the North American Test Flight of *Boomerang*," *ApJL*, vol. 536, pp. L59–L62, 2000.

[77] Netterfield, C. B. et al., "A Measurement by *BOOMERANG* of Multiple Peaks in the Angular Power Spectrum of the Cosmic Microwave Background," *ApJ*, vol. 571, pp. 604–614, 2002.

[78] Baker, J. C., "Detection of cosmic microwave background structure in a second field with the Cosmic Anisotropy Telescope," *MNRAS*, vol. 308, pp. 1173–1178, 1999.

[79] Scott, P. F. et al., "Measurements of Structure in the Cosmic Background Radiation with the Cambridge Cosmic Anisotropy Telescope," *ApJL*, vol. 461, p. L1, 1996.

[80] Padin, S. et al., "First Intrinsic Anisotropy Observations with the Cosmic Background Imager," *ApJL*, vol. 549, pp. L1–L5, 2001.

[81] Hinshaw, G. et al., "Band Power Spectra in the *COBE* DMR Four-Year Anisotropy Maps," *ApJL*, vol. 464, p. L17, 1996.

[82] Halverson, N. W. et al., "Degree Angular Scale Interferometer First Results: A Measurement of the Cosmic Microwave Background Angular Power Spectrum," *ApJ*, vol. 568, pp. 38–45, 2002.

[83] Ganga, K. et al., "The amplitude and spectral index of the large angular scale anisotropy in the cosmic microwave background radiation," *ApJL*, vol. 432, pp. L15–L18, 1994.

[84] Dicker, S. R. et al., "Cosmic microwave background observations with the Jodrell Bank-IAC interferometer at 33 GHz," *MNRAS*, vol. 309, pp. 750–760, 1999.

[85] Femenia, B. et al., "The Instituto Astrofisica de Canarias-Bartol Cosmic Microwave Background Anisotropy Experiment: Results of the 1994 Campaign," *ApJ*, vol. 498, p. 117, 1998.

[86] de Oliveira-Costa, A. et al., "Mapping the Cosmic Microwave Background Anisotropy: Combined Analysis of *QMAP* Flights," *ApJL*, vol. 509, pp. L77–L80, 1998.

[87] Torbet, E. et al., "A Measurement of the Angular Power Spectrum of the Microwave Background Made from the High Chilean Andes," *ApJL*, vol. 521, pp. L79–L82, 1999.

[88] Tanaka, S. T. et al., "Measurements of Anisotropy in the Cosmic Microwave Background Radiation at 0 degrees -8pt.5 Scales near the Stars HR 5127 and Phi Herculis," *ApJL*, vol. 468, p. L81, 1996.

[89] Lee, A. T. et al., "A High Spatial Resolution Analysis of the *MAXIMA*-1 Cosmic Microwave Background Anisotropy Data," *ApJL*, vol. 561, pp. L1–L5, 2001.

[90] Wilson, G. W. et al., "New Cosmic Microwave Background Power Spectrum Constraints from *MSAM1*," *ApJ*, vol. 532, pp. 57–64, 2000.

[91] Readhead, A. C. S. et al., "A limit of the anisotropy of the microwave background radiation on arc minute scales," *ApJ*, vol. 346, pp. 566–587, 1989.

[92] Platt, S. R. et al., "Anisotropy in the Microwave Sky at 90 GHz: Results from *Python* III," *ApJL*, vol. 475, p. L1, 1997.

[93] Coble, K. et al., "Anisotropy in the Cosmic Microwave Background at Degree Angular Scales: *Python* V Results," *ApJL*, vol. 519, pp. L5–L8, 1999.

[94] Leitch, E. M. et al., "A Measurement of Anisotropy in the Cosmic Microwave Background on 7'-22' Scales," *ApJ*, vol. 532, pp. 37–56, 2000.

[95] Netterfield, C. B. et al., "A Measurement of the Angular Power Spectrum of the Anisotropy in the Cosmic Microwave Background," *ApJ*, vol. 474, p. 47, 1997.

[96] Gundersen, J. O. et al., "Degree-scale anisotropy in the cosmic microwave background: *SP*94 results," *ApJL*, vol. 443, pp. L57–L60, 1995.

[97] Schuster, J. et al., "Cosmic background radiation anisotropy at degree angular scales - Further results from the South Pole," *ApJL*, vol. 412, pp. L47–L50, 1993.

[98] Church, S. E. et al., "An Upper Limit to Arcminute-Scale Anisotropy in the Cosmic Microwave Background Radiation at 142 GHz," *ApJ*, vol. 484, p. 523, 1997.

[99] Gutiérrez, C. M. et al., "The Tenerife Cosmic Microwave Background Maps: Observations and First Analysis," *ApJ*, vol. 529, pp. 47–55, 2000.

[100] Miller, A. D. et al., "A Measurement of the Angular Power Spectrum of the Cosmic Microwave Background from L = 100 to 400," *ApJL*, vol. 524, pp. L1–L4, 1999.

[101] Peterson, J. B. et al., "First Results from *Viper*: Detection of Small-scale Anisotropy at 40 GHZ," *ApJL*, vol. 532, pp. L83–L86, 2000.

[102] Partridge, R. B. et al., "Small-Scale Cosmic Microwave Background Observations at 8.4 GHz," *ApJ*, vol. 483, p. 38, 1997.

[103] Tucker, G. S. et al., "A Search for Small-Scale Anisotropy in the Cosmic Microwave Background," *ApJL*, vol. 419, p. L45, 1993.

[104] Lyth, D. H. and Liddle A. R., *The Primordial Density Perturbation*. Cambridge University Press, 2009.

[105] Coles, P. and Lucchin F., *The Origin and Evolution of Cosmic Structure*. Wiley, Chichester, 2002.

[106] Liddle A. R., *An Introduction to Modern Cosmology*. Wiley, Chichester, 2003.

[107] Scott, D. and Srednicki, M. and White, M., "Sample variance in small-scale cosmic microwave background anisotropy experiments," *ApJL*, vol. 421, pp. L5–L7, 1994.

[108] Knox, L., "Determination of inflationary observables by cosmic microwave background anisotropy experiments," *PRD*, vol. 52, pp. 4307–4318, 1995.

[109] Gunn, J. E. and Peterson, B. A., "On the Density of Neutral Hydrogen in Intergalactic Space," *ApJ*, vol. 142, pp. 1633–1641, 1965.

[110] Loeb, A. and Barkana, R., "The Reionization of the Universe by the First Stars and Quasars," *ARAA*, vol. 39, pp. 19–66, 2001.

[111] Barkana, R. and Loeb, A., "In the beginning: the first sources of light and the reionization of the universe," *Physics Reports*, vol. 349, pp. 125–238, 2001.

[112] Hu, W., "CMB temperature and polarization anisotropy fundamentals," *Annals of Physics*, vol. 303, pp. 203–225, 2003.

[113] Zaldarriaga, M., "Polarization of the microwave background in reionized models," *PRD*, vol. 55, pp. 1822–1829, 1997.

[114] Kaplinghat, M. et al., "Probing the Reionization History of the Universe using the Cosmic Microwave Background Polarization," *ApJ*, vol. 583, pp. 24–32, 2003.

[115] Holder, G. P. et al., "The Reionization History at High Redshifts. II. Estimating the Optical Depth to Thomson Scattering from Cosmic Microwave Background Polarization," *ApJ*, vol. 595, pp. 13–18, 2003.

[116] Kogut, A. et al., "First-Year Wilkinson Microwave Anisotropy Probe (*WMAP*) Observations: Temperature-Polarization Correlation," *ApJS*, vol. 148, pp. 161–173, 2003.

[117] Hu, W. and Holder, G. P., "Model-independent reionization observables in the CMB," *PRD*, vol. 68, p. 023001, 2003.

[118] Barkana, R. and Loeb, A., "Gamma-Ray Bursts versus Quasars: Lyα Signatures of Reionization versus Cosmological Infall," *ApJ*, vol. 601, pp. 64–77, 2004.

[119] Knox, L., "CMB signatures of extended reionization," *New Astronomy Reviews*, vol. 47, pp. 883–886, 2003.

[120] Oh, S. P. and Haiman, Z., "Fossil H II regions: self-limiting star formation at high redshift," *MNRAS*, vol. 346, pp. 456–472, 2003.

[121] Onken, C. A. and Miralda-Escudé, J., "History of Hydrogen Reionization in the Cold Dark Matter Model," *ApJ*, vol. 610, pp. 1–8, 2004.

[122] Kovac, J. M. et al., "Detection of polarization in the cosmic microwave background using *DASI*," *Nature*, vol. 420, pp. 772–787, 2002.

[123] Kaplan, J., "CMB Polarization as complementary information to anisotropies," *Comptes Rendus Physique*, vol. 4, pp. 917–924, 2003.

[124] Zaldarriaga, M., "The Polarization of the Cosmic Microwave Background," *Measuring and Modeling the Universe*, p. 309, 2004.

[125] Goldberg, J. N. et al., "Spin-s Spherical Harmonics and $\eth$," *Journal of Mathematical Physics*, vol. 8, pp. 2155–2161, 1967.

[126] Kamionkowski, M. and Kosowsky, A. and Stebbins, A., "Statistics of cosmic microwave background polarization," *PRD*, vol. 55, pp. 7368–7388, 1997.

[127] Zaldarriaga, M. and Seljak, U., "All-sky analysis of polarization in the microwave background," *PRD*, vol. 55, pp. 1830–1840, 1997.

[128] Bunn, E. F. et al., "E/B decomposition of finite pixelized CMB maps," *PRD*, vol. 67, p. 023501, 2003.

[129] Lue, A. and Wang, L. and Kamionkowski, M., "Cosmological Signature of New Parity-Violating Interactions," *Physical Review Letters*, vol. 83, pp. 1506–1509, 1999.

[130] Mitra, S. and Sengupta, A. S. and Souradeep, T., "CMB power spectrum estimation using noncircular beams," *PRD*, vol. 70, p. 103002, 2004.

[131] Tristram, M. et al., "ASYMFAST: A method for convolving maps with asymmetric main beams," *PRD*, vol. 69, p. 123008, 2004.

[132] Page, L. et al., "Three-Year Wilkinson Microwave Anisotropy Probe (*WMAP*) Observations: Polarization Analysis," *ApJS*, vol. 170, pp. 335–376, 2007.

[133] de Zotti, G. et al., "The *Planck* Surveyor mission: astrophysical prospects," in *3K cosmology*, vol. 476, pp. 204–223, 1999.

[134] Rybicki, G. B. and Lightman, A. P., *Radiative processes in astrophysics*. Wiley-Interscience, 1979.

[135] Keating, B. et al., "Large Angular Scale Polarization of the Cosmic Microwave Background Radiation and the Feasibility of Its Detection," *ApJ*, vol. 495, p. 580, 1998.

[136] Schlegel, D. J. et al., "Maps of Dust Infrared Emission for Use in Estimation of Reddening and Cosmic Microwave Background Radiation Foregrounds," *ApJ*, vol. 500, p. 525, 1998.

[137] Watson, R. A. et al., "Detection of Anomalous Microwave Emission in the Perseus Molecular Cloud with the *COSMOSOMAS* Experiment," *ApJL*, vol. 624, pp. L89–L92, 2005.

[138] Lazarian, A. and Draine, B. T., "Resonance Paramagnetic Relaxation and Alignment of Small Grains," *ApJL*, vol. 536, pp. L15–L18, 2000.

[139] Bennett, C. L. et al., "First-Year Wilkinson Microwave Anisotropy Probe (*WMAP*) Observations: Foreground Emission," *ApJS*, vol. 148, pp. 97–117, 2003.

[140] Mitra, S. et al., "Cosmic microwave background power spectrum estimation with non-circular beam and incomplete sky coverage," *MNRAS*, vol. 394, pp. 1419–1439, 2009.

[141] Burigana, C. et al., "Beam distortion effects on anisotropy measurements of the cosmic microwave background," *AAPS*, vol. 130, pp. 551–560, 1998.

[142] Armitage-Caplan, C. and Wandelt, B. D., "PReBeaM for *Planck*: A Polarized Regularized Beam Deconvolution Map-Making Method," *ApJS*, vol. 181, pp. 533–542, 2009.

[143] Burigana, C. and Sáez, D., "Beam deconvolution in noisy CMB maps," *AAP*, vol. 409, pp. 423–437, 2003.

[144] Reinecke, M. et al., "A simulation pipeline for the *Planck* mission," *AAP*, vol. 445, pp. 373–373, 2006.

[145] Challinor, A. et al., "All-sky convolution for polarimetry experiments," *PRD*, vol. 62, p. 123002, 2000.

[146] Varshalovich, D. A. and Moskalev, A. N. and Khersonskii, V. K., *Quantum Theory of Angular Momentum*. Singapore: World Scientific, 1988.

[147] Ng, K.-W. and Liu, G.-C., "Correlation Functions of CMB Anisotropy and Polarization," *International Journal of Modern Physics D*, vol. 8, pp. 61–83, 1999.

[148] Schulten, K. and Gordon, R. G., "Recursive evaluation of 3j and 6j coefficients," *Computer Physics Communications*, vol. 11, pp. 269–278, 1976.

[149] Risbo, T., "Fourier transform summation of Legendre series and D-functions," *Journal of Geodesy*, vol. 70, pp. 383–396, 1996.

[150] Kostelec, P. J. and Rockmore, D. N., "FFTs on the Rotation Group," *Journal of Fourier Analysis and Applications*, vol. 14, pp. 145–179, 2008.

[151] Bersanelli, M. et al., "*Planck* pre-launch status: Design and description of the Low Frequency Instrument," *AAP*, vol. 520, p. A4, 2010.

[152] Lamarre, J.-M. et al., "*Planck* pre-launch status: The HFI instrument, from specification to actual performance," *AAP*, vol. 520, p. A9, 2010.

[153] Tauber, J. A. et al., "*Planck* pre-launch status: The *Planck* mission," *AAP*, vol. 520, p. A1, 2010.

[154] Lewis, A. and Challinor, A., "CAMB: Code for Anisotropies in the Microwave Background." Astrophysics Source Code Library, 2011.

[155] *Planck* Collaboration, "*Planck* 2013 results. XVI. Cosmological parameters," *ArXiv e-prints*, 2013.

[156] *Planck* Collaboration, "*Planck* 2013 results. XXIII. Isotropy and Statistics of the CMB," *ArXiv e-prints*, 2013.

[157] F. R. Bouchet and R. Gispert, "Foregrounds and CMB experiments. I. Semi-analytical estimates of contamination," *New Astronomy*, vol. 4, pp. 443–479, 1999.

[158] Zaldarriaga, M. and Seljak, U., "Gravitational lensing effect on cosmic microwave background polarization," *PRD*, vol. 58, p. 023003, 1998.

[159] Martin, J. and Schwarz, D. J., "Precision of slow-roll predictions for the cosmic microwave background radiation anisotropies," *PRD*, vol. 62, p. 103520, 2000.

[160] Lewis, A. and Challinor, A. and Turok, N., "Analysis of CMB polarization on an incomplete sky," *PRD*, vol. 65, p. 023505, 2002.

[161] Smith, K. M., "Pseudo-C_l estimators which do not mix E and B modes," *PRD*, vol. 74, p. 083002, 2006.

[162] Smith, K. M., "Pure pseudo-C_l estimators for CMB B-modes," *New Astronomy Reviews*, vol. 50, pp. 1025–1029, 2006.

[163] Smith, K. M. and Zaldarriaga, M., "General solution to the E-B mixing problem," *PRD*, vol. 76, p. 043001, 2007.

[164] Tegmark, M. and de Oliveira-Costa, A., "How to measure CMB polarization power spectra without losing information," *PRD*, vol. 64, p. 063001, 2001.

[165] Larson, D. L., "Estimation of Polarized Power Spectra by Gibbs Sampling," *ApJ*, vol. 656, pp. 653–660, 2007.